

**MODELING AND SIMULATION OF
EMBEDDED PASSIVES USING RATIONAL
FUNCTIONS IN MULTI-LAYERED
SUBSTRATES**

A Thesis
Presented to
The Academic Faculty

By

Kwang Lim Choi

In Partial Fulfillment
Of the Requirements for the Degree
Doctor of Philosophy in Electrical and Computer Engineering

Georgia Institute of Technology

August 1999

**MODELING AND SIMULATION OF
EMBEDDED PASSIVES USING RATIONAL
FUNCTIONS IN MULTI-LAYERED
SUBSTRATES**

Approved:

Madhavan Swaminathan, Chairman

Abhijit Chatterjee

David R. Hertling

David C. Keezer

Suresh K. Sitaraman

Date Approved _____

DEDICATION

To God, the creator of the universe and all the physical laws in it,
who is my source of divine wisdom,
for
"fear of the Lord is the beginning of knowledge..." (Proverbs 1:7)

And to Jesus Christ, my Master,
who is my source of freedom.

CONTENTS

DEDICATION	iii
CONTENTS	iv
LIST OF FIGURES	vii
LIST OF TABLES	xii
1 INTRODUCTION	1
1.1 Packaging Technology	2
1.1.1 Low Temperature Cofired Ceramic (LTCC)	4
1.1.2 High Temperature Cofired Ceramic (HTCC)	6
1.1.3 Thin-Film Packaging	7
1.2 Asymptotic Waveform Evaluation	8
1.2.1 Algorithm	8
1.2.2 Stability	10
1.2.3 Enhancements to AWE	12
1.3 Technically Challenging Issues in Realizing Embedded Passives	14
1.4 Proposed Research	15
1.5 Dissertation Outline	16
2 EXTRACTION OF THE FREQUENCY RESPONSE OF EMBEDDED PASSIVES USING LIMITED DATA	17
2.1 Accuracy of Full Wave EM solvers	17
2.2 Acceleration Algorithm	20
2.3 Determining the Required Minimum Number of Data	22
2.4 Interpolation Results and Evaluation of Simulation Time Saving	23

2.5	Reliability of Interpolation	28
2.6	Data Sampling	30
2.6.1	Inductor	31
2.6.2	Capacitor	34
2.6.3	Resistor	35
3	TRANSIENT SIMULATION OF EMBEDDED PASSIVES USING MACROMODELS	37
3.1	Generating A Function with Real Coefficient Polynomials	40
3.2	Generating Functions with Common Poles for Multiple-port Structures	42
3.3	Generating Lossless Functions	45
3.4	Minimum Number of Data Needed	46
3.5	Stability	47
3.6	Implementation in SPICE	49
3.7	Simulation of SPICE Macromodels and Measurement Correlation	51
3.8	Embedded Resistors in High-speed Digital Circuits	59
4	EQUIVALENT CIRCUIT SYNTHESIS	62
4.1	Synthesizable Rational Functions Synthesizable Rational Functions	64
4.2	Synthesis of One-port Network	65
4.3	Examples of Equivalent Circuits for One-port Structures	71
4.1.1.	Inductor	71
4.1.2	Capacitor	76
4.1.3	Resistor	77
4.4	Synthesis of Two-port Networks	79
4.5	Examples of Equivalent Circuits for Two-port Structures	88

4.2.1	Inductor	89
4.2.2	Capacitor	90
4.2.3	Resistor	92
4.6	More Examples of Equivalent Circuits for Thin-film Structures	95
5	STABILITY ENFORCEMENT ALGORITHM	98
5.1	Stability Algorithm	99
5.2	Results of Stability Enforcement Algorithm	101
5.2.1	Inductor	101
5.2.2	Capacitor	103
5.2.3	Resistor	106
5.3	Application of the Stability Enforcement Algorithm	108
6	SIMULATION OF EMBEDDED CIRCUITS USING MACROMODELS AND EQUIVALENT CIRCUITS	111
6.1	Digital Application	112
6.2	Analog and RF Application	119
7.	CONCLUSION AND FUTURE WORK	125
7.1	Conclusion	125
7.2	Future Work	128
7.3	Publications	129
7.4	Awards	130
	APPENDIX	131
	REFERENCES	142
	VITA	148

LIST OF FIGURES

1.1	Passive integration.	2
1.2	Parasitic and lossy effects of a typical embedded spiral inductor.	3
1.3	Different types of embedded inductors.	5
1.4	Parallel plate capacitor.	5
1.5	Interdigitated capacitor.	5
1.6	A typical resistor structure.	6
1.7	Thin-film floating capacitor.	7
1.8	Thin-film resistor.	7
2.1	The inductor structure. All dimensional units are in mils.	19
2.2	Reactance of inductor.	19
2.3	Q of inductor.	19
2.4	$ \lambda_{\min} $ of the inductor structure in Figure 2.1.	23
2.5	The capacitor structure. All dimensional units are in mils.	24
2.6	Imag (Z_{in}) of the inductor.	26
2.7	Q of the inductor.	26
2.8	Error of Imag (Z_{in}) in %.	26
2.9	Error of Q in %.	26
2.10	Mag (S_{21}) of the capacitor.	27
2.11	Phase (S_{21}) of the capacitor.	27
2.12	Error of Mag (S_{21}) in %.	27
2.13	Error of Phase (S_{21}) in %.	27
2.14	Error of Imag(Z_{in}) and Q of varying inductor. All dimensional units are in mils.	29
2.15	Inductor structure used for sampling.	32

2.16	Frequencies where data points were sampled for the inductor structure.	32
2.17	The interpolated response of the inductor as the number of data increases. Dashed dot - P=2 & Q=3, Solid - P=3 & Q=4, Dashed - P=4 & Q=5, Dotted - P=5 & Q=6.	33
2.18	Full set of SONNET data and interpolated response of the inductor using minimum order P = 4 and Q = 5. Dotted - SONNET, dashed - rational function.	33
2.19	Frequency where data points were sampled for the capacitor structure.	34
2.20	The interpolated response of the capacitor as the number of data increases. Dash dot - P=0 & Q=1, solid - P=1 & Q=2, dashed - P=2 & Q=3 (minimum order), dotted - P=3 & Q=4.	35
2.21	Frequencies where data points were sampled for the resistor structure.	36
2.22	The interpolated response of the resistor as the number of data increases.	36
3.1	Macromodeling.	38
3.2	TDR / TDT measurement setup.	52
3.3	Top and side view of the 26 Ω resistor structure. The dimensional units are in mils.	52
3.3	Top and side view of the 858 Ω resistor structure. The dimensional units are in mils.	53
3.5	Pole-zero plot of y11 of 26 Ω resistor.	53
3.6	Admittance parameters of the 26 Ω resistor.	54
3.7	TDR response of 26 Ω resistor.	56
3.8	TDT response of 858 Ω resistor.	57
3.9	Capacitor structure. All dimensional units are in mils.	57
3.10	Response of SONNET and the equivalent circuit of the capacitor.	58
3.11	TDT response of the capacitor.	58
3.12	Transient response of a transmission line terminated with matching impedance of embedded resistor.	59
3.13	Transient response of 858 Ω resistor.	61

3.14	Transient response of 26Ω resistor for a step input with 35 ps rise time.	61
4.1	Equivalent circuit after synthesis of $Z_{in}(s)$ in (4.2).	70
4.2	Example of non-ladder circuit.	70
4.3	Metal dimensions of the inductor. The dimensional units are in mils.	72
4.4	S11 response of SONNET (square) and the equivalent circuit (circle) of the inductor structure L1 in Table 4.1.	73
4.5	A capacitor structure. All dimensional units are in mils.	76
4.6	Equivalent circuit of the 1-port capacitor in Figure 4.5.	77
4.7	Response of SONNET (square) and the equivalent circuit (circle) of the capacitor in Figure 4.5.	77
4.8	A resistor structure. All dimensional units are in mils.	78
4.9	Equivalent circuit of the 1-port resistor in Figure 4.8.	78
4.10	Equivalent circuit that matches z_{11} and zeros z_{21} in (4.10) before the z_{21} scaling.	81
4.11	Equivalent circuit with z_{11} , z_{21} and z_{22} matched for (4.10).	83
4.12	The equivalent circuit of (4.19) before z_{21} scaling and z_{22} matching.	85
4.13	The equivalent circuit of (4.23) before y_{21} scaling and y_{22} matching.	87
4.14	Equivalent circuit of (4.26) before y_{21} scaling and y_{22} matching.	88
4.15	An embedded inductor structure. All dimensional units are in mils.	89
4.16	Equivalent circuit of the 2-port inductor in Figure 4.15.	89
4.17	Equivalent circuit of the 2-port capacitor structure in Figure 4.5.	91
4.18	Response of SONNET (square) and the lossless equivalent circuit (circle) of the 2-port capacitor structure in Figure 4.5.	91
4.19	Lossy equivalent circuit of the capacitor structure in Figure 4.8.	92
4.19	Equivalent circuit of the resistor structure in Figure 4.8. Losses (resistors) were optimized by an optimizer in MDS.	93
4.20	Response of SONNET (square) and the equivalent lossless circuit (circle) of the 2-port resistor in Figure 4.8 before optimization.	94
4.21	Response of SONNET (square) and the lossy equivalent circuit (circle)	

	of the 2-port resistor in Figure 4.8 after optimization.	94
4.23	Lossy equivalent circuit of the resistor structure in Figure 4.8.	95
4.24	SLIM one-port inductor structure.	96
4.25	Equivalent circuit for the SLIM inductor structure shown in Figure 4.24.	96
4.26	SLIM two-port capacitor structure.	97
4.27	The equivalent circuit for the capacitor structure.	97
5.1	The inductor structure. All dimensional units are in mils.	102
5.2	Response of SONNET and the stable function. Dotted - SONNET, dashed - the stable function, x - data points used to update residues.	102
5.3	Capacitor structure. All dimensional units are in mils.	104
5.3	Response of SONNET and the stable function. Dotted - SONNET, dashed - the stable function.	105
5.4	Top and side view of the 26 Ω resistor structure. The dimensional units are in mils.	107
5.5	Input impedance generated by SONNET and the stable function. Dotted - SONNET, dashed - the stable function, x - data points used to update residues.	107
5.6	SLIM resistor structure. All dimensional units are in mils unless stated otherwise.	110
5.8	Equivalent circuit of the resistor structure in Figure 5.7.	110
6.1	Schematic of the digital circuit for test.	113
6.2	The 150 Ω resistor structure. All dimensional units are in mils.	114
6.3	Equivalent circuit of the resistor structure shown in Figure 6.2.	114
6.4	Response of each modeling method for the circuit shown in Figure 6.1. Dashed - macromodel, dotted - equivalent circuit, solid - ideal lumped resistor.	116
6.5	Schematic of the digital circuit.	117

6.6	Response of each modeling method for the circuit shown in Figure 6.5. Dashed - macromodel, dotted - equivalent circuit, solid - ideal lumped resistor.	118
6.7	Bandpass filter using ideal lumped elements.	119
6.8	Filter using empirical models in ADS.	121
6.9	Macromodel for the filter.	123
6.10	Equivalent circuit for the filter.	124
6.11	$ S_{21} $ response of the filter.	124

LIST OF TABLES

1.1	Advantages and disadvantages of embedded passives.	3
2.1	Comparison of simulation time required with and without the method.	28
2.2	Minimum eigenvalue of the inductor structure as the order increases.	33
2.3	Minimum eigenvalue for the capacitor structure.	34
2.4	Minimum eigenvalue for the resistor structure.	36
3.1	Macromodel for 1-port structure using input admittance.	49
3.2	Macromodel for 1-port structure using input impedance.	50
3.3	2-port macromodel using y-parameter functions.	50
3.4	Two-port macromodel using z-parameter functions.	50
4.1	Equivalent circuits as material and physical parameters of the inductor were varied. All dimensional units are in mils.	74
6.1	Electrical and physical parameters for the embedded passives.	120
6.2	Embedded passive structures. All dimensional units are in mils.	120

CHAPTER 1

INTRODUCTION

The trend in portable wireless electronics is to combine digital and RF circuits into a compactly packaged mixed signal module. Examples of such electronics are pagers, cellular phones, transceivers, and global positioning systems that typically function in the RF frequency range. Integral passives represent an emerging technology that has the potential for increased reliability, improved electrical performance, size shrinkage, and reduced cost. Using this technology, surface-mount passive components can be integrated into the substrate on multiple layers. Both organic and inorganic approaches are being investigated around the world for embedded passive technology. This chapter is divided into five sections. The first section deals with currently available packaging technology with examples of embedded structures. The second section discusses Asymptotic Waveform Evaluation, which approximates the response of a large order system using only a few dominant poles and zeros. AWE deserves a serious attention since it provides a standard of merit for comparison with the modeling techniques presented in this dissertation, which also require a low order approximation. The third section discusses technically challenging problems in realizing the embedded passives. The fourth section proposes research needed to answer the issues addressed in the third section. The fifth section describes the remainder of this dissertation.

1.1 Packaging Technology

Today's rapid growth of RF wireless products has turned our attention to reduced-size and cost-effective packaging technology. Design of RF circuits requires packaging that is highly reliable and superior in electrical performance to accommodate its wideband frequency operation. An adequate solution is provided by "passive integration." The aim is to integrate the passive components such as inductors, capacitors, and resistors in a single substrate. Figure 1.1 illustrates the basic concept behind passive integration.

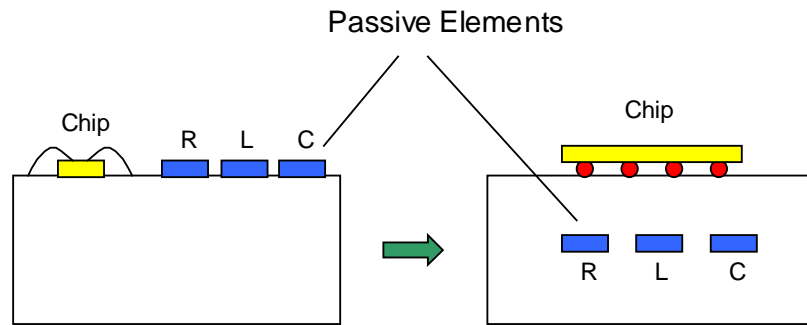


Figure 1.1: Passive integration.

There are several advantages of embedding passive elements over the conventional technique of component mounting on the surface of the board. Embedded passives require no assembly to its board, yielding lower cost. Soldering is not required; thus, solder-joint failure is nonexistent, which translates to better reliability. Other

advantages include improved efficiency and better electrical performance. However, the frequency behavior of the embedded components is dictated by parasitics, losses, and electromagnetic interference. Figure 1.2 illustrates common parasitic and lossy effects with a typical embedded spiral inductor. Dedicated tools or advanced modeling techniques are needed to predict their behavior. The advantages and challenging issues of embedded components are outlined in Table 1.1.

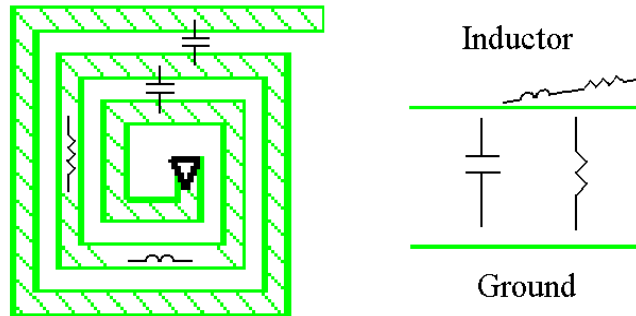


Figure 1.2: Parasitic and lossy effects of a typical embedded spiral inductor.

Table 1.1: Advantages and disadvantages of embedded passives.

<i>Advantages of Embedded Passives</i>		<i>Disadvantages of Embedded Passives</i>	
1.	Reduced cost	1.	Frequency behavior dictated by parasitics, losses, and electromagnetic interference
2.	Better reliability		
3.	Improved electrical performance		
4.	Improved packaging efficiency		
5.	Separate packaging not required		

Ceramic packaging has been considered the best solution to serve all the noted demands due to its electrical, thermal, and dimensional stability. Laminated ceramic packaging technologies, Low Temperature Cofired Ceramic (LTCC) and High Temperature Cofired Ceramic (HTCC) provide the most suitable solution to the full 3-D passive integration and are given the most attention. Another packaging technique under consideration for embedded passives is thin-film packaging technology, which has advantages over thick-film ceramic packaging, as will be discussed later.

1.1.1 Low Temperature Cofired Ceramic (LTCC)

LTCC is a young technology, introduced in the 1980s. Attracted by its unique ability to integrate passive components, researchers in the microelectronics community have been vigorously investigating this technology for electronic packaging [3]. Utilizing this thick-film printing technique, its multilayered ceramic structure allows burying of complex parts with flexible dimensional control. The significance of LTCC lies on low-cost, shrinkage in size, high reliability, and high-density interconnects. It also offers low losses, low permittivity, and duplicable sheet thickness [4]. These characteristics are relevant in the design of RF circuits, making LTCC a desirable technique.

The passive components include inductors, capacitors, and resistors. There are a number of ways to realize passive components in LTCC. A few examples of each type of component will be discussed. The structures presented in this section are in no way the only solution to realize the embedded passives but serve as a guide to provide conceptual

knowledge as they have been adopted by some manufacturers.

Figure 1.3 shows various inductor structures. The inductor types (a) and (b) are realizable on a single layer. The metal can be on the surface or embedded between dielectric layers. Type (c) shows an inductor that has one turn on each layer. To reduce parasitic capacitance between the metals in each layer, each turn may be slightly misaligned, as shown in (d).

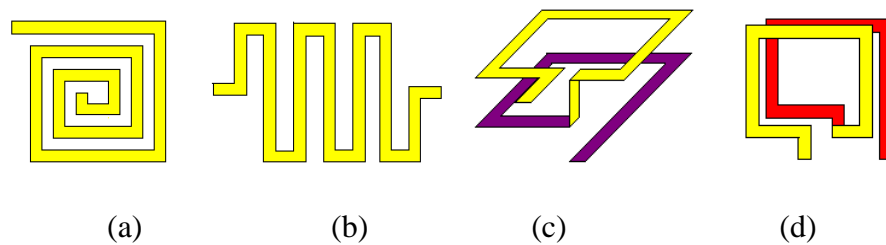


Figure 1.3: Different types of embedded inductors.

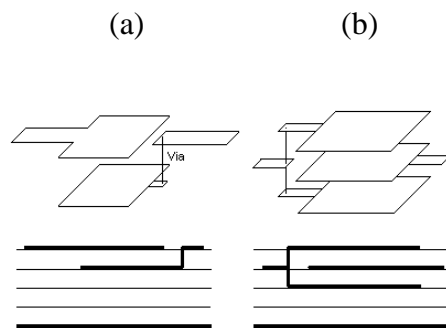


Figure 1.4: Parallel plate capacitor.

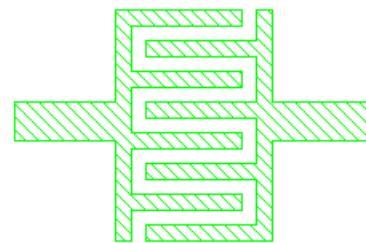


Figure 1.5: Interdigitated capacitor.

Figure 1.4 shows two examples of a parallel plate capacitor in 3-D and its cross-section. The capacitor in (a) is a two-plate capacitor and the one in (b) is a three-plate capacitor. The capacitance varies with the plate dimensions, ϵ_r of the dielectric layers, the distance between the plates, etc. Figure 1.5 shows a top-down view of an interdigitated capacitor. It has relatively small capacitance compared with the size it occupies. The number of fingers and ϵ_r of the material largely determine its capacitance.

Figure 1.6 shows a typical resistor structure. Its DC resistance is mainly determined by resistivity of the lossy metal and its dimensions.

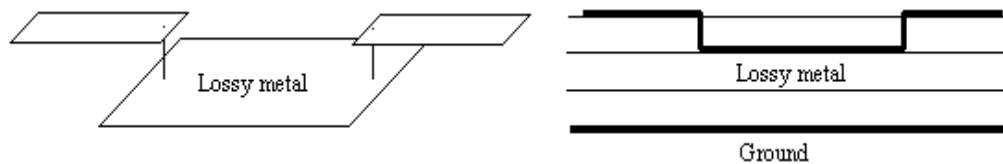


Figure 1.6: A typical resistor structure.

1.1.2 High Temperature Cofired Ceramic (HTCC)

HTCC is similar to LTCC in concept, but there are a few notable differences. Typically 1600°C firing temperature is required in HTCC as opposed to 850°C in LTCC. HTCC generally yields higher loss because of its use of refractory-conducting metals such as tungsten, molybdenum, and manganese. Between 85% and 96% of the ceramic content of HTCC is made up of alumina, while LTCC's alumina content is only 40%-60% [5]. HTCC shares the general advantages of LTCC.

1.1.3 Thin-film Packaging

Thin film often implies coating layer thicknesses of a few micrometers although thicknesses up to 50 μm may also be considered thin film. Typical dimensions of conductors and dielectrics range from 2 μm to 25 μm , compared with the order of 100s of μm in thick-film ceramic packaging such as LTCC [1]. The most commonly used dielectric material is polyimide. The following lists some advantages of thin-film technology compared with thick-film technology.

Thin-film Advantages

1. Size shrinkage with higher density
2. Improvement in interconnect reliability
3. Lighter weight desirable for portable microcomputers and communication devices
4. Ability to use much longer length of film than those in thick-film

As it is a new field, one of the few passive structures found is from the works of the High Density Electronic Center, University of Arkansas and Packaging Research Center, Georgia Tech. Figure 1.7 shows a side view of a thin-film floating capacitor [6]. Figure 1.8 shows a side view of a thin-film resistor [7].

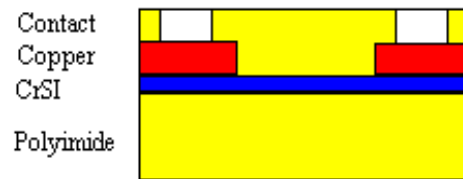
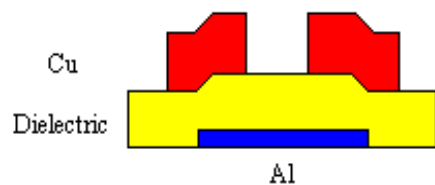


Figure 1.7: Thin-film floating capacitor.

Figure 1.8: Thin-film resistor.

1.2 Asymptotic Waveform Evaluation

Asymptotic Waveform Evaluation (AWE) has a relatively short history but has been discussed in a large number of paper [21]. It is a technique that approximates frequency and time domain responses of a large order system in a rational function with a reduced order. This is possible because the response of a large order system is often dominated by the effect of a few dominant poles. As the order of approximated poles increase, the approximation approaches the actual response. AWE has often been used for analysis of linearized lumped circuits but can also be applied to distributed-element networks as well.

Despite so much favorable attention by many researchers, AWE has its own drawbacks [46]. First, it is very difficult to determine the best reduced order of poles in advance since the number of dominant poles are unknown. Second, stability is not guaranteed. It may produce the poles on the right half plane in the s-domain. A few have addressed the latter problem, which is discussed in this section.

1.2.1 Algorithm

The AWE algorithm can be divided into two parts. The first part is moment generation from a time-domain signal. The second part is moment matching which is recognized as Pade' approximation. The generated moments are matched to a reduced order rational function using Pade' approximation.

Consider a time domain impulse response $f(t)$. Using Laplace transform,

$$F(s) = \int_0^{\infty} f(t) \cdot e^{-s \cdot t} dt \quad (1)$$

After Taylor series expansion about $s=0$, $F(s)$ can be rewritten as

$$F(s) = \int_0^{\infty} f(t) \cdot \left(1 - s \cdot t + \frac{1}{2} \cdot s^2 \cdot t^2 - \dots \right) dt \quad (2)$$

or

$$F(s) = m_0 + m_1 \cdot s + m_2 \cdot s^2 + \dots \quad (3)$$

where

$$m_k = \frac{(-1)^k}{k!} \cdot \int_0^{\infty} t^k \cdot f(t) dt \quad (4)$$

Now consider

$$H(s) = \frac{a_0 + a_1 \cdot s + a_2 \cdot s^2 + \dots + a_p \cdot s^p}{1 + b_1 \cdot s + b_2 \cdot s^2 + \dots + b_Q \cdot s^Q} \quad (5)$$

with the numerator order, P, and the denominator order, Q, which is only half the order of F(s). Usually P=Q-1 but it is not required. Let H(s) and F(s) be equal, then it gives

$$\frac{a_0 + a_1 \cdot s + a_2 \cdot s^2 + \dots + a_P \cdot s^P}{1 + b_1 \cdot s + b_2 \cdot s^2 + \dots + b_Q \cdot s^Q} = m_0 + m_1 \cdot s + m_2 \cdot s^2 + \dots \quad (6)$$

Multiplying both sides with the denominator of H(s) will yield a set of equations which allows one to find all the coefficients, $a_0, a_1, \dots, a_P, b_1, b_2, \dots, b_Q$. More details about solving the equation above can be found in [22]. After partial fraction expansion, H(s) can be rewritten as

$$H(s) = \sum_{i=1}^q \frac{k_i}{s - p_i} \quad (7)$$

The time domain response is obtained from (7).

1.2.2 Stability

One of the most significant concerns raised by AWE is its stability. AWE does not guarantee stability and can produce unstable poles. The paper [21] addresses stability with search of the Pade' Table which is shown in Table 1.1. The H_{pq} is an AWE approximation with numerator order of p and denominator order of q. The idea is to

search the table until satisfactory poles are obtained. Although the search can be made for every approximation, the most efficient way is to search either by diagonal sequence or horizontal sequence. Diagonal search is performed by searching H's which has $p = q-1$ along the diagonal of the table. For horizontal search, q is fixed and p is swiped from 0 to maximum order of P . As p is increased, all the poles of H will converge to those that are nearest to the origin [23]. The lowest poles are most accurate since the Taylor series expansion is performed at $s = 0$. Poles will become inaccurate as their distance is increased from the expansion point, $s = 0$. When a desired number of accurate left half plane poles are obtained, then their corresponding residues can be found.

$$\begin{array}{cccccc}
 H_{00} & H_{01} & H_{02} & \dots & H_{0Q} & \\
 H_{10} & H_{11} & H_{12} & \dots & H_{1Q} & \\
 \dots & \dots & \dots & \dots & \dots & \\
 H_{P0} & H_{P1} & H_{P2} & \dots & H_{PQ} &
 \end{array}$$

Table 1.1: Pade' Table.

Anastasakis, Gopal, Kim and Pillage present another approach to stabilize the approximation [46]. Unstable poles are produced by small effects of inaccurate high frequency poles which results in inaccurate low order moments. High order moments tend to emphasize the effect of low frequency poles and vice versa [21]. The inaccurate low order moments can be avoided by exciting an input that has less power at the high frequency region to nullify the dominance of high frequency pole effect. This is done by

using step, ramp, or even a quadratic input response. In case a ramp input is used, the resulting response is

$$\frac{a_0 + a_1 \cdot s + a_2 \cdot s^2 + \dots + a_p \cdot s^p}{b_0 + b_1 \cdot s + b_2 \cdot s^2 + \dots + b_Q \cdot s^Q} + \frac{A_s}{s} + \frac{A_r}{s^2} \frac{m_0}{s^2} + \frac{m_1}{s} + m_2 + m_3 \cdot s + m_4 \cdot s^2 + \dots + m_{2Q} \cdot s^{2Q} \quad (8)$$

The low order moments are used to solve the particular solution while the higher order moments are used to solve the poles. This yields stable poles with greater accuracy.

Although efforts can be spend to search for accurate and stable poles, the techniques presented in this section do not increase the accuracy of the approximated response. The accuracy of response must be insured by separate means.

1.2.3 Enhancements to AWE

A disadvantage of conventional AWE is its approximation from a single point Taylor expansion. Approximated response will only be accurate close to the expansion point ($s = 0$) but accuracy will degrade as the distance from the expansion point increases. The dominant poles in the higher frequency region of interest may not be detected. To address this issue, Chiprout and Nakhla have introduced a new technique, Complex Frequency Hopping (CFH) [47]. Unlike the original AWE, CFH approximates a function using multiple expansion points with a binary search technique. The accurate poles generated from each expansion point will be collected. The poles are considered accurate when they are within a radius of accuracy around the expansion point. The distance of a

common pole from each expansion point serves as radii of accuracy for each expansion point. The further expansion at new frequency will stop when a common pole is detected. Due to expansion at the maximum frequency of interest, even the poles at the high frequency region are detected accurately which is unavailable in conventional AWE.

The following example will clarify its algorithm. Given a Laplace transform of a time domain signal, the expansion is applied at $s = 0$. Another expansion is applied at highest frequency of interest on imaginary axis. If there is a common pole produced by two expansions, then the poles within the constraints will be collected and their corresponding residues are found. No further expansion is necessary. If there is no common pole, then a new expansion is performed at a frequency between the two previous expansion frequencies. The procedure will continue in the same manner.

Later, Celik, Ocali and Tan claimed a better enhancement to AWE, Multipoint Pade' Approximation (MPA) [48]. Unlike CFH, which extracts poles at different frequency separately, MPA finds poles while all the expansion points are taken into consideration at once. Given the system function $F(s)$, Taylor series expansion is applied at certain frequency $s = s_k$ as

$$F(s) = \sum_{i=0}^{\infty} m_{k,i} \cdot (s - s_k)^i \quad (9)$$

where $m_{k,i}$ is an i -th shifted moment at s_k . Then the following multipoint moment matching is computed,

$$\frac{a_0 + a_1 \cdot s + a_2 \cdot s^2 + \dots + a_p \cdot s^p}{1 + b_1 \cdot s + b_2 \cdot s^2 + \dots + b_q \cdot s^q} = m_{k,0} + m_{k,1} \cdot (s - s_k) + \dots + m_{k,(n_k-1)} \cdot (s - s_k)^{n_k-1} + O\left[(s - s_k)^{n_k}\right]$$

and $k = -n, \dots, 0, \dots, n$ (10)

where n is a number of moments from each expansion at $s = s_k$. Once all the coefficients are found, a standard partial fraction expansion is performed to obtain poles and residues. The details of formulation can be found in [48].

1.3 Technically Challenging Issues in Realizing Embedded Passives

Although much work can be found concerning packaging technology and analysis techniques, the designers of embedded components are still faced with many unanswered challenges. First, there is no fast way to accurately simulate the embedded passive structures. Although empirical models found in advanced RF/microwave simulators may be fast, they are only limited to certain fixed geometry for simple embedded structures. Moreover, they are available for mature technologies and are not relevant for new processes. Only EM solvers are suitable for a wide range of complex structures. However, even with today's rapid advancement in computer processors, currently available EM tools are still very slow. Second, currently, embedded passives may be analyzed only in expensive RF/microwave simulation tools. It is very desirable to make the analysis available in general circuit simulators such as SPICE. Third, a sound

approach to extract a lumped model for embedded structure is yet to be found. James Rautio has presented an approach to synthesize equivalent lumped models using scattering parameter data [16]. However, it has been reported that it is difficult to produce a synthesized model that has a good agreement with high-frequency measurements [14]. Further, undesirable effects of the embedded components in RF frequency are not well understood. A sound technique is needed to study the effects of parasitics, losses, electromagnetic interference, coupling, and frequency dependence, which are of great concern when embedded passive components are operated in RF frequency.

1.4 Proposed Research

Considering the technically challenging issues in the design and modeling of embedded passives, the following research is proposed.

1. Development of an interpolation method that captures the response of embedded passive structures from limited frequency data. This enables the speedup of EM solvers for simulating complex structures.
2. Development of a method for simulating embedded passives using macromodels. This enables the use of frequency-dependent models in a transient simulation. This requires the modification of the rational functions by enforcing the stability condition with complex conjugate poles on the left half plane. Macromodels in SPICE reduce the transient simulation time for complex structures.
3. Although macromodels can be embedded in a SPICE simulation, design kits may require equivalent circuits for RF design. A method is presented that extracts equivalent circuits from rational functions. An important constraint that has been enforced is to ensure that the equivalent circuits correlate with the physical structure.
4. Development of an algorithm that reliably generates stable functions at all times. The interpolation technique in (2) produces a stable solution for most embedded structures. However, the technique does not guarantee a stable solution and may generate rational functions with unstable poles, especially when a high order approximation is performed. An algorithm that guarantees stability is desired.

5. Simulation of circuits that consists of multiple embedded passives using the modeling technique developed in (2) and (3) and evaluation of their response.

1.5 Dissertation Outline

The remainder of this dissertation is organized as follows. Chapter 2 presents an interpolation technique to extract frequency response of embedded structures using a limited sampled data. In Chapter 3, a SPICE macromodeling technique is discussed. In Chapter 4, equivalent circuits are synthesized for embedded structures. In Chapter 5, a stability enforcement algorithm is applied to unstable rational functions. In Chapter 6, macromodeling technique and equivalent circuit synthesis are applied to circuits that consist of multiple embedded components. Finally, Chapter 7 concludes this dissertation and recommends future work.

CHAPTER 2

EXTRACTION OF THE FREQUENCY RESPONSE OF EMBEDDED PASSIVES USING LIMITED DATA

The acceleration algorithm presented in this paper combines the accuracy of EM solvers with an interpolation technique based on Cauchy's method [17][18] to approximate the behavior of embedded passives using limited data. The approximated function is represented as a ratio of two polynomials. This technique saves a significant amount of EM simulation time since the solution requires sampling at limited frequency points.

2.1 Accuracy of Full-wave EM Solvers

Three critical parameters are often used to design embedded passive components (resistors, inductors, and capacitors) in RF circuits, namely the variation of resistance/reactance with frequency, the variation of quality factor (Q) with frequency, and the resonance behavior of the component. Numerous methods are available to analyze these structures such as the partial element equivalent circuit (PEEC) approach [9][10][19][20], empirical techniques (Series IV), and full-wave electromagnetic (EM) methods (SONNET, HFSS) [7][8] to name a few. Since the accuracy of the response

over a large bandwidth is critical in designing RF circuits, the appropriate method has to be applied for the analysis. Full-wave EM techniques provide accurate solutions over a large bandwidth since they solve Maxwell's equations directly with the appropriate boundary conditions. As an example, the variation of reactance with frequency for a one-port embedded RF spiral inductor realized using Low Temperature Cofired Ceramics (LTCC), shown in Figure 2.1, is plotted in Figure 2.2. Both Series IV and SONNET provided good correlation with measured results, while the PEEC method provided a less accurate solution. Though the reactance behavior was captured by Series IV, it produced a less accurate Q variation in Figure 2.3, which is a measure of the loss in the structure. Hence, only SONNET, which is an integral equation-based solver, produced accurate results. This is because all the retardation and loss effects were captured accurately in SONNET as compared with either Series IV or PEEC.

The problem with most full-wave EM solvers is the long analysis time required, which could be hours for a simple structure. The next section shows the mathematical details of the acceleration algorithm. This method combines the accuracy of full-wave EM solvers with an interpolation technique to reduce the simulation time for embedded passive components.

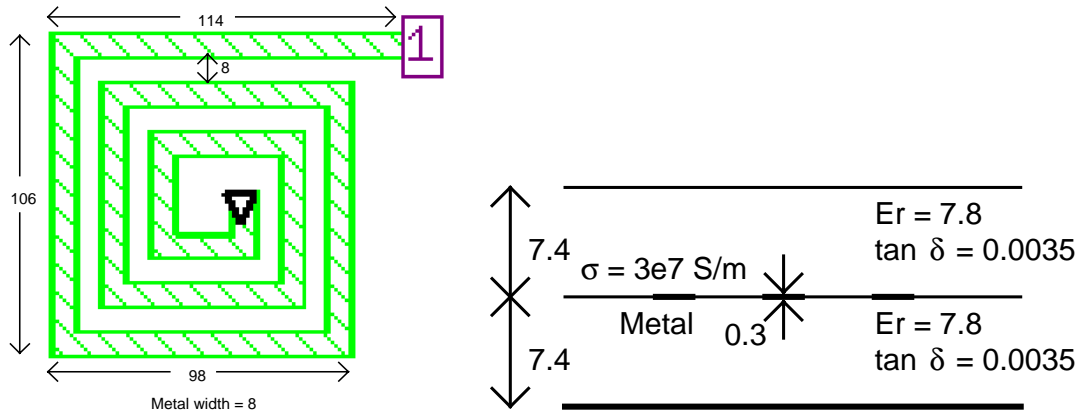


Figure 2.1: The inductor structure. All dimensional units are in mils.

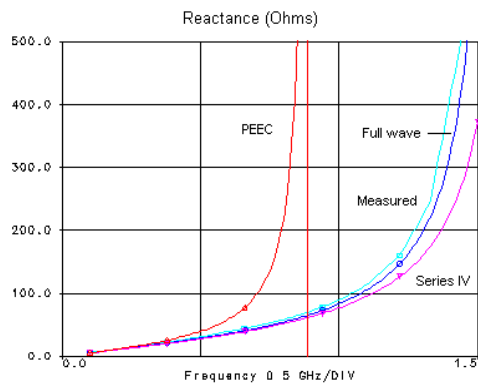


Figure 2.2: Reactance of inductor.

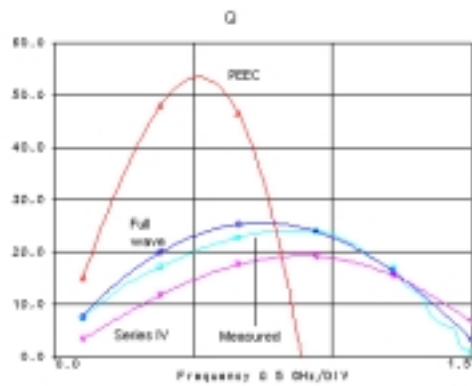


Figure 2.3: Q of inductor.

2.2 Acceleration Algorithm

Consider a function in the frequency domain, which can be represented as

$$H(s) = \frac{\sum_{k=0}^P a_k \cdot s^k}{\sum_{l=0}^Q b_l \cdot s^l}, \quad (2.1)$$

where $s = j \cdot \omega$, ω is the angular frequency, and a_k and b_l are complex coefficients.

Function $H(s)$ could be impedance, admittance, or scattering parameters. Equation (2.1)

can be rewritten as

$$\sum_{k=0}^P a_k \cdot s^k - H(s) \cdot \sum_{l=0}^Q b_l \cdot s^l = 0, \quad (2.2)$$

which can be represented in a matrix form [17],

$$[A] [x] = 0, \quad (2.3)$$

where

$$[A] = \begin{bmatrix} (s_1)^0 & (s_1)^1 & \cdots & (s_1)^P & -H(s_1) \cdot (s_1)^0 & -H(s_1) \cdot (s_1)^1 & \cdots & -H(s_1)^Q \\ (s_2)^0 & (s_2)^1 & \cdots & (s_2)^P & -H(s_2) \cdot (s_2)^0 & -H(s_2) \cdot (s_2)^1 & \cdots & -H(s_2)^Q \\ \vdots & \vdots & \vdots & \vdots & \vdots & \vdots & \vdots & \vdots \\ (s_m)^0 & (s_m)^1 & \cdots & (s_m)^P & -H(s_m) \cdot (s_m)^0 & -H(s_m) \cdot (s_m)^1 & \cdots & -H(s_m)^Q \end{bmatrix} \quad (2.4)$$

and $[x]$ is a solution vector that contains all the coefficients of $H(s)$ as follows:

$$[x] = [a_0 \ a_1 \ \dots \ a_P \ b_0 \ b_1 \ \dots \ b_Q]^T. \quad (2.5)$$

The variable 'm' is the number of available data points with $m \geq P + Q + 2$, where P and Q are the orders of the numerator and denominator, respectively, in (2.1). In general, the order of the polynomials in (2.1) is chosen such that $Q = P + 1$ although it is not a required condition. The data points need not be equally spaced in frequency. The usefulness of setting up the matrix equation as in (2.3) is the nonrequirement for the derivatives of the function $H(s)$ at a given frequency point using the Taylor series expansion [20][21][22][23]. Since equation (2.3) is generated through a set of partial data points and does not involve any derivatives, the equation can be readily applied to compute the response of passive components using commercial EM solvers. Once the orders, P and Q, of the polynomials are determined, the coefficients, a_k and b_i , can be computed by solving λ_{\min} of the equation [24]:

$$[A]^H [A] [x] = \lambda_{\min} [x], \quad (2.6)$$

where $[x]$ is found by solving the eigenvector corresponding to the λ_{\min} (or eigenvalue closest to zero) [18] of $[A]^H[A]$ in equation (2.6). The superscript 'H' denotes the complex conjugate transpose of the matrix $[A]$. Since no condition is enforced on the coefficients, a_k and b_l , and since the matrix $[A]^H[A]$ is complex, the eigenvectors are complex. Hence, the coefficients, a_k and b_l , are complex. However, equation (2.6) allows one to interpolate the response by determining the coefficients, a_k and b_l , once the order of the polynomial (P and Q) is determined.

2.3 Determining the Required Minimum Number of Data

To determine the minimum number of data points required for the interpolation, the λ_{\min} of the matrix $[A]^H[A]$ is observed as the order of the polynomial, P and Q, is increased. The value of λ_{\min} decreases to a point where any further decrease is not significant. The value of P and Q used at that point is the minimum order of the polynomial. To construct $[A]$ in (2.4) and solve (2.6), the required minimum number of data points is $P+Q+2$. The minimum order, P and Q, (or minimum number of data points, $P+Q+2$) is found only once for a class of structure. The same order of the polynomial can be subsequently used for the same class of structures.

As an example, Figure 2.4 shows how $|\lambda_{\min}|$ of the matrix $[A]^H[A]$ of the inductor structure, shown in Figure 2.1, varies with the value of $P+Q+2$. For $P+Q+2 = 6$, $|\lambda_{\min}|$ approaches zero and does not significantly decrease thereafter, showing that the minimum order of the solution is four and the minimum number of data points required is

six. Since $P+Q = 4$, the order $P=2$ and $Q=2$ should be used. However, for the experiments presented in this chapter, $P+Q+2$ is chosen to be seven (unless stated otherwise) to keep P less than Q . In this way, the order $P=2$ and $Q=3$ may be used.

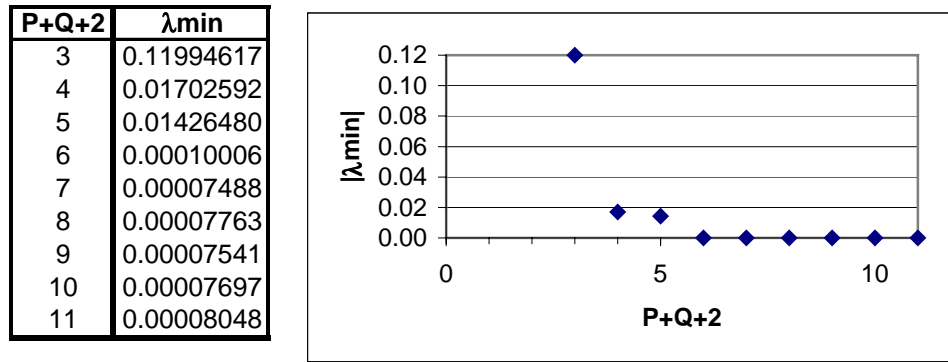


Figure 2.4: $|\lambda_{\min}|$ of the inductor structure in Figure 2.1.

2.4 Interpolation Results and Evaluation of Simulation Time Saving

Two embedded passive components were tested to evaluate the validity of the acceleration algorithm. The technique was applied to an embedded one-port spiral inductor, shown in Figure 2.1, and an embedded two-port parallel plate capacitor, shown in Figure 2.5.

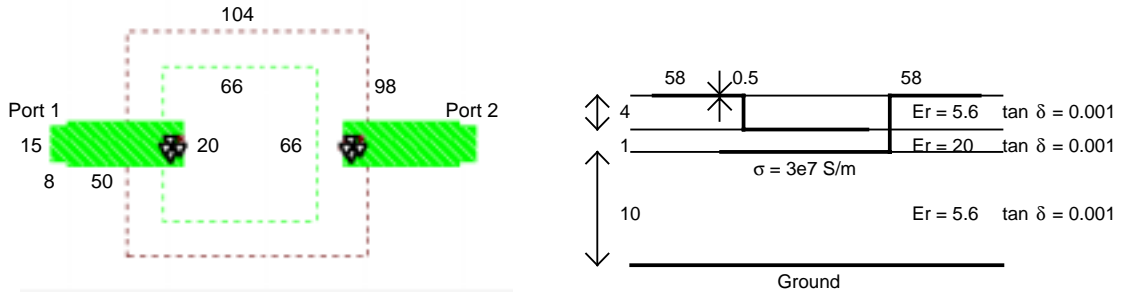


Figure 2.5: The capacitor structure. All dimensional units are in mils.

The spiral inductor was based on the LTCC ground rules supplied by National Semiconductor, while the high-frequency RF capacitor was also realized using LTCC-M technology. For both the inductor and the capacitor, the polynomial order of $P = 2$ and $Q = 3$ was used. SONNET [25] was used to simulate the structures to extract S-parameter data at seven frequency points. These frequency points were arbitrarily chosen over the frequency band of interest. In the case of the inductor, s-parameter data was interpolated to generate the following function:

$$S_{11}(s) = \frac{a_0 + a_1 \cdot s + a_2 \cdot s^2}{b_0 + b_1 \cdot s + b_2 \cdot s^2 + b_3 \cdot s^3} \quad a = \begin{pmatrix} -0.2038 - 0.2263i \\ 0.356 + 0.2012i \\ -0.1332 - 0.0078i \end{pmatrix} \quad b = \begin{bmatrix} 0.2032 + 0.2391i \\ 0.2936 + 0.5493i \\ 0.051 + 0.4663i \\ -0.0627 + 0.1093i \end{bmatrix}, \quad (2.7)$$

which was later converted to input impedance

$$Z_{11}(s) = \frac{c_0 + c_1 \cdot s + c_2 \cdot s^2 + c_3 \cdot s^3}{d_0 + d_1 \cdot s + d_2 \cdot s^2 + d_3 \cdot s^3} \cdot 50 \quad c = \begin{bmatrix} -6 \cdot 10^{-4} + 0.0128i \\ 0.6496 + 0.7505i \\ -0.0822 + 0.4585i \\ -0.0627 + 0.1093i \end{bmatrix} \quad d = \begin{bmatrix} 0.407 + 0.4654i \\ -0.0624 + 0.3481i \\ 0.1842 + 0.4741i \\ -0.0627 + 0.1093i \end{bmatrix} \quad (2.8)$$

The equations (2.7) and (2.8) are normalized functions with a frequency scaling factor of 10^{10} . Figures 2.6 and 2.7 show the imaginary part of Z_{11} and Q of the inductor, respectively. The equation (2.8) has the following poles:

$$\text{poles} = \begin{pmatrix} -2.2029 + 3.3559i \\ -0.3213 - 1.1997i \\ -0.012 + 0.984i \end{pmatrix}, \quad \begin{array}{|l} \text{translates to 1.57 GHz} \\ \text{after frequency scaling} \end{array} \quad (2.9)$$

which contain the resonant frequency. As can be seen from the figures, equation (2.8) captured the resonant frequency very accurately even though no data point was chosen at the resonant frequency. The error of $\text{Imag}(Z_{11})$ and Q between the full set of SONNET-generated data and the interpolated response (equation (2.8)) is shown in Figure 2.8 and 2.9, respectively. The largest error was less than 3%, demonstrating the accuracy of this interpolation technique.

In case of the capacitor, Figures 2.10 and 2.11 compare the magnitudes and phases, respectively, of the full set of SONNET data and the interpolated response using only seven data points. Figures 2.12 and 2.13 show the error of the magnitude and phase, respectively. As shown, the error was less than 0.4% in the worst case, again suggesting that the interpolation method is well suited for modeling embedded passive components.

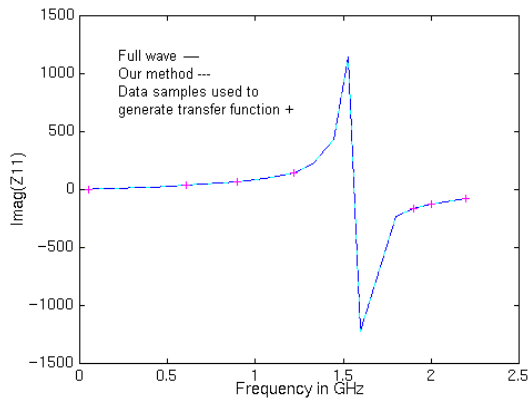


Figure 2.6 Imag (Z_{in}) of the inductor.

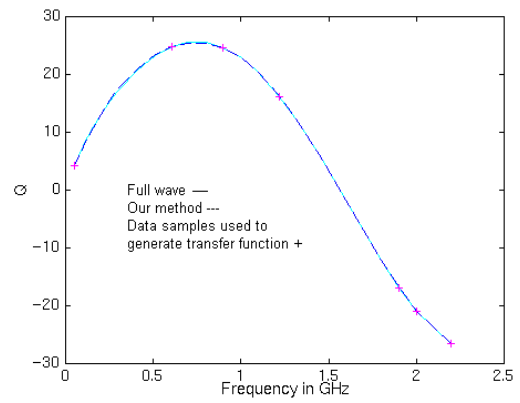


Figure 2.7: Q of the inductor.

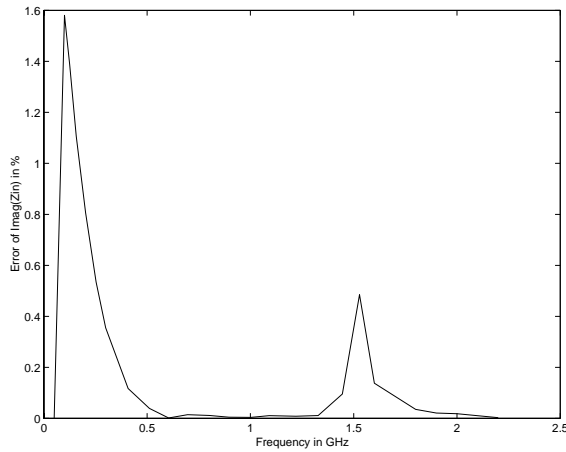


Figure 2.8: Error of Imag (Z_{in}) in %.

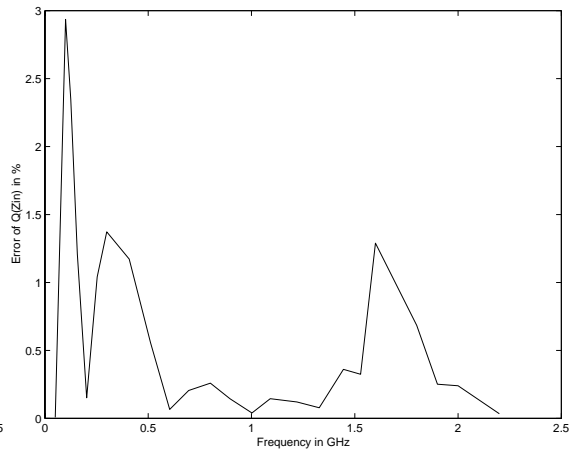


Figure 2.9: Error of Q in %.

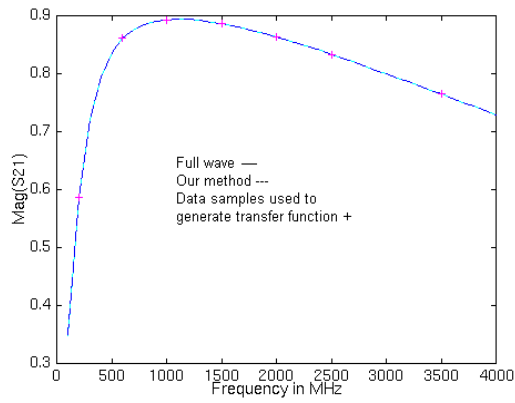


Figure 2.10: Mag (S21) of the capacitor.

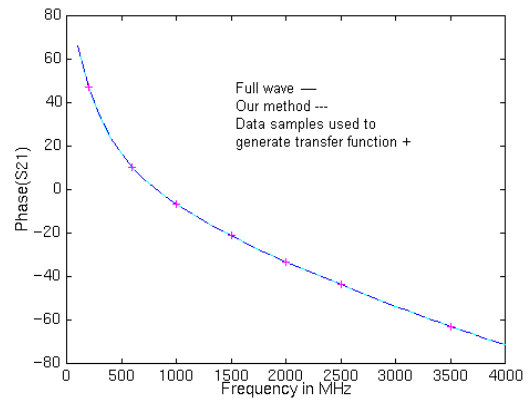


Figure 2.11: Phase (S21) of the capacitor.

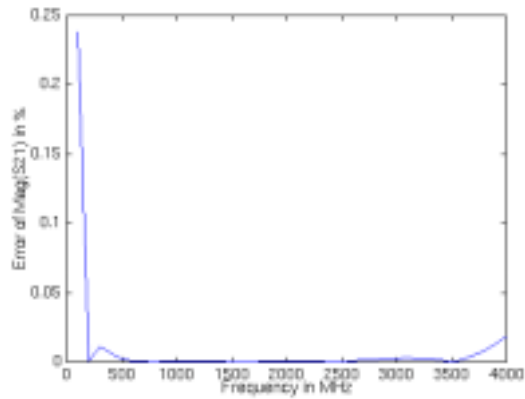


Figure 2.12: Error of Mag (S21) in %.

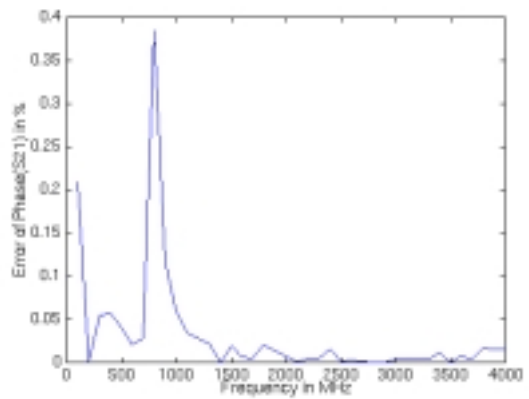


Figure 2.13: Error of Phase (S21) in %.

The technique described in this paper saves a significant amount of time in predicting the accurate response of embedded passive components in RF circuits. Table 2.1 summarizes savings in simulation time for the inductor and the capacitor structure analyzed using a high-end Sun Workstation with 512MB RAM. As shown in Table 1, the interpolation technique is useful for complicated multilayered structures, such as capacitors, and provides a means for significant reductions in computation time.

Table 2.1: Comparison of simulation time required with and without the method.

Type	Frequency Band	SONNET		Present Method	
		Data Points	Simulation Time	Data Points	Simulation Time
Inductor	DC - 2.2 GHz	24	15.2 minutes	7	4.4 minutes
Capacitor	DC - 4 GHz	40	3.7 hours	7	39 minutes

2.5 Reliability of Interpolation

To ensure that the minimum number of data points do not change for similar classes of structures, the response of the spiral inductor was extracted using the interpolation algorithm for varying physical parameters. The metal winding is shown in Figure 2.1 and its physical variations are indicated in Figure 2.14. The interpolation algorithm used six equally spaced data points over 4 GHz bandwidth, and its result was compared with the frequency response obtained using 40 data points equally spaced with 0.1 GHz intervals. The error between the actual response and the interpolated response is shown in Figure 2.14, where the error is less than 6 %.

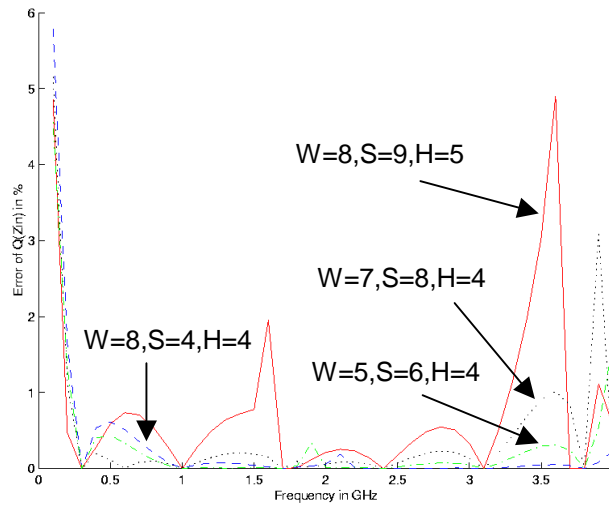
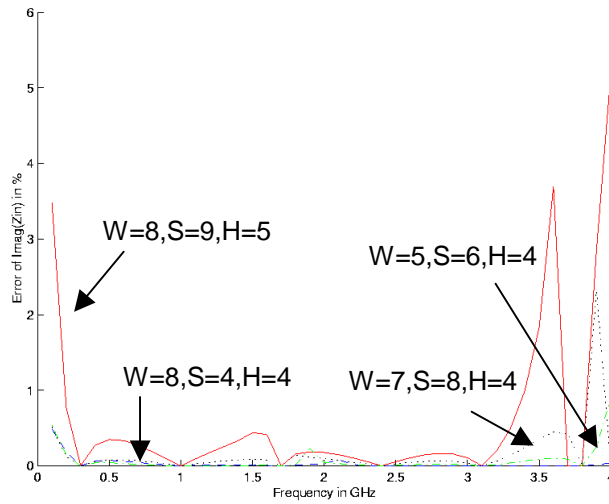
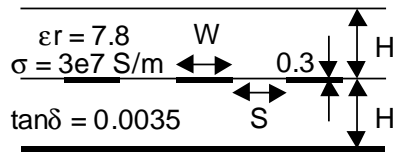


Figure 2.14: Error of $\text{Imag}(Z_{in})$ and Q of varying inductor. All dimensional units are in mils.

2.6 Data Sampling

In Section 2.3, an eigenvalue method was used to determine the required minimum order using a full set of data. Once the minimum order, P and Q , is found by evaluating the eigenvalues, the same order can be used for similar classes of structures as shown in Section 2.5. With a known order, the required minimum number of data may be sampled with equally spaced intervals. However, equal spacing is not a required condition and it is only sought for simplicity.

In this section, a sampling method is presented to illustrate data sampling and ensure the minimum number of samples are used for a new structure. When a full set of data is not available for a new structure with an unknown order, a minimum number of data may still be used to find the minimum order by choosing data points selectively. This method is useful since a significant reduction in simulation time is still achieved with a new structure. The following procedure describes one of the sampling methods.

1. A minimum of three data points are required for interpolation since the smallest order a rational function can have is $P = 0$ and $Q = 1$. Once a desired frequency band is determined, obtain three data points at the lowest frequency, the highest frequency, and the frequency in the middle. Obtain the minimum eigenvalue of $[A]^H[A]$.
2. Obtain a data point between the two data points that are located closest in (1). Repeat to obtain another data point symmetrically from the center (or the frequency point in the middle in (1)). Two more data points are obtained in this

- step. Use all the data points obtained in (1) and (2) for interpolation and find the minimum eigenvalue of $[A]^H[A]$.
3. If the interpolated response in (1) agrees closely to the interpolated response in (2), the responses have converged. The order associated with the number of data points in the previous step is used. If they do not agree, the step (2) is repeated until the convergence occurs. The convergence is easily determined by observing the minimum eigenvalues. If λ_{\min} in (1) and λ_{\min} in (2) are close, λ_{\min} has converged. If λ_{\min} in (1) and λ_{\min} in (2) are significantly different, repeat step (2) until λ_{\min} converges to the λ_{\min} of the previous step.

The method is illustrated in the following examples. This approach was applied to an inductor, a capacitor, and a resistor structure and the following subsections discuss the results.

2.6.1 Inductor

The sampling method was applied to an inductor structure shown in Figure 2.15. The data points were obtained using SONNET and the response of input impedance was interpolated up to 10 GHz. The data points were sampled as shown in Figure 2.16. As the order was increased by two, additional two data points were simulated at the frequency points shown in Figure 2.16. Table 2.2 shows the minimum eigenvalue corresponding to the order. Figure 2.17 shows the interpolated response for each order. The response converged when the value of $P+Q+2$ was 11 and 13, which shows that the

minimum number of data points required for interpolation up to 10 GHz is eleven. Figure 2.18 shows the interpolated response with 11 data points and the full set of the SONNET-generated data. It shows good agreement.

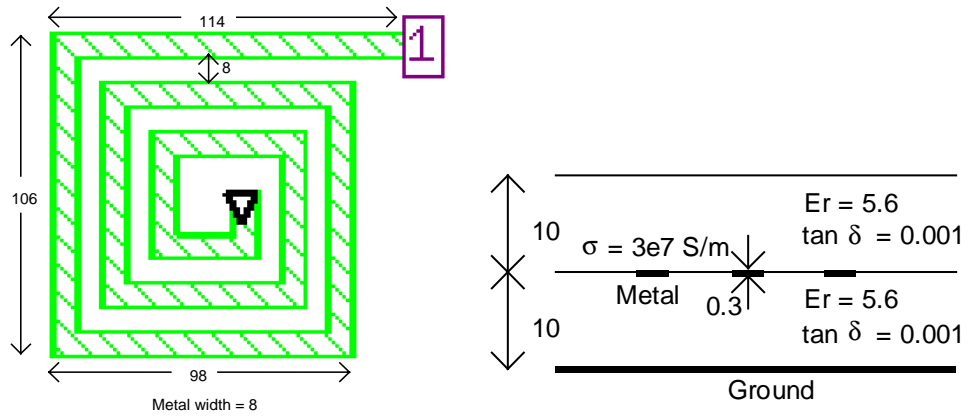


Figure 2.15: Inductor structure used for sampling.

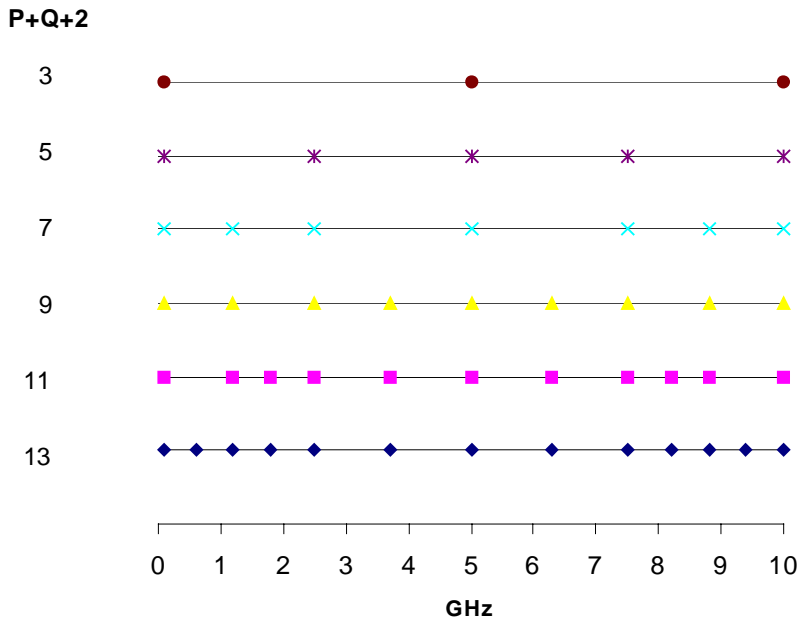


Figure 2.16: Frequencies where data points were sampled for the inductor structure.

Table 2.2: Minimum eigenvalue of the inductor structure as the order increases.

P	Q	P+Q+2	λ_{\min}
0	1	3	0.473955847
1	2	5	0.473955847
2	3	7	0.497262499
3	4	9	0.036331996
4	5	11	3.12502E-06
5	6	13	1.72215E-07

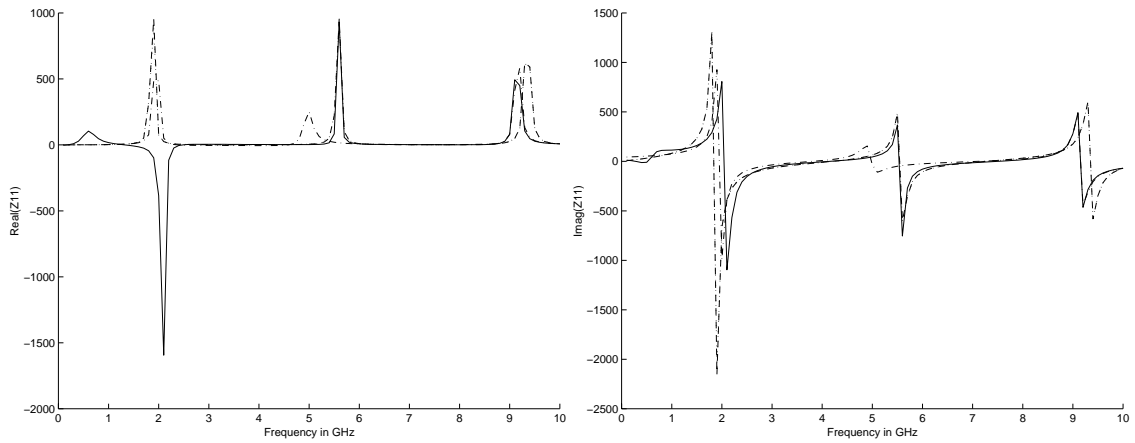


Figure 2.17: The interpolated response of the inductor as the number of data increases. Dashed dot - P=2 & Q=3, Solid - P=3 & Q=4, Dashed - P=4 & Q=5, Dotted - P=5 & Q=6.

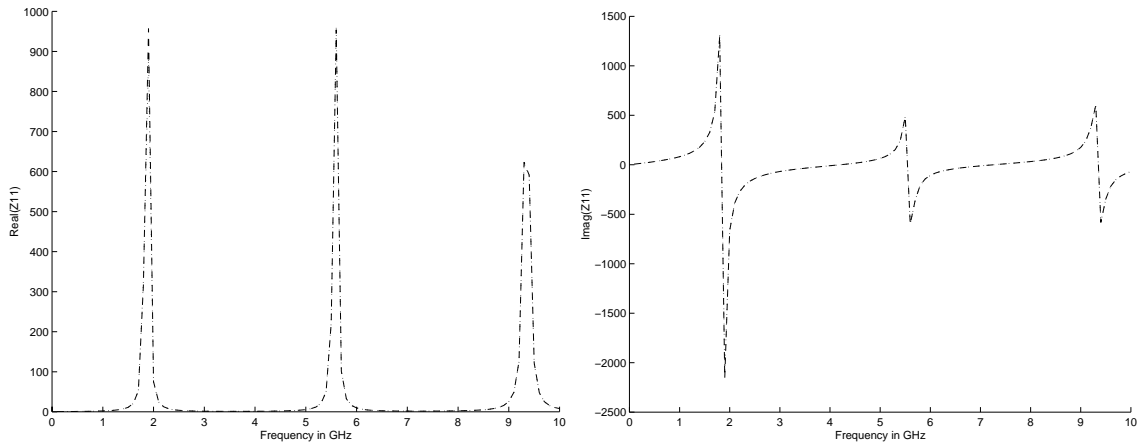


Figure 2.18: Full set of SONNET data and interpolated response of the inductor using minimum order P = 4 and Q = 5. Dotted - SONNET, dashed - rational function.

2.6.2 Capacitor

The sampling method was applied to the capacitor structure shown in Figure 2.5. The full-wave EM solver SONNET was used to generate data. Figure 2.19 shows the frequency points where data was sampled as the order was increased. Table 2.3 shows the corresponding minimum eigenvalues. Figure 2.20 shows the interpolated response of input admittance. The response converged when $P+Q+2$ reached 7 and 9, showing that the minimum number of data required for interpolation up to 4 GHz is seven.

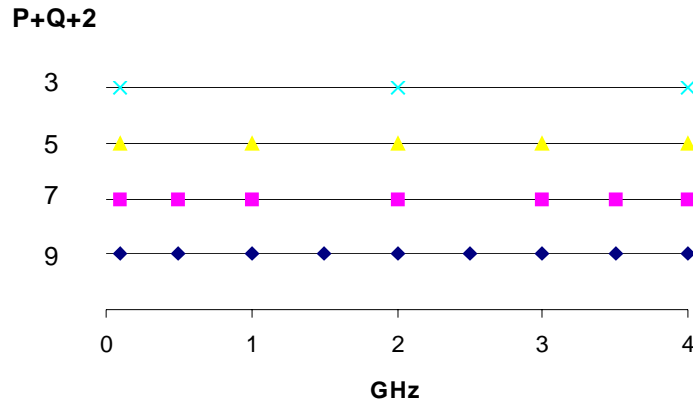


Figure 2.19: Frequency where data points were sampled for the capacitor structure.

Table 2.3: Minimum eigenvalue for the capacitor structure.

P	Q	P+Q+2	λ_{\min}
0	1	3	1.342775E-06
1	2	5	2.213852E-05
2	3	7	3.965071E-09
3	4	9	1.719493E-13

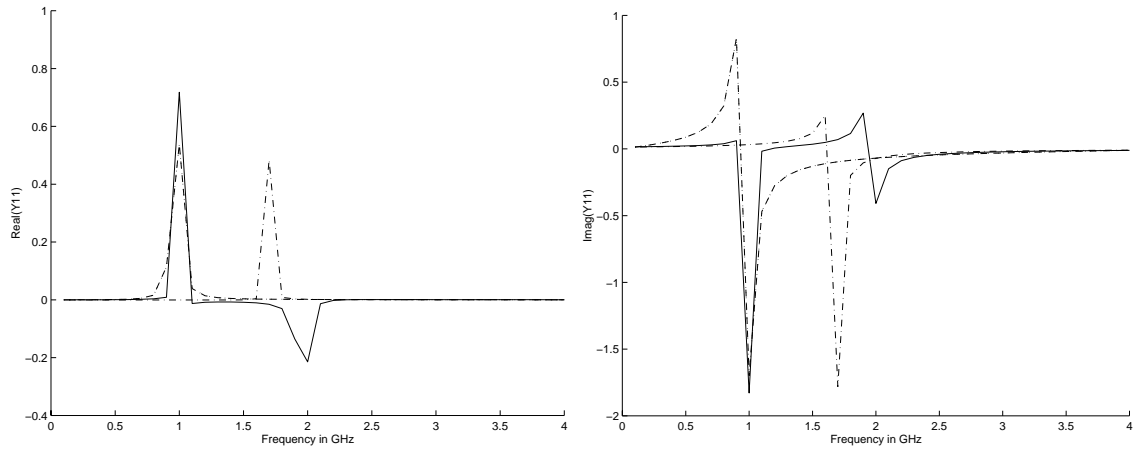


Figure 2:20: The interpolated response of the capacitor as the number of data increases.
 Dash dot - $P=0$ & $Q=1$, solid - $P=1$ & $Q=2$, dashed - $P=2$ & $Q=3$ (minimum order),
 dotted - $P=3$ & $Q=4$.

2.6.3 Resistor

The resistor structure shown in Figure 4.8 was interpolated using the data points as indicated in Figure 2.21. The data points were obtained using SONNET. Table 2.4 shows the corresponding minimum eigenvalues. Figure 2.22 shows the interpolated response of the input admittance as the order increases. The convergence occurred when $P+Q+2$ reached 5 and 7. The minimum number of data needed for interpolation up to 4 GHz was five.

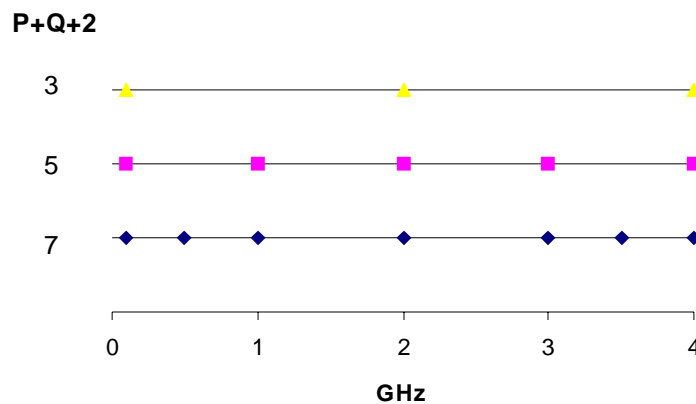


Figure 2.21: Frequencies where data points were sampled for the resistor structure.

Table 2.4: Minimum eigenvalue for the resistor structure.

P	Q	P+Q+2	λ_{\min}
0	1	3	1.993034E-04
1	2	5	1.710009E-08
2	3	7	8.770335E-11

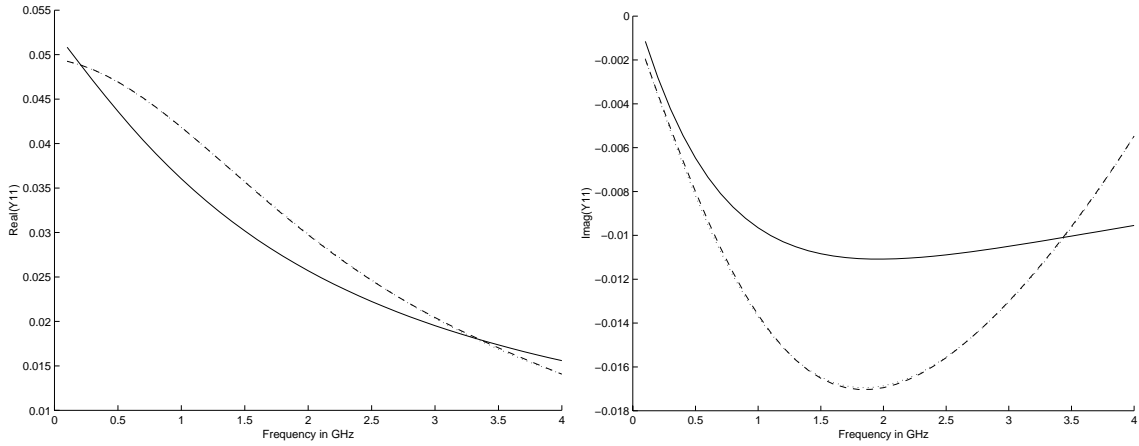
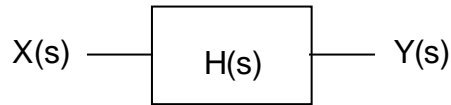


Figure 2.22: The interpolated response of the resistor as the number of data increases.
 Solid - P=0 & Q=1, dashed - P=1 & Q=2 (minimum order), dotted - P=2 & Q=3.

CHAPTER 3

TRANSIENT SIMULATION OF EMBEDDED PASSIVES USING MACROMODELS

Consider a linear system



that consists of an input $X(s)$ and output $Y(s)$. The output is related to the input through a transfer function

$$H(s) = \frac{Y(s)}{X(s)}.$$

Macromodels capture the $H(s)$ behavior of any structure, which can then be represented as a black box in a SPICE simulation. Figure 3.1 illustrates the concept for a two-port embedded structure.

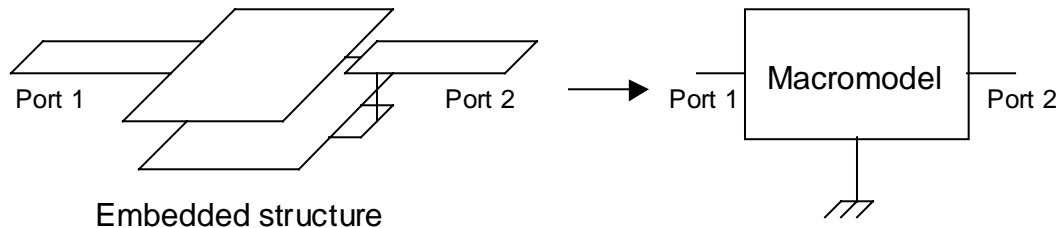
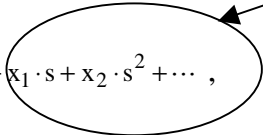


Figure 3.1: Macromodeling.

To implement macromodels in SPICE, the polynomial representation of the embedded structures is incorporated using Laplace function [39]. The previous chapter discusses an acceleration algorithm that interpolates a minimum number of data points and approximates the function as a ratio of two polynomials. However, the interpolation technique based on Cauchy's method in Section 2.2 does not generate rational functions that are suitable to be implemented in SPICE as a macromodel. The rational function must satisfy the following conditions for a passive circuit.

1. All the coefficients of the polynomials must be real. This results in real and complex conjugate poles and zeros that translate into sine, cosine, and exponential functions during convolution for time domain analysis. If poles (and zeros) are not complex conjugates of each other, inverse Laplace transform results in imaginary terms in time domain.
2. Polynomial functions representing the behavior of two-port or multiple port structures must have common poles for each function associated with each port.
3. All the poles of the polynomial function must be located on the left half plane. Otherwise, inverse Laplace transform results in unbounded exponential functions as its time variable approaches infinity.
4. The order of the numerator polynomial P must be less than or equal to the order of the denominator Q. If P is greater than Q, partial fraction expansion results in the following unwanted terms,

$$\frac{r_0}{s + p_0} + \frac{r_1}{s + p_1} + \dots + x_0 + x_1 \cdot s + x_2 \cdot s^2 + \dots ,$$


which translates to unrealizable derivatives of impulse response $\delta(t)$ (Dirac delta function) in time domain [36][37].

5. Rational function must be a positive real function. A function is a positive real function if the following two properties are satisfied [15][49]:
 - i) $Z_{in}(s)$ (or $Y_{in}(s)$) is real if s is real.

ii) $\text{Real}[Z_{in}(s)] \geq 0$ if $\text{real}[s] \geq 0$.

For embedded passives, this is not a serious condition because only a few dominant poles are required. See Section 4.1 in Chapter 4 for details.

To meet the required conditions above, some modification in the interpolation technique is required. Realization of the first condition is discussed in Section 3.1 while Section 3.2 discusses realization of the second condition. The third and fourth condition are related to stability and is discussed in section 3.5.

This chapter discusses a method for generating the macromodel. These macromodels are SPICE compatible and can be used in transient simulation. The results have been compared with TDR / TDT measurements [27] to show the accuracy and importance of the macromodels. The behavior of embedded passives in high-speed digital circuits has been discussed using simple examples [28]. The polynomial-generating technique described in this chapter was used by Dr. Heebyung Yoon (Ph.D, Georgia Tech) to perform pole/zero analysis in his fault detection and diagnosis technique for embedded passive components [40].

3.1 Generating A Function with Real Coefficient Polynomials

The resulting function from the interpolation algorithm in the previous chapter has complex coefficient polynomials. Some modification is necessary in the method to

generate real coefficients. They can be obtained by enforcing the condition that the coefficients, a_k and b_l , are real in (2.1). Consider a real coefficient polynomial function:

$$H(s) = \frac{\sum_{k=0}^P a_k \cdot s^k}{\sum_{l=0}^Q b_l \cdot s^l}, \quad (3.1)$$

where $s = j \cdot \omega$, ω is the angular frequency and a_k and b_l are real coefficients. The real coefficient function (3.1) is obtained by modifying (2.2) to the form

$$\sum_{k=0}^P a_k \cdot \text{Re}(s^k) - \sum_{l=0}^Q b_l \cdot \text{Re}(H(s) \cdot s^l) = 0 \quad (3.2a)$$

$$\sum_{k=0}^P a_k \cdot \text{Im}(s^k) - \sum_{l=0}^Q b_l \cdot \text{Im}(H(s) \cdot s^l) = 0 \quad (3.2b)$$

or in a matrix form

$$[A] = \begin{bmatrix} \text{Re}(s_1^0) & \text{Re}(s_1^1) & \cdots & \text{Re}(s_1^P) & \text{Re}(-H_1(s_1) \cdot (s_1^0)) & \text{Re}(-H_1(s_1) \cdot (s_1^1)) & \cdots & \text{Re}(-H_1(s_1) \cdot (s_1^Q)) \\ \text{Re}(s_2^0) & \text{Re}(s_2^1) & \cdots & \text{Re}(s_2^P) & \text{Re}(-H_2(s_2) \cdot (s_2^0)) & \text{Re}(-H_2(s_2) \cdot (s_2^1)) & \cdots & \text{Re}(-H_2(s_2) \cdot (s_2^Q)) \\ \vdots & \vdots & \vdots & \vdots & \vdots & \vdots & \vdots & \vdots \\ \text{Re}(s_m^0) & \text{Re}(s_m^1) & \cdots & \text{Re}(s_m^P) & \text{Re}(-H_m(s_m) \cdot (s_m^0)) & \text{Re}(-H_m(s_m) \cdot (s_m^1)) & \cdots & \text{Re}(-H_m(s_m) \cdot (s_m^Q)) \\ \text{Im}(s_1^0) & \text{Im}(s_1^1) & \cdots & \text{Im}(s_1^P) & \text{Im}(-H_1(s_1) \cdot (s_1^0)) & \text{Im}(-H_1(s_1) \cdot (s_1^1)) & \cdots & \text{Im}(-H_1(s_1) \cdot (s_1^Q)) \\ \text{Im}(s_2^0) & \text{Im}(s_2^1) & \cdots & \text{Im}(s_2^P) & \text{Im}(-H_2(s_2) \cdot (s_2^0)) & \text{Im}(-H_2(s_2) \cdot (s_2^1)) & \cdots & \text{Im}(-H_2(s_2) \cdot (s_2^Q)) \\ \vdots & \vdots & \vdots & \vdots & \vdots & \vdots & \vdots & \vdots \\ \text{Im}(s_m^0) & \text{Im}(s_m^1) & \cdots & \text{Im}(s_m^P) & \text{Im}(-H_m(s_m) \cdot (s_m^0)) & \text{Im}(-H_m(s_m) \cdot (s_m^1)) & \cdots & \text{Im}(-H_m(s_m) \cdot (s_m^Q)) \end{bmatrix} \quad (3.3)$$

and solving the equation:

$$[A][x] = 0. \quad (3.4)$$

Least squares method may be used to solve (3.4) [24]. The equation is rewritten as

$$[A]^H[A][x] = \lambda_{\min}[x]. \quad (3.5)$$

The solution vector $[x]$ is obtained by finding the eigenvector corresponding to λ_{\min} (or eigenvalue that is closest to zero) of the matrix $[A]^H[A]$. The matrix $[A]$ in (3.3) consists of real numbers. Thus, the elements of eigenvector of $[A]^H[A]$ is also real. The solution vector $[x]$ contains the real coefficients as follows:

$$[x] = [a_0 \ a_1 \ \dots \ a_p \ b_0 \ b_1 \ \dots \ b_Q]^T. \quad (3.6)$$

3.2 Generating Functions with Common Poles for Multiple-port Structures

The discussion in the previous section is based on generating a single function. It is useful for one-port structures that only require Z_{in} , Y_{in} or S_{11} etc. For multiple-port structures, either the admittance (y) parameter or impedance (z) parameter is approximated and represented by polynomial functions that have common poles. The technique in the previous section can be readily extended to two-port or other multiple-port networks. For example, a two-port structure has the admittance parameters y_{11} , y_{12} , y_{21} , and y_{22} . This can be represented in equation form as

$$\begin{pmatrix} I_1 \\ I_2 \end{pmatrix} = \begin{pmatrix} y_{11} & y_{12} \\ y_{21} & y_{22} \end{pmatrix} \cdot \begin{pmatrix} V_1 \\ V_2 \end{pmatrix}, \quad (3.7)$$

where

$$y_{11} = \frac{\sum_{k=0}^{P_1} a_{1,k} \cdot s^k}{\sum_{l=0}^Q b_l \cdot s^l} \quad y_{21} = y_{12} = \frac{\sum_{k=0}^{P_2} a_{2,k} \cdot s^k}{\sum_{l=0}^Q b_l \cdot s^l} \quad y_{22} = \frac{\sum_{k=0}^{P_3} a_{3,k} \cdot s^k}{\sum_{l=0}^Q b_l \cdot s^l} \quad (3.8)$$

In (3.8), the admittance parameters have a common denominator and hence the same poles. This constraint is enforced since the poles of a system cannot change and have to

remain constant for multiple ports. This also simplifies the enforcement of the stability condition. The coefficients, $a_{n,k}$ and b_j , are obtained by solving (3.5) where [A] is the matrix

$$[A] = \begin{bmatrix}
 \begin{array}{c} \text{Re}(s_{1,1}^0) \dots \text{Re}(s_{1,1}^{P_1}) \\ \vdots \\ \text{Re}(s_{1,m}^0) \dots \text{Re}(s_{1,m}^{P_1}) \\ \text{Im}(s_{1,1}^0) \dots \text{Im}(s_{1,1}^{P_1}) \\ \vdots \\ \text{Im}(s_{1,m}^0) \dots \text{Im}(s_{1,m}^{P_1}) \end{array} & \begin{array}{c} 0 \\ \vdots \\ 0 \end{array} & \begin{array}{c} \dots \\ \vdots \\ \dots \end{array} & \begin{array}{c} 0 \\ \vdots \\ 0 \end{array} & \begin{array}{c} \text{Re}(-H_1(s_{1,1}) \cdot (s_{1,1}^0)) \dots \text{Re}(-H_1(s_{1,1}) \cdot (s_{1,1}^Q)) \\ \vdots \\ \text{Re}(-H_1(s_{1,m}) \cdot (s_{1,m}^0)) \dots \text{Re}(-H_1(s_{1,m}) \cdot (s_{1,m}^Q)) \\ \text{Im}(-H_1(s_{1,1}) \cdot (s_{1,1}^0)) \dots \text{Im}(-H_1(s_{1,1}) \cdot (s_{1,1}^Q)) \\ \vdots \\ \text{Im}(-H_1(s_{1,m}) \cdot (s_{1,m}^0)) \dots \text{Im}(-H_1(s_{1,m}) \cdot (s_{1,m}^Q)) \end{array} \\
 \begin{array}{c} 0 \\ \vdots \\ 0 \end{array} & \begin{array}{c} \text{Re}(s_{2,1}^0) \dots \text{Re}(s_{2,1}^{P_2}) \\ \vdots \\ \text{Re}(s_{2,m}^0) \dots \text{Re}(s_{2,m}^{P_2}) \\ \text{Im}(s_{2,1}^0) \dots \text{Im}(s_{2,1}^{P_2}) \\ \vdots \\ \text{Im}(s_{2,m}^0) \dots \text{Im}(s_{2,m}^{P_2}) \end{array} & \begin{array}{c} \ddots \\ \vdots \\ \ddots \end{array} & \begin{array}{c} \vdots \\ \vdots \\ \vdots \end{array} & \begin{array}{c} \text{Re}(-H_2(s_{2,1}) \cdot (s_{2,1}^0)) \dots \text{Re}(-H_2(s_{2,1}) \cdot (s_{2,1}^Q)) \\ \vdots \\ \text{Re}(-H_2(s_{2,m}) \cdot (s_{2,m}^0)) \dots \text{Re}(-H_2(s_{2,m}) \cdot (s_{2,m}^Q)) \\ \text{Im}(-H_2(s_{2,1}) \cdot (s_{2,1}^0)) \dots \text{Im}(-H_2(s_{2,1}) \cdot (s_{2,1}^Q)) \\ \vdots \\ \text{Im}(-H_2(s_{2,m}) \cdot (s_{2,m}^0)) \dots \text{Im}(-H_2(s_{2,m}) \cdot (s_{2,m}^Q)) \end{array} \\
 \begin{array}{c} \vdots \\ \vdots \\ \vdots \end{array} & \begin{array}{c} \ddots \\ \vdots \\ \ddots \end{array} & \begin{array}{c} \ddots \\ \vdots \\ \ddots \end{array} & \begin{array}{c} 0 \\ \vdots \\ 0 \end{array} & \begin{array}{c} \vdots \\ \vdots \\ \vdots \end{array} \\
 \begin{array}{c} 0 \\ \vdots \\ 0 \end{array} & \begin{array}{c} \dots \\ \vdots \\ \dots \end{array} & \begin{array}{c} 0 \\ \vdots \\ 0 \end{array} & \begin{array}{c} \text{Re}(s_{n,1}^0) \dots \text{Re}(s_{n,1}^{P_n}) \\ \vdots \\ \text{Re}(s_{n,m}^0) \dots \text{Re}(s_{n,m}^{P_n}) \\ \text{Im}(s_{n,1}^0) \dots \text{Im}(s_{n,1}^{P_n}) \\ \vdots \\ \text{Im}(s_{n,m}^0) \dots \text{Im}(s_{n,m}^{P_n}) \end{array} & \begin{array}{c} \text{Re}(-H_n(s_{n,1}) \cdot (s_{n,1}^0)) \dots \text{Re}(-H_n(s_{n,1}) \cdot (s_{n,1}^Q)) \\ \vdots \\ \text{Re}(-H_n(s_{n,m}) \cdot (s_{n,m}^0)) \dots \text{Re}(-H_n(s_{n,m}) \cdot (s_{n,m}^Q)) \\ \text{Im}(-H_n(s_{n,1}) \cdot (s_{n,1}^0)) \dots \text{Im}(-H_n(s_{n,1}) \cdot (s_{n,1}^Q)) \\ \vdots \\ \text{Im}(-H_n(s_{n,m}) \cdot (s_{n,m}^0)) \dots \text{Im}(-H_n(s_{n,m}) \cdot (s_{n,m}^Q)) \end{array}
 \end{bmatrix} \tag{3.9}$$

and 'n' is the number of parameters to be solved for a common denominator. In the case of a two-port embedded structure, the value of 'n' is 3 and the functions H_1 , H_2 , and H_3 correspond to y_{11} , y_{21} , and y_{22} , respectively. (The y_{12} is not considered since it is the same as y_{21} for the passive structures.) The solution vector [x] contains the numerator coefficients, $a_{n,k}$, for each parameter along with the common denominator coefficients, b_j , as follows:

$$[\mathbf{x}] = [\mathbf{a}_{1,1} \ \mathbf{a}_{1,2} \ \dots \ \mathbf{a}_{1,m} : \mathbf{a}_{2,1} \ \mathbf{a}_{2,2} \ \dots \ \mathbf{a}_{2,m} : \dots : \mathbf{a}_{n,1} \ \mathbf{a}_{n,2} \ \dots \ \mathbf{a}_{n,m} : \mathbf{b}_1 \ \mathbf{b}_2 \ \dots \ \mathbf{b}_m]^T. \quad (3.10)$$

3.3 Generating Lossless Functions

Lossless functions may be generated if the loss of the structure is small and negligible. Lossless functions are desirable since they can be used to synthesize equivalent circuits that physically correlate with fewer number of elements, as will be demonstrated in the next chapter.

Lossless functions are derived in the form of a ratio of an even-powered polynomial to an odd-powered polynomial or vice versa. To illustrate the generation of such functions, the matrix [A] is represented with the following submatrices:

$$[\mathbf{B}] = \begin{bmatrix} s_1^0 & s_1^1 & \cdots & s_1^P \\ s_2^0 & s_2^1 & \cdots & s_2^P \\ \vdots & \vdots & \vdots & \vdots \\ s_m^0 & s_m^1 & \cdots & s_m^P \end{bmatrix} \quad (3.11)$$

and

$$[\mathbf{C}] = \begin{bmatrix} H(s_1) \cdot s_1^0 & H(s_1) \cdot s_1^1 & \cdots & H(s_1) \cdot s_1^Q \\ H(s_2) \cdot s_2^0 & H(s_2) \cdot s_2^1 & \cdots & H(s_2) \cdot s_2^Q \\ \vdots & \vdots & \vdots & \vdots \\ H(s_m) \cdot s_m^0 & H(s_m) \cdot s_m^1 & \cdots & H(s_m) \cdot s_m^Q \end{bmatrix}. \quad (3.12)$$

In the case of a one-port structure, the matrix [A] in (3,3) can be rewritten as

$$[A] = \begin{bmatrix} \text{Re}[B] & \text{Re}[C] \\ \text{Im}[B] & \text{Im}[C] \end{bmatrix}. \quad (3.13)$$

To generate lossless functions, the matrix $[A]$ in (3.3) is constructed with even columns of $[B]$ and odd columns of $[C]$ or vice versa. In the case of a two-port structure, the matrix $[A]$ in (3.9) can be rewritten as

$$[A] = \begin{bmatrix} \text{Re}[B_{11}] & 0 & 0 & \text{Re}[C_{11}] \\ \text{Im}[B_{11}] & 0 & 0 & \text{Im}[C_{11}] \\ 0 & \text{Re}[B_{21}] & 0 & \text{Re}[C_{21}] \\ 0 & \text{Im}[B_{21}] & 0 & \text{Im}[C_{21}] \\ 0 & 0 & \text{Re}[B_{22}] & \text{Re}[C_{22}] \\ 0 & 0 & \text{Im}[B_{22}] & \text{Im}[C_{22}] \end{bmatrix}, \quad (3.14)$$

where $[B_{11}]$ and $[C_{11}]$ are matrix $[B]$ in (3.11) and $[C]$ in (3.12), respectively, constructed using z_{11} data. $[B_{21}]$ and $[C_{21}]$ are constructed using z_{21} data, etc. To generate lossless functions, the matrix $[A]$ in (3.14) is constructed using even columns of $[B]$ and odd columns of $[C]$ or vice versa. All $[C]$ matrices must have the same Q .

3.4 Minimum Number of Data Needed

To develop rational functions with real coefficients, it is important to note that higher-order polynomials are required as compared with complex coefficient polynomials. Therefore, solving for a higher-order polynomial further requires more data points, which translates to more simulation time if directly coupled to an EM solver such as SONNET. To minimize the number of data points and hence minimize the EM

simulation time to obtain a suitable polynomial representation, interpolation can be first performed by computing the matrix $[A]$ in (2.4) and the complex coefficient function (2.1), which can then provide the required number of data points to solve for the real coefficient function. Once the complex coefficient function is found, a larger matrix $[A]$ in (3.3) is created with higher P and Q and m from the complex coefficient function. Based on experience, the order of P and Q for a real coefficient function is one more than that required for a complex coefficient function for the classes of embedded structures considered in this chapter.

However, it should be noted that it is not necessary to compute the solution of complex coefficients before computing the solution of real coefficients. The values of P and Q found by observing the λ_{\min} (as discussed in Chapter 2) are the minimum polynomial orders required to approximate a complex coefficient function using the minimum number of data points, $P+Q+2$. When the number of available data from EM solver is much larger than $P+Q+2$, the matrix $[A]$ in (3.3) for a one-port structure or the matrix $[A]$ in (3.9) for a multiple-port structure can be directly created from EM-generated data, bypassing the computation of complex coefficient solution. However, this is done at a cost of more EM simulation time.

3.5 Stability

Other than the real coefficient function and common pole (for multiple-port) requirements, the SPICE macromodel also requires two additional conditions related to

stability. The first condition is that all the poles of the function must be located on the left half plane. Another required condition is that the order of the numerator must be less than the order of the denominator.

The algorithm shown in the previous section does not guarantee a stable solution. The resulting function may have poles located in the right half plane. If the resulting function is stable with $P < Q$, no additional work is needed. If the resulting function has unstable poles, the following actions must be taken [27].

1. Change P and Q until a stable function is obtained. For example, if the function has one unstable pole, reduce the denominator order Q by one. The unstable pole may disappear. If there are many unstable poles, Q may be too high. Reduce Q appropriately and try again. Too much difference between the order P and Q may also be a cause for unstable poles. If Q is reduced, P may need to be reduced to some degree accordingly.
2. As P and Q are changed, be sure to keep P less than Q as it is also one of the required conditions. If it is not possible to produce an accurate curve-fitting function while maintaining P less than Q , a different parameter should be pursued. For example, if a function approximating input impedance Z_{in} is not satisfactory while keeping P less than Q , then, input admittance Y_{in} should be approximated instead.

3. A reasonable scaling factor should be used to generate an accurate solution. The optimum scaling factor was determined by checking the spread in the eigenvalues. A large spread may indicate that a more adequate scaling factor is needed.

By following the above guidelines, a stable solution could be always obtained for all the embedded passive components tested.

3.6 Implementation in SPICE

In the case of a one-port structure, a polynomial function representing either an input admittance or input impedance is needed. For the case of one-port structures, Table 3.1 shows a SPICE macromodel using input admittance (Y_{in}) and Table 3.2 using input impedance (Z_{in}). For two-port structures, Table 3.3 shows SPICE macromodel using admittance (y) parameter functions and Table 3.4 using impedance (z) parameter functions. The coefficients are defined in '.param' section.

Table 3.1: Macromodel for 1-port structure using input admittance.

```
.macro nport1 1 reference
g11 1 reference LAPLACE 1 reference a0,a1, ... ap / b0,b1, ... bq
.eom nport1
```

Table 3.2: Macromodel for 1-port structure using input impedance.

```
.macro nport1 port1 reference
v1 port1 1 0
f1 cnt1 0 v1 -1.0
r1 cnt1 0 1.0
e11 1 reference LAPLACE cnt1 0 a0, a1, ... ap / d0, d1, ... dq
.eom nport1
```

Table 3.3: 2-port macromodel using y-parameter functions.

```
.macro nport2 1 2 reference
g11 1 reference LAPLACE 1 reference a0,a1, ... ap1 / d0,d1, ... dq
g12 1 reference LAPLACE 2 reference b0,b1, ... bp2 / d0,d1, ... dq
g21 2 reference LAPLACE 1 reference b0,b1, ... bp2 / d0,d1, ... dq
g22 2 reference LAPLACE 2 reference c0,c1, ... cp3 / d0,d1, ... dq
.eom nport2
```

Table 3.4: Two-port macromodel using z-parameter functions.

```
.macro nport2 port1 port2 reference
v1 port1 1 0
f1 cnt1 0 v1 -1.0
r1 cnt1 0 1.0
v2 port2 2 0
f2 cnt2 0 v2 -1.0
r2 cnt2 0 1.0
e11 1 1_1 LAPLACE cnt1 0 a0,a1, ... ap1 / d0,d1, ... dq
e12 1_1 reference LAPLACE cnt2 0 b0,b1, ... bp2 / d0,d1, ... dq
e21 2 2_1 LAPLACE cnt1 0 b0,b1, ... bp2 / d0,d1, ... dq
e22 2_1 reference LAPLACE cnt2 0 c0,c1, ... cp3 / d0,d1, ... dq
.eom nport2
```

3.7 Simulation of SPICE Macromodels and Measurement Correlation

The SPICE macromodels were simulated in the time domain and correlated with time-domain reflectometry (TDR) and time-domain transmission (TDT) measurements. The measurement setup consisted of Tektronix 11801B digital sampling oscilloscope, SD-24 (20 GHz bandwidth) sampling heads with dual channels, Cascade Microtech G-S-G probes, Cascade Microtech probe station, and high-frequency Gore cables. Figure 3.2 shows the measurement setup where R is the resistor under test and Z_S and Z_I are terminating impedance of the digital sampling oscilloscope. A 250 mV step with a rise time of 35 ps was propagated on the structure and both the reflected and transmitted pulses were measured. The TDR and TDT measurement locations are indicated in Figure 3.2. Suitable SPICE models were developed of the setup to enable a macromodel to measurement correlation.

The technique was applied to two two-port embedded resistors shown in Figures 3.3 and 3.4. The structures were realized by LTCC technology. In Figures 3.3 and 3.4, metallization connecting to ports 1 and 2 provided access to the resistors through a coplanar transition. To develop SPICE macromodels for the resistors that had DC resistance of 26 Ω and 858 Ω , the polynomial orders $P=2$ and $Q=3$ were used to approximate the admittance parameters using complex coefficients, while $P=3$ and $Q=4$ were needed to represent the same response using real coefficients. A frequency scaling factor of 10^9 was used. The pole-zero plot of the 26 Ω resistor is shown in Figure 3.5 for the admittance parameter y_{11} represented using the rational function. As can be seen

from the figure, the poles are on the LHP. Figure 3.6 shows the frequency response of the $26\ \Omega$ resistor generated by SONNET [25] and the interpolated results indicating that the agreement is very good.

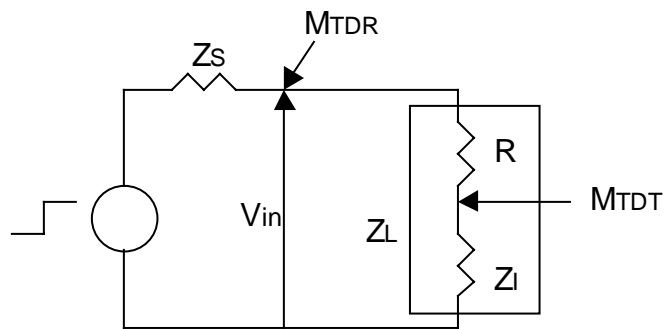


Figure 3.2: TDR / TDT measurement setup.

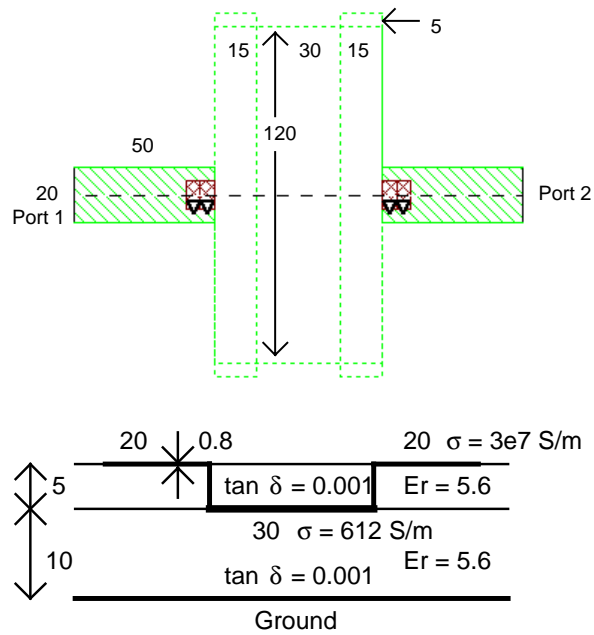


Figure 3.3: Top and side view of the $26\ \Omega$ resistor structure. The dimensional units are in mils.

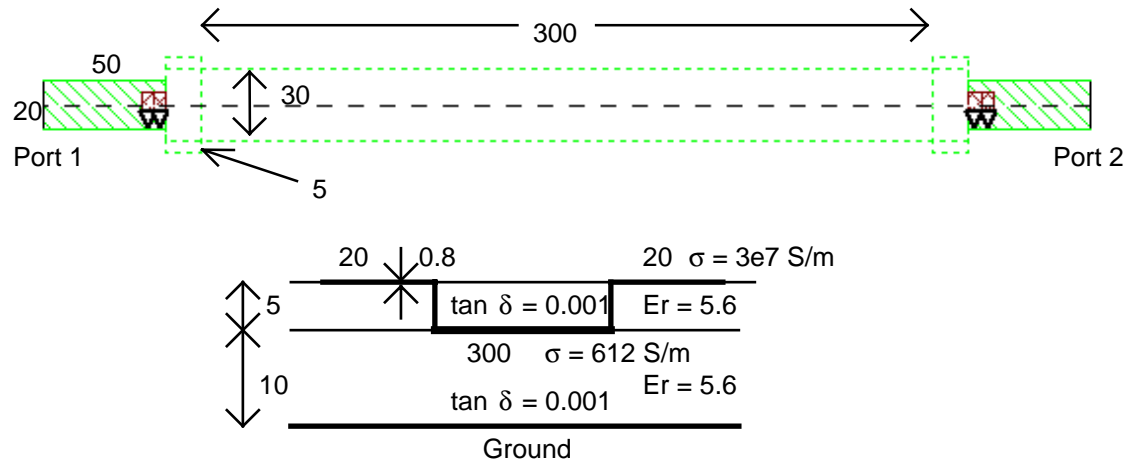


Figure 3.4: Top and side view of the 858 Ω resistor structure. The dimensional units are in mils.

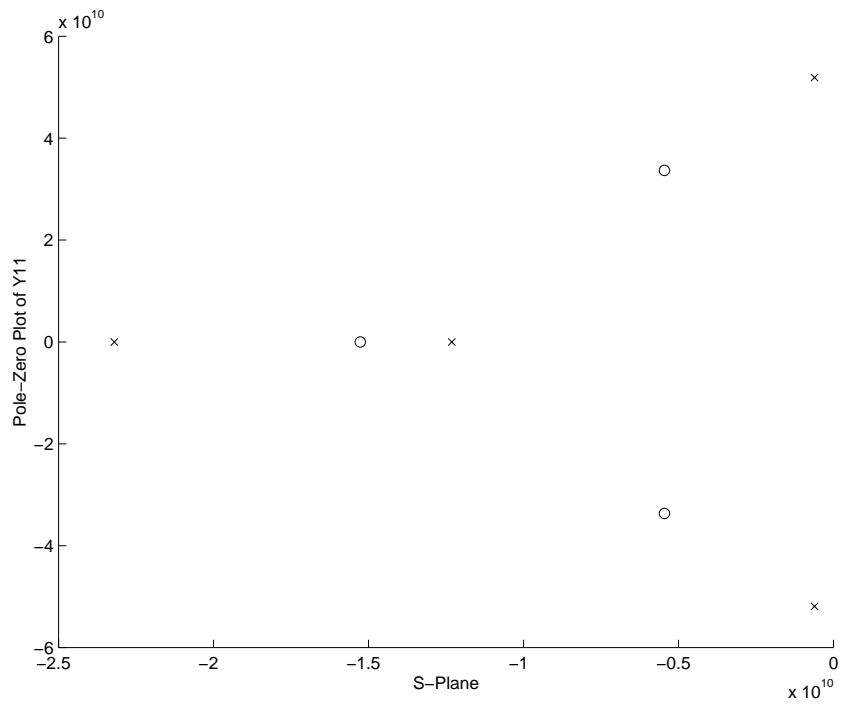


Figure 3.5: Pole-zero plot of y_{11} of 26 Ω resistor.

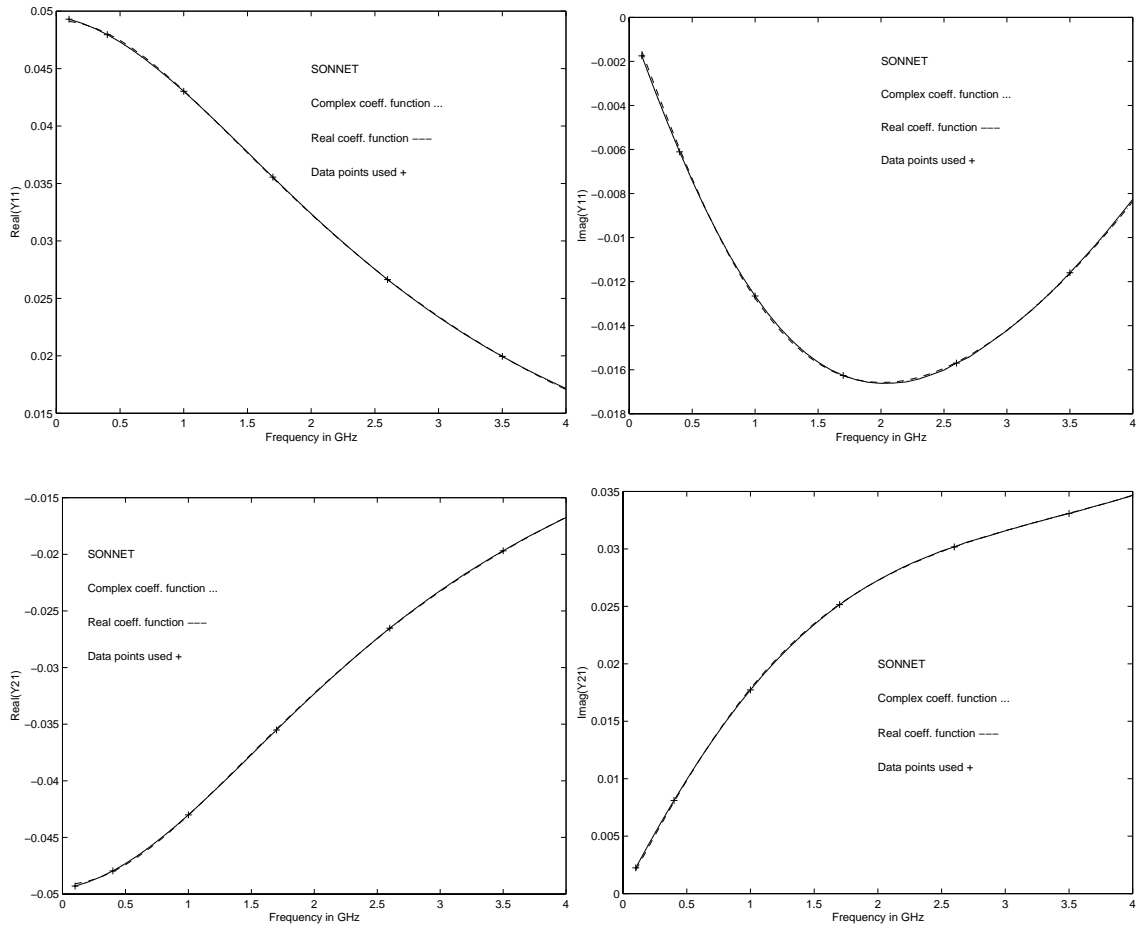


Figure 3.6: Admittance parameters of the 26 Ω resistor.

Figure 3.7 shows the measured and simulated TDR response of the 26 Ω embedded resistor. The initial negative peak represents the capacitance parasitic (between resistor and ground plane), which has been captured accurately by the macromodel. Figure 3.8 shows the measured and simulated TDT response for the 858 Ω resistor. Figure 3.8 consists of four waveforms, namely the measured TDT response, response using a simple resistor model, response using the macromodel, and a DC compensated macromodel response. Small positive peaks shown in the simulation using the simple lumped resistor model is due to high impedance (>50 ohm) transition in the test vehicle. The simulations using macromodels show good agreement with measurements in all cases as compared with the simple resistor model, clearly revealing frequency dependence and parasitics. The effect of rounding the pulse because of high frequency effects can be clearly seen in Figure 3.8 for the 858 Ω resistor, which has been captured accurately by the macromodel. The rounding and slanting of the pulse introduces appreciable delay at the 50% level, which cannot be duplicated using a simple resistor model. The 5mV difference in DC levels between measured values and simulated values in the TDT response can be attributed to the DC resistance of the resistor. The modeled resistance value of 858 Ω (specification) was measured to have a resistance of 868 Ω using an LCR meter. By adjusting the $a_{1,0}$, $a_{2,0}$, and $a_{3,0}$ terms in (3.8), the agreement between model and measurement was improved, as shown in Figure 3.8. This method of adjusting the low-frequency coefficients of the macromodel based on measurements has been called DC compensation in Figure 3.8.

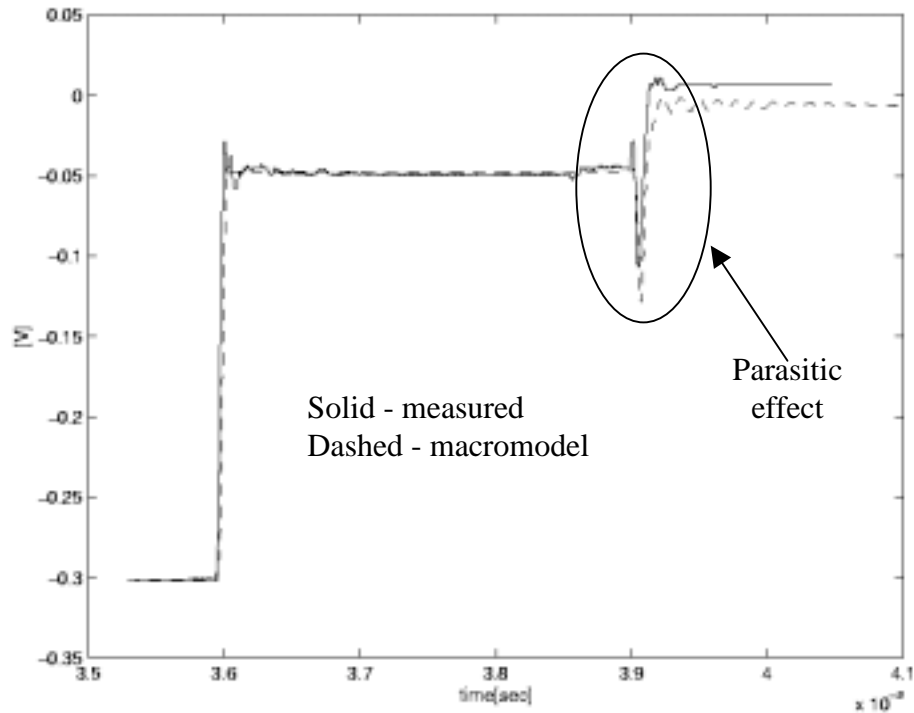


Figure 3.7: TDR response of 26 Ω resistor.

The macromodeling technique was next applied to a two-port embedded capacitor. Figure 3.9 shows the capacitor structure that was realized using LTCC technology. To develop the capacitor macromodel, the impedance parameters were approximated with $P=2$ and $Q=3$ using complex coefficients and $P=3$ and $Q=4$ using real coefficients. A frequency scaling factor of 10^9 was used. Figure 3.10 shows the SONNET-generated data and the rational function response for z_{11} in the frequency range DC - 4 GHz. The TDT response of the capacitor is shown in Figure 3.11. As can be clearly seen, the macromodel agrees very well with the measured TDT response, indicating that all the EM effects associated with the structure have been accurately captured.

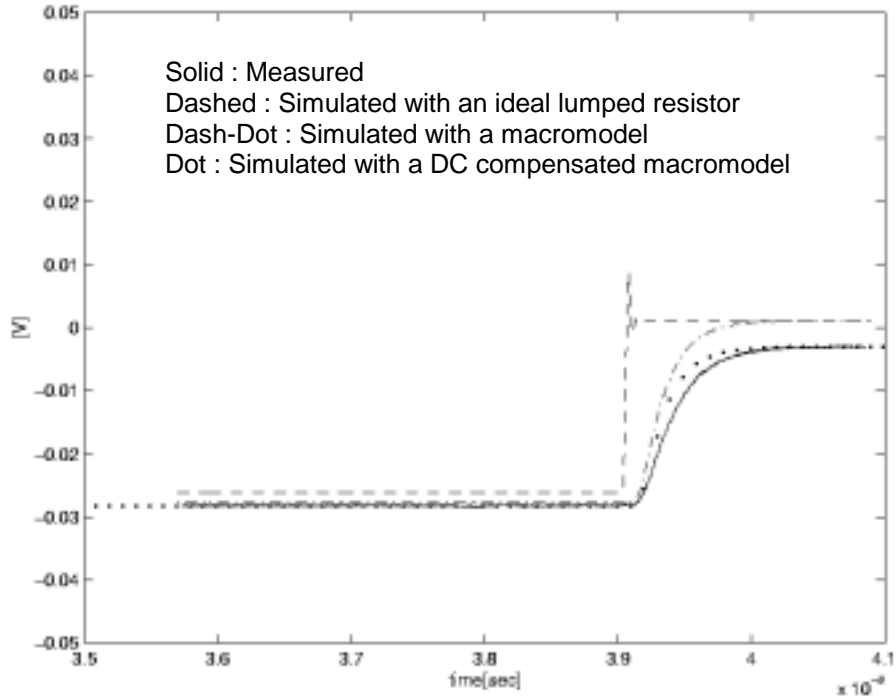


Figure 3.8: TDT response of 858 Ω resistor.

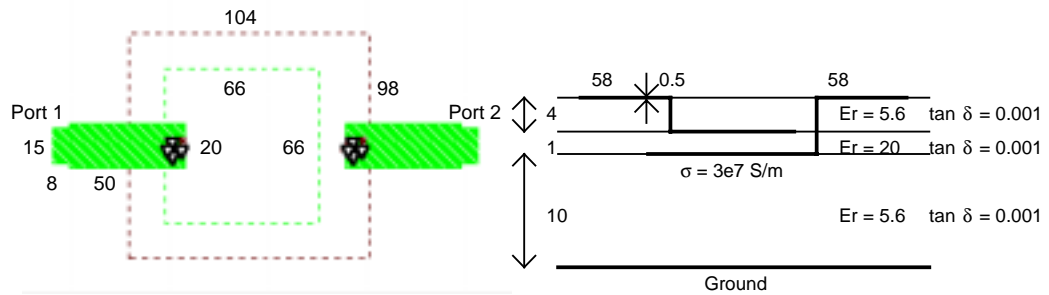


Figure 3.9: Capacitor structure. All dimensional units are in mils.

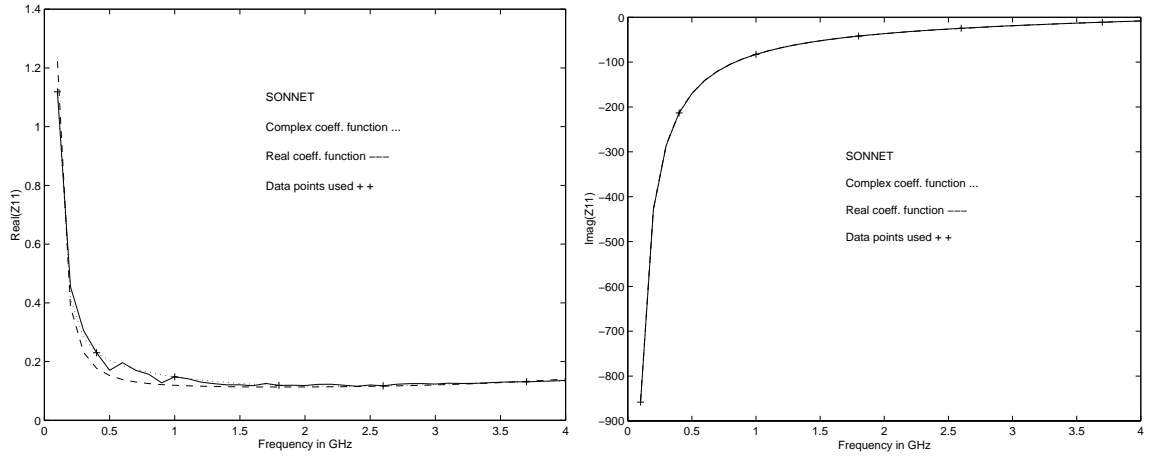


Figure 3.10: Response of SONNET and the equivalent circuit of the capacitor.

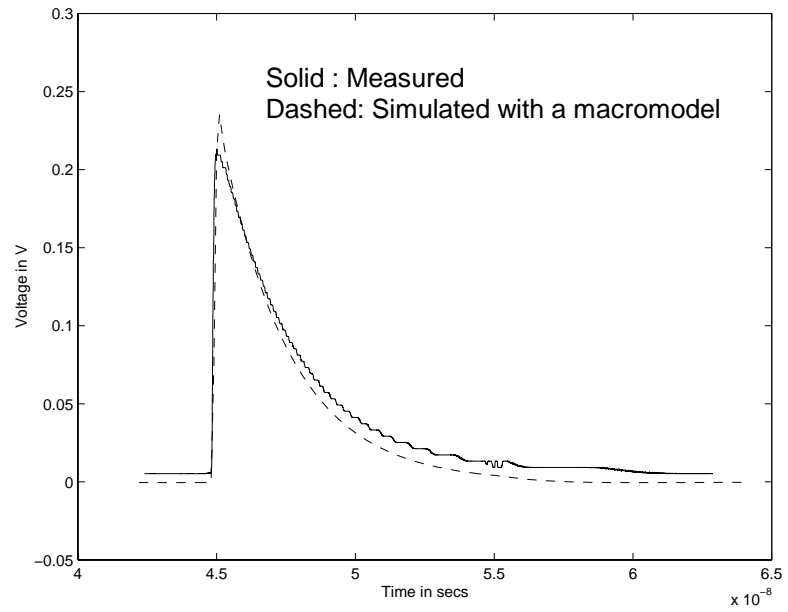


Figure 3.11: TDT response of the capacitor.

It is important to note that although the input pulse with a rise time of 35 ps has a 20 GHz bandwidth, a rational function that provided an accurate response in the frequency range DC - 4 GHz was sufficient to provide an accurate response in the time domain. This greatly simplifies and reduces the analysis of such structures.

3.8 Embedded Resistors in High-speed Digital Circuits

This section discusses the use of embedded resistors (as an example) in high speed digital circuits [28]. Simple circuits have been used to elaborate the importance of parasitics and frequency dependence on the behavior of embedded resistors and similar embedded passive structures. All results in this section are based on macromodels embedded in a SPICE simulation and have been used to generate the results.

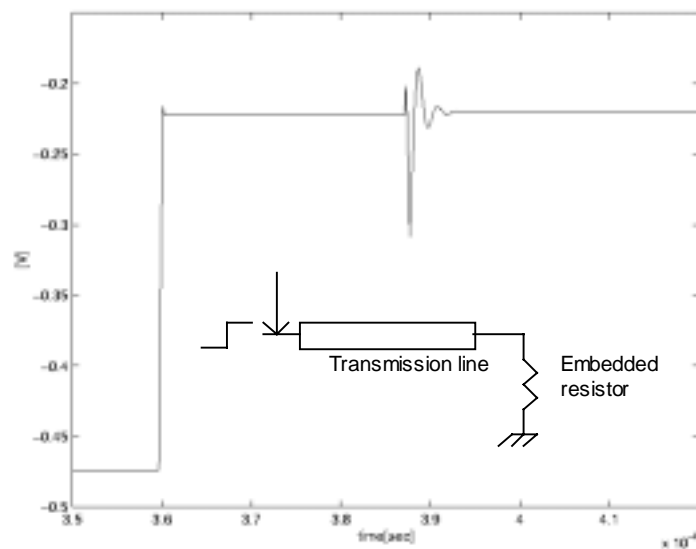


Figure 3.12: Transient response of a transmission line terminated with matching impedance of embedded resistor.

To study the effect of terminating digital transmission lines using embedded resistors, a $50\ \Omega$ transmission line terminated with a $50\ \Omega$ embedded resistor was simulated using a step with a 35 ps rise time. Because of the capacitive and inductive nature of the resistor, the ringing in the reflected response can be seen in Figure 3.12, which can cause problems in high speed circuits. This ringing would be absent with an ideal resistor. Next, two voltage divider networks (typically used in Analog-Digital converters) using two embedded resistors and two ideal resistors were simulated using a 35 ps rise time pulse, as shown in Figures 3.13 and 3.14. In Figure 3.13, the $858\ \Omega$ resistor divider network causes a considerable slow down of the rise time, while the $26\ \Omega$ resistor network causes oscillations, as shown in Figure 3.14. In both Figures 3.13 and 3.14, the response at the output is shown and is substantially different from the ideal resistor response. Hence, though a simple divide-by-two voltage divider network has been used, the response is largely dependent on the physical structure and the associated parasitics. Thus, considerable emphasis in designing embedded resistors is necessary for high-speed circuits.

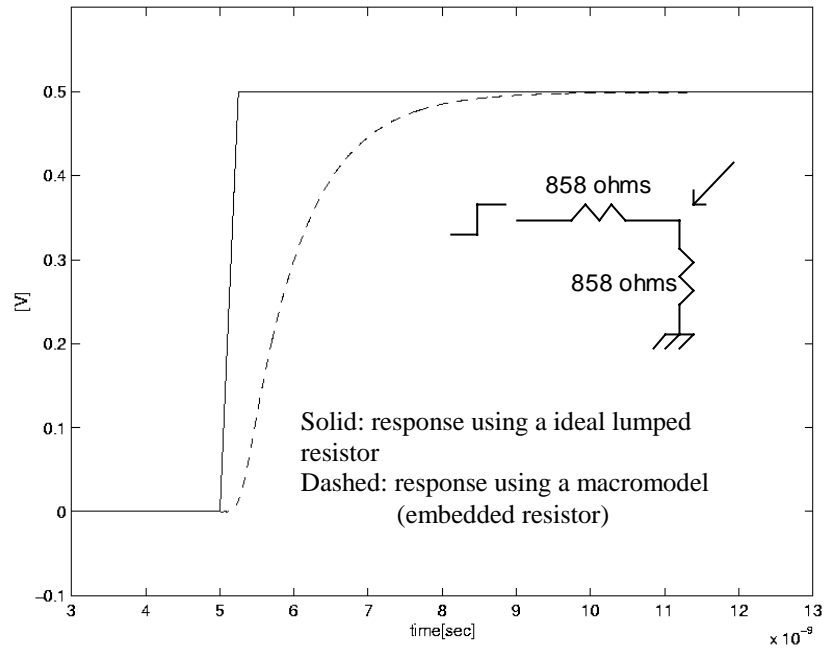


Figure 3.13: Transient response of 858 Ω resistor.

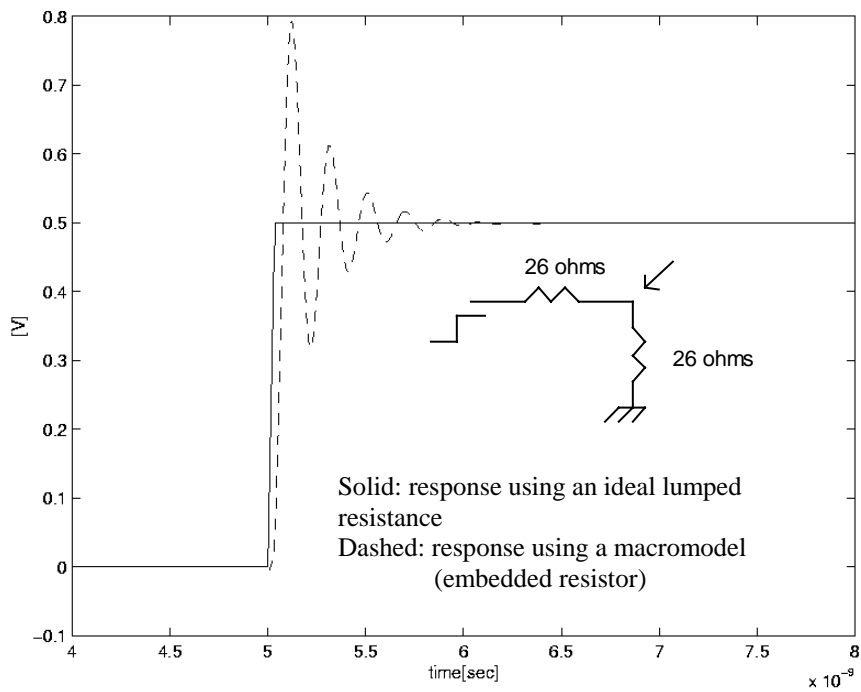


Figure 3.14: Transient response of 26 Ω resistor for a step input with 35 ps rise time.

CHAPTER 4

Equivalent Circuit Synthesis

The design of circuits with integral components such as resistors, inductors and capacitors is nontrivial because of the electromagnetic interactions causing parasitics, leading to nonideal frequency behavior. For example, a spiral inductor integrated into the substrate may resonate at discrete frequencies, thus limiting its frequency of operation, as shown in Figure 2.6. The quality factor (Q) of the inductor may also degrade because of the conductor losses in the structure. Hence, accurate models of integral components at RF frequencies are required.

Most RF design systems require an equivalent circuit to capture the response of a device. Though these systems have the capability to accept scattering parameters (s-parameters) directly, equivalent circuits are often preferred since they help in fine tuning the manufacturing process. The current practice for the derivation of a lumped model for an embedded passive structure involves a careful selection of a trial lumped model based on the physical layout and the skill of the designer. The value of each element is then optimized to give a best fitting response [14]. If the chosen lumped model does not produce satisfying results for the frequency bandwidth of interest, the model is abandoned and a new trial model is selected. This method obviously has many disadvantages. First, this is a very tedious and time consuming process and is heavily dependent on the skill of the designer. Second, the effects of the parasitics often tend to

increase as the size of the structure becomes larger. A lumped model selected for a small size structure may not produce reliable result for the same structure of larger size. Third, this method is more suitable for simple structures at low frequencies and can produce erroneous results at RF frequencies where tight tolerance of the specifications is required.

In this chapter, a method is presented to synthesize lumped-element circuits of RF components. Though integral passives have been analyzed in this paper, the method developed is general and can be applied to any passive structure. In Chapter 2, an interpolation technique was discussed which used a small number of data points to generate the broadband response of a RF component [19]. The method used data from an electromagnetic (EM) simulator to generate a rational function. The technique was modified in Chapter 3 to generate a rational function with real coefficients [27],[29]. The polynomial function was used to obtain the transient response using a SPICE simulator. In this chapter, the rational functions with real coefficients have been used to synthesize lumped element equivalent circuits. Careful attention has been paid to ensure that the equivalent circuits contain mainly positive components that correlate with the physical layout of the structure. The circuit topology generated by the circuit synthesis technique provides ground work in developing scalable models. The equivalent circuits provide connectivity between the physical parameters of the structure and the electrical parameters of the circuit, which may be analyzed to develop scalable models [41]. Scalable models may be incorporated in a design kit as discussed in [35]. Design kits provide an iterative technique that uses a library of components for designing a circuit and takes a minimum simulation time due to use of scalable models. Once the models

are available, they could be incorporated into a Hewlett Packard's Series IV (Libra) type framework. Design kits play a critical role in the design of precision RF components since this provides a CAD framework for RF designers to gain access to accurate models to be able to predict electrical performance prior to fabrication.

4.1 Synthesizable Rational Functions

The rational functions are synthesizable into networks only if it is a positive real function, which has the following properties [15][49]:

- 1) $Z_{in}(s)$ (or $Y_{in}(s)$) is real if s is real.
- 2) $\text{Real}[Z_{in}(s)] \geq 0$ if $\text{real}[s] \geq 0$.

The following properties are implied by the properties of positive real function [15][49]:

- 1) A rational function must have real coefficients. This condition is enforced in (3.2) by separating the real and imaginary parts of the matrix $[A]$.
- 2) All poles and zeros of the rational function lie on the left half plane. This condition results in a rational function with all positive coefficients. This condition is enforced by retaining the left half plane poles and updating the corresponding residues, as discussed in Section 5.1.

- 3) If the function has any pole on the $j\omega$ axis, it must be simple and have a real and positive residue. Same condition must hold for the reciprocal of the rational function.
- 4) The real part of the rational function must never be less than zero. This is obtained by bandlimiting the response and testing the response over the frequency band of interest. Since the circuits are used for RF simulation, this is an acceptable condition.

These properties need to be observed to verify a rational function generated by the interpolation technique is synthesizable.

4.2 Synthesis of One-port Network

Equivalent circuits for 1-port integral passive structure are obtained by synthesizing a rational function approximating the input impedance or admittance of the structure. Chapter 3 discusses the details on generating the required function.

Consider a synthesizable and frequency-normalized function which represents the driving-point input impedance or admittance of a 1-port network,

$$H(s) = \frac{\sum_{k=0}^P a_k \cdot s^k}{\sum_{l=0}^Q b_l \cdot s^l}, \quad (4.1)$$

where all the coefficients are real and positive. From $H(s)$, an equivalent circuit is synthesized through subtraction of certain functions or a constant which can then be realized using lumped components such as inductors, capacitors and resistors. Continual subtraction reduces the order of the polynomial until no more subtractions are possible. The following steps outline the procedure of the synthesis technique for 1-port structure.

1. Given $H(s)$, if the numerator has less coefficients than the denominator, invert $H(s)$ for further processing. For example, if $Z(s)$ (z-parameter) has $P=3$ and $Q=4$, convert it to $Y(s)$ by inversion. No subtraction is performed unless the number of coefficients in the numerator is greater than or equal to the denominator.
2. One of the following subtractions is performed to remove either the first or last coefficient term in the numerator.

Function to be subtracted has	What to subtract (ohm or mho)	Component
Pole at $s=\infty$	$x \cdot s$	L in ohm or C in mho
Pole at $s=0$	$1/(x \cdot s)$	C in ohm or L in mho
No pole at either $s=\infty$ or 0	X	R

The value of 'x' is either the first term of the numerator over the first term of the denominator or the last term of the numerator over the last term of the denominator. When a resistor is subtracted, four ways to choose 'x' are possible.

The value 'x' is chosen by ensuring that the remainder has all positive coefficients since positive components are desired in the equivalent circuit.

3. After the subtraction, the coefficients of the remainder are examined. A requirement for non-negative components in the equivalent circuit is that all the coefficients after subtraction have the identical sign (say all positive). Steps 1 and 2 are repeated until no more subtraction is possible.
4. After obtaining the equivalent circuit, the frequency dependant components, inductors and capacitors, are denormalized by dividing every inductance and capacitance by the frequency scaling factor.

To illustrate the synthesis procedure, a specific example is considered. Let $H(s)$ be the input impedance, $Z_{in}(s)$, with $P=1$ and $Q=2$. $Z_{in}(s)$ is represented in the frequency domain as

$$Z_{in}(s) = \frac{a_0 + a_1 \cdot s}{b_0 + b_1 \cdot s + b_2 \cdot s^2} \quad (4.2)$$

Using Step 1, the input admittance $Y_{in}(s)$ is obtained by inverting $Z_{in}(s)$ to form $Y_{in}(s)$,

$$Y_{in}(s) = \frac{b_0 + b_1 \cdot s + b_2 \cdot s^2}{a_0 + a_1 \cdot s} \quad (4.3)$$

$Y_{in}(s)$ has a pole at $s = \infty$. The pole is removed by subtracting from $Y_{in}(s)$ a function which removes the term, b_2s^2 , in the numerator. The remainder y_2 after subtraction is

$$y_2 = Y_{in} - \frac{b_2}{a_1} \cdot s = \frac{c_0 + c_1 \cdot s}{a_0 + a_1 \cdot s}, \quad (4.4)$$

where

$$c = \begin{bmatrix} b_0 \\ b_1 - \frac{1}{a_1} \cdot b_2 \cdot a_0 \end{bmatrix}. \quad (4.5)$$

A capacitor is extracted by subtracting $(b_2/a_1) \cdot s$ in mhos with the capacitance value of b_2/a_1 F. The remainder y_2 has the same number of coefficients in both the numerator and the denominator. It does not have the pole either at $s = \infty$ or $s = 0$. In such cases, y_2 is subtracted by frequency independent constants to remove either a first or last coefficient term in the numerator. The subtraction yields a resistor. Let y_3 be the remainder after subtraction. Since four possibilities exist for the subtraction of the resistor, an appropriate subtraction is chosen to yield y_3 with all positive coefficients. The four cases are shown below:

$$y_2 - \frac{c_1}{a_1} \quad y_2 - \frac{c_0}{a_0} \quad z_2 - \frac{a_1}{c_1} \quad z_2 - \frac{a_0}{c_0} \quad (4.6)$$

If the second extraction yields the remainder with all positive coefficients and is chosen for subtraction, then

$$y_3 = y_2 - \frac{c_0}{a_0} = \frac{d \cdot s}{a_0 + a_1 \cdot s} \quad (4.7)$$

where

$$d = \frac{a_0 \cdot c_1 - c_0 \cdot a_1}{a_0} \quad (4.8)$$

A resistor is extracted with its admittance of c_0/a_0 mhos. The coefficient term c_0 in y_2 is removed. The remaining elements are easily extracted by inverting y_3 to form z_3 where,

$$z_3 = \frac{a_0 + a_1 \cdot s}{d \cdot s} = \frac{a_0}{d \cdot s} + \frac{a_1}{d} \quad (4.9)$$

Figure 4.1 shows the resulting equivalent circuit.

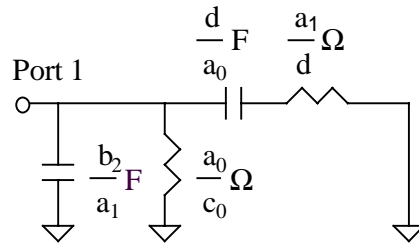


Figure 4.1: Equivalent circuit after synthesis of $Z_{in}(s)$ in (4.2).

It is important to note that the synthesis only results in ladder circuits such as the one shown in Figure 4.1. Non-ladder circuits, such as the one shown in Figure 4.2, are not synthesizable.

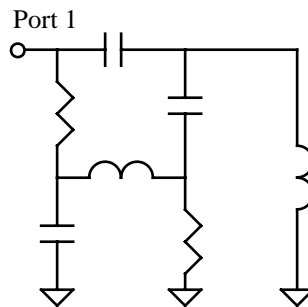


Figure 4.2: Example of non-ladder circuit.

4.3 Examples of Equivalent Circuits for One-port Structures

The synthesis technique was applied to a 1-port inductor, capacitor and resistor structure. They were realized by ground rules based on LTCC technology. The input impedance or admittance was approximated as a polynomial function with real coefficients using the interpolation technique discussed in Chapter 3. The equivalent circuits were synthesized from the resulting functions. The response of all the equivalent circuits is accurate over the frequency band DC – 4 GHz unless stated otherwise.

4.3.1 Inductor

The synthesis technique presented in this paper was applied to a 1-port embedded inductor structure. Low Temperature Cofired Ceramic (LTCC) technology ground rules were used to define the structure of the inductor. Two separate sets of materials from two different companies were used for the study. SONNET produced good correlation with measurements on some structures and hence was used to generate the frequency response for the structure. The physical dimensions of the metalization, shown in Figure 4.3, were kept constant, but other material and physical parameters, such as ϵ_r and thickness of the dielectric layers and location and conductivity of the metal, were varied to observe changes in the corresponding equivalent circuit. For each case, a full wave EM simulator SONNET was used to simulate the structure and a set of scattering parameter data was obtained. The scattering parameter data was converted to impedance parameter data and the input impedance was approximated using the interpolation technique to produce a

polynomial function with real coefficients. For all cases, a synthesizable function was obtained.

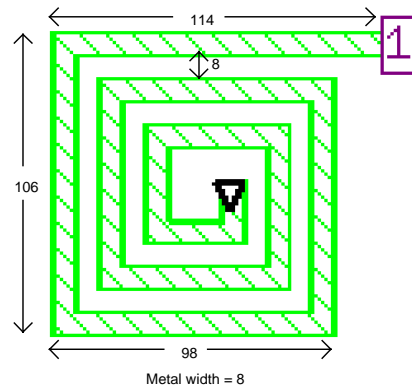
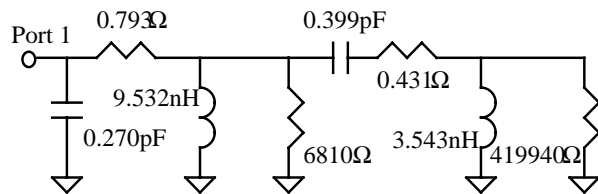


Figure 4.3: Metal dimensions of the inductor. The dimensional units are in mils.

Table 4.1 lists the cross section of the varying parameters of the inductor in Figure 4.3 and the corresponding equivalent circuit obtained using the synthesis procedure. As mentioned earlier, the synthesis only results in ladder type circuits. For example, after the synthesis, L1 in the Table 4.1 had the following ladder type equivalent circuit,



The equivalent circuits shown in Table 4.1 were redrawn from the original ladder circuits in a way that the readers can easily understand their physical correlation. Figure 4.4

shows the frequency response of the inductor L1. The response of the equivalent circuit was generated from SPICE and compared to the simulated response generated from SONNET. They agree accurately as shown.

The equivalent circuits shown in Table 4.1 were redrawn from the ladder circuits in a way that the readers can easily understand their physical correlation. Figure 4.4 shows the response of the inductor structure L1 in Table 4.1. The response of the equivalent circuit was compared to the full set of SONNET-generated data. They agree accurately as shown.

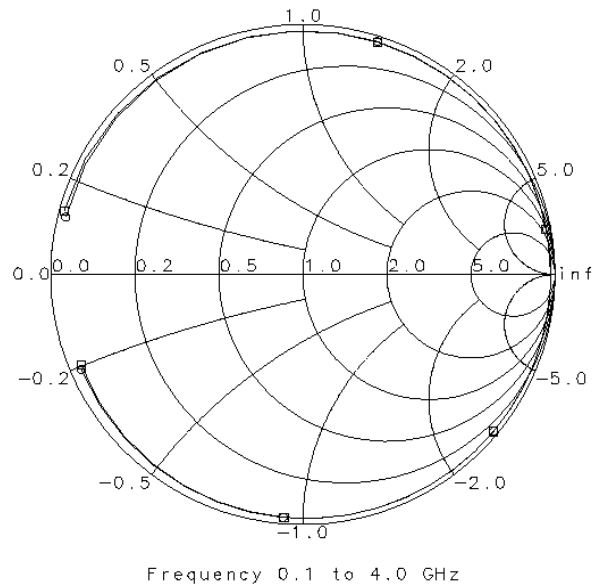


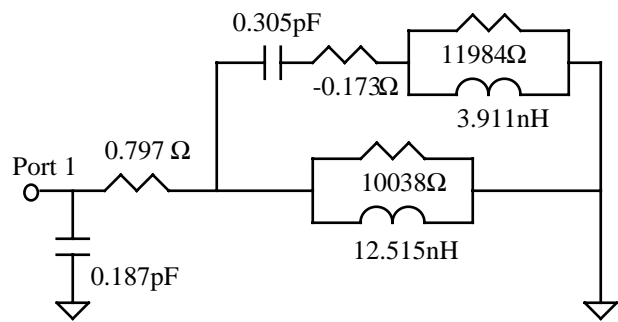
Figure 4.4: S11 response of SONNET (square) and the equivalent circuit (circle) of the inductor structure L1 in Table 4.1.

Table 4.1: Equivalent circuits as material and physical parameters of the inductor were varied. All dimensional units are in mils.

Name	Side-view of the Inductor	Equivalent Circuit
L1	<p> $\sigma = 3e7 \text{ S/m}$ Metal 0.5 Er = 5.6 $\tan \delta = 0.001$ Er = 5.6 $\tan \delta = 0.001$ Ground </p>	<p> Port 1 0.793 Ω 0.399 pF 0.431 Ω 419940 Ω 3.543 nH 6810 Ω 9.532 nH 0.270 pF </p>
L2	<p> $\sigma = 3e7 \text{ S/m}$ Metal 0.5 Er = 7.8 $\tan \delta = 0.001$ Er = 7.8 $\tan \delta = 0.001$ Ground </p>	<p> Port 1 0.658 Ω 0.483 pF 0.419 Ω 26076 Ω 4.158 nH 5381 Ω 9.289 nH 0.486 pF </p>
L3	<p> $\sigma = 3e7 \text{ S/m}$ Metal 0.3 Er = 7.8 $\tan \delta = 0.0035$ Er = 7.8 $\tan \delta = 0.0035$ Ground </p>	<p> Port 1 0.909 Ω 0.702 pF 0.263 Ω 12360 Ω 2.952 nH 3201 Ω 8.339 nH 0.361 pF </p>
L4	<p> $\sigma = 3e7 \text{ S/m}$ Metal 0.5 Er = 5.6 $\tan \delta = 0.001$ Ground </p>	<p> Port 1 0.115 pF 55018 Ω 2.699 nH 0.156 Ω 0.9840 nH 0.738 Ω 0.399 pF 28411 Ω </p>
L5	<p> $\sigma = 3e7 \text{ S/m}$ Metal 0.5 Er = 7.8 $\tan \delta = 0.001$ Ground </p>	<p> Port 1 0.548 Ω 0.305 pF 0.099 Ω 11408 Ω 3.911 nH 10482 Ω 12.515 nH 0.187 pF </p>

Many interesting observations were made after synthesizing the inductor with different parameters. The low frequency reactance (at about 0.2 GHz), when converted to an inductance, showed up as one of the components in the equivalent circuit. The low frequency inductance was reduced when the metal winding was moved from the surface and embedded in the middle of the substrate with other parameters kept unchanged. For instance, the low frequency inductance, 12.515 nH, of L5 was reduced to 9.289 nH in L2. The low frequency inductance, 12.539 nH (that is 2.699 nH + 9.840 nH), of L4 was reduced to 9.532 nH in L1. As ϵ_r of the dielectric layers was increased from 5.6 (L1) to 7.8 (L2), the capacitance between the input port and the ground in the equivalent circuit was significantly increased. The microstrip inductors had lower capacitance than the embedded inductors due to air and larger spacing between the metal winding and the ground plane. The low frequency inductance was also reduced from 9.532 nH (L1) to 9.289 nH (L2).

When synthesis was applied to inductor L5, a negative component value was unavoidable. The following equivalent circuit was obtained,



which contains a negative resistor. After investigation, it was found that the real part of the transfer function of the input impedance, $\text{Real}[Z_{in}(s)]$, had a large error compared to the simulated data in extremely low frequency region. The error was due to the offset of the two frequency independent terms, a_0 and b_0 , in (4.1). When a_0 was slightly adjusted to give a minimal error at the low frequency region, all positive value components were obtained. Table 4.1 shows the resulting circuit for L5 with all positive components.

4.3.2 Capacitor

For the capacitor structure shown in Figure 4.5, an equivalent circuit as shown in Figure 4.6 was synthesized. In Figure 4.6, the low frequency capacitance between the two metal plates is captured by C2 (19.07 pF) while the effect of the interconnects is captured by L1 and L2. The inductance L2 is larger than L1 since it includes the via for the short. Figure 4.7 shows the S11 response of SONNET and the equivalent circuit.

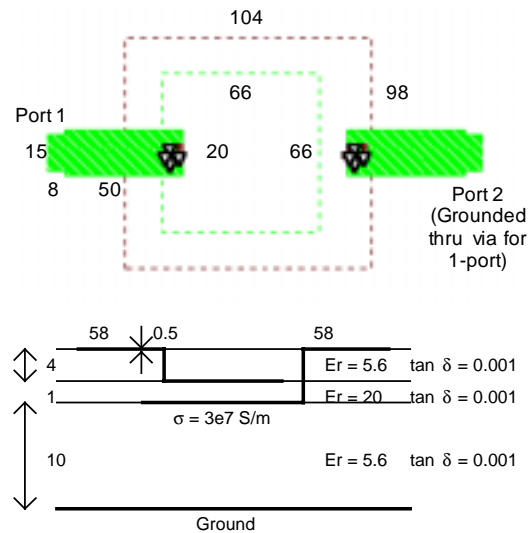


Figure 4.5: A capacitor structure. All dimensional units are in mils.

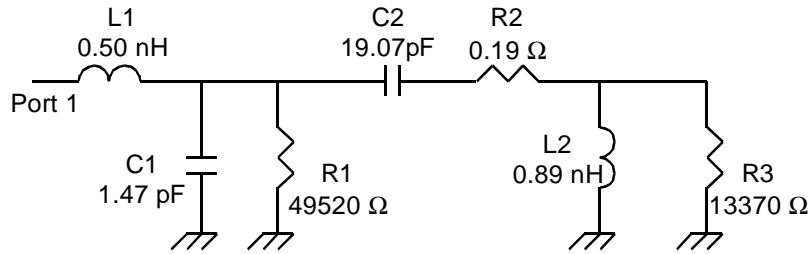


Figure 4.6: Equivalent circuit of the 1-port capacitor in Figure 4.5.

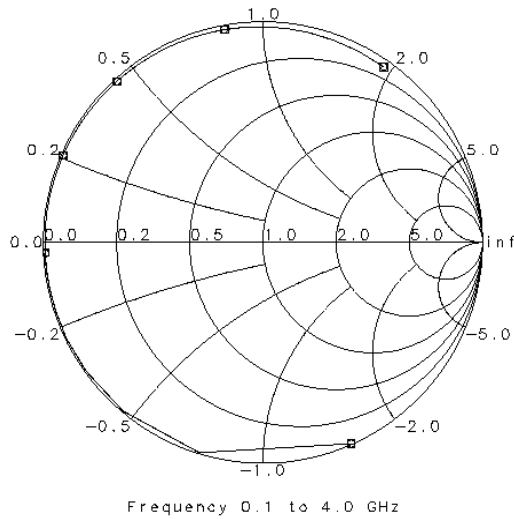


Figure 4.7: Response of SONNET (square) and the equivalent circuit (circle) of the capacitor in Figure 4.5.

4.3.3 Resistor

For the resistor structure in Figure 4.8, an equivalent circuit as shown in Figure 4.9 was synthesized. The synthesis resulted in an unavoidable negative resistor which was replaced by a current controlled voltage source. The resistor R1 captures the DC resistance of the resistor and the remaining elements represent parasitic effects. The

negative resistor can be viewed as a correction factor required to obtain the appropriate response.

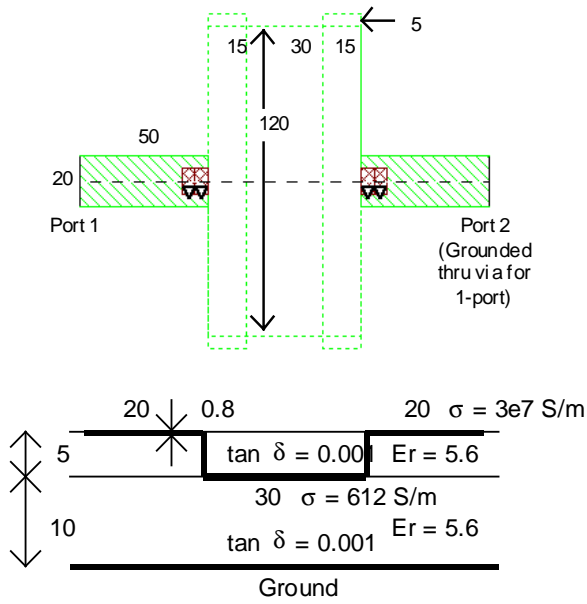


Figure 4.8: A resistor structure. All dimensional units are in mils.

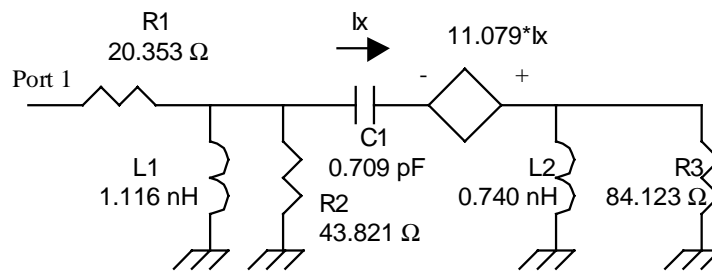


Figure 4.9: Equivalent circuit of the 1-port resistor in Figure 4.8.

4.4 Synthesis of Two-port Networks

Equivalent circuits for 2-port integral passive structure are obtained by synthesizing rational functions approximating z or y -parameter of the structure. For two-port structures, although lossy functions may be synthesized, the resulting circuit contains many negative elements, which creates difficulty interpreting its physical correlation to the structures. For this reason, most attention is paid to the lossless circuits. Chapter 3 discusses the details on generating the required functions.

The following steps outline the synthesis procedure for two port networks.

1. Observe the frequencies at which z_{21} (or y_{21}) becomes zero. From z_{11} (or y_{11}), remove the poles at the frequencies where z_{21} (or y_{21}) becomes zero. The poles at different frequencies can be subtracted in any order.
2. Correctly scale z_{21} (or y_{21}).
3. Compute the difference between z_{22} and partial z_{22} and synthesize it as for a 1-port structure. Add it to the circuit to complete the synthesis.
4. For every inductor and capacitor, divide by the frequency scaling factor that was used when generating the rational functions.

Four test cases have been considered to illustrate the synthesis procedure for lossless functions. As the first test case, let the z -parameters of the structure be defined by

$$z_{11} = \frac{a_0 + a_2 \cdot s^2}{d_1 \cdot s + d_3 \cdot s^3} \quad z_{21} = z_{12} = \frac{b_0}{d_1 \cdot s + d_3 \cdot s^3} \quad z_{22} = \frac{c_0 + c_2 \cdot s^2}{d_1 \cdot s + d_3 \cdot s^3}, \quad (4.10)$$

where all the coefficients are real and positive. The goal is to reduce the number of coefficients in z_{11} by subtracting functions that can be realized by lumped components. Zeros of z_{21} provide information on the components to be subtracted from z_{11} . The parameter z_{21} has three zeros at $s = \infty$. Poles at $s = \infty$ are therefore removed from z_{11} three times. The resulting circuit has three components consisting of inductors ($x \cdot s$ ohms) and capacitors ($x \cdot s$ mhos). Since z_{11} does not have a pole at $s = \infty$ but $1/z_{11}$ does, it is inverted for subtraction. Let y_2 be the remainder after subtraction,

$$y_2 = \frac{1}{z_{11}} - \frac{d_3}{a_2} \cdot s = \frac{e_1 \cdot s}{a_0 + a_2 \cdot s^2}, \quad (4.11)$$

where

$$e_1 = d_1 - \frac{1}{a_2} \cdot d_3 \cdot a_0. \quad (4.12)$$

A capacitor of d_3/a_2 F is subtracted in (4.11). The following subtraction,

$$z_{11} = \frac{a_0}{d_1 \cdot s}, \quad (4.13)$$

is also possible but is incorrect since it realizes a zero for z_{21} at $s = 0$. The remaining components are synthesized when the remainder y_2 is inverted to z_2 as shown below,

$$z_2 = \frac{1}{y_2} = \frac{a_0}{e_1 \cdot s} + \frac{a_2}{e_1} \cdot s. \quad (4.14)$$

Equation (4.14) consists of an inductor (a_2/e_1) H and a capacitor (e_1/a_0) F. The inductor and the capacitor are placed as shown in Figure 4.10 to provide three poles at $s = \infty$.

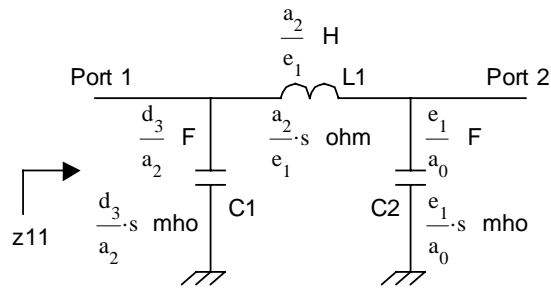


Figure 4.10: Equivalent circuit that matches z_{11} and zeros z_{21} in (4.10) before the z_{21} scaling.

Realizing an equivalent circuit by continued pole removal at $s = \infty$, as demonstrated in this case, is based on Cauer 1 realization [15][32][33][34]. Similarly, successive pole removal at $s = 0$ is also possible through Cauer 2 realization [15][32][33][34]. The circuit

shown in Figure 4.10 realizes z_{11} and zeros of z_{21} , but does not include the scaling factor, k , that must be applied to correctly scale z_{21} . In Figure 4.10,

$$z_{p21} = k \cdot z_{21}, \quad (4.15)$$

where

$$k = \frac{\left(\frac{d_1}{C1 + C2} \right)}{b_0}, \quad (4.16)$$

and z_{p21} is z_{21} of the circuit in Figure 4.10. One way to correctly scale for z_{21} is by adding a transformer in parallel with $C2$. However, this creates difficulty correlating the circuit to the physical structure. Another method has therefore been used in this dissertation by splitting $C2$ as shown in Figure 4.11. The capacitors, $C2a$ and $C2b$ are adjusted to correctly scale z_{21} while maintaining the following relationship,

$$C2a \parallel C2b = C2. \quad (4.17)$$

The final step is to obtain z_{22} - z_{p22} that matches z_{22} . Figure 4.12 defines z_{p22} . Suppose that

$$z_{22} - z_{p22} = \frac{f_0 + f_2 \cdot s^2}{d_1 \cdot s + d_3 \cdot s^3} \quad (4.18)$$

The function (4.18) is synthesized in the same way for 1-port and added as shown in Figure 4.11 to form a final circuit.

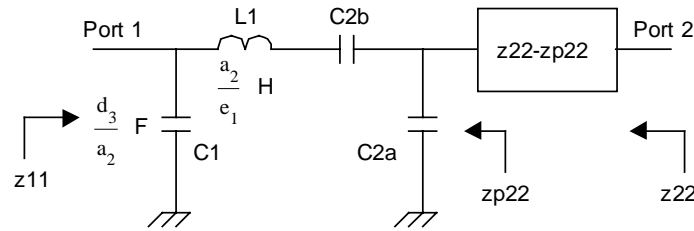


Figure 4.11: Equivalent circuit with z_{11} , z_{21} and z_{22} matched for (4.10).

The second test case considered has the same z_{11} and z_{22} as in (4.10) but a different z_{21} as shown,

$$z_{11} = \frac{a_0 + a_2 \cdot s^2}{d_1 \cdot s + d_3 \cdot s^3} \quad z_{21} = z_{12} = \frac{b_0 + b_2 \cdot s^2}{d_1 \cdot s + d_3 \cdot s^3} \quad z_{22} = \frac{c_0 + c_2 \cdot s^2}{d_1 \cdot s + d_3 \cdot s^3} \quad (4.19)$$

Zeros of z_{21} are located at $s = \pm j \cdot \sqrt{b_0/b_2}$ and $s = \infty$ which requires $\frac{x \cdot s}{b_0 + b_2 \cdot s^2}$ and $x \cdot s$

to be subtracted from z_{11} , where x is a real constant. To realize the subtraction of

$\frac{x \cdot s}{b_0 + b_2 \cdot s^2}$, poles of z_{11} are shifted to $s = \pm j \cdot \sqrt{b_0/b_2}$ by a partial pole removal [15] as

follows:

$$y_2 = \frac{1}{z_{11}} - x_1 s = \frac{sc_1 \cdot (b_0 + b_2 \cdot s^2) \cdot s}{a_0 + a_2 \cdot s^2}, \quad (4.20)$$

where x_1 is a constant which creates a pair of poles at $s = \pm j \cdot \sqrt{b_0/b_2}$ in the remainder z_2 , and sc_1 is a resulting scaling factor. The following subtraction is performed next,

$$z_3 = \frac{1}{y_2} - \frac{x_2 s}{b_0 + b_2 \cdot s^2} = \frac{sc_2 \cdot (b_0 + b_2 \cdot s^2)}{sc_1 \cdot (b_0 + b_2 \cdot s^2) \cdot s} = \frac{sc_2}{sc_1 \cdot s}, \quad (4.21)$$

where x_2 is a real constant that creates a pair of zeros at $s = \pm j \cdot \sqrt{b_0/b_2}$ in z_3 (to cancel out the same poles) and sc_2 is a resulting scaling factor. The synthesized circuit for this case is shown in Figure 4.12. To complete the synthesis, z_{21} is scaled and the difference of z_{22} and z_{p22} is added as discussed in the previous case.

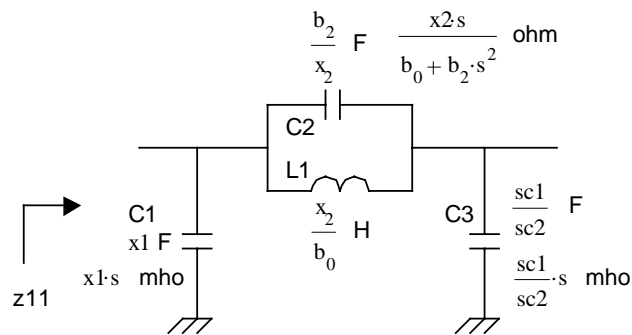


Figure 4.12: The equivalent circuit of (4.19) before z_{21} scaling and z_{22} matching.

The third test case considered has the following z_{21} (or z_{12}),

$$z_{11} = \frac{a_0 + a_2 \cdot s^2}{d_1 \cdot s + d_3 \cdot s^3} \quad z_{21} = z_{12} = \frac{b_0 + b_2 \cdot s^2 + b_4 \cdot s^4}{d_1 \cdot s + d_3 \cdot s^3} \quad z_{22} = \frac{c_0 + c_2 \cdot s^2}{d_1 \cdot s + d_3 \cdot s^3}, \quad (4.22)$$

with the same z_{11} and z_{22} in (4.10). It is impossible to synthesize an equivalent circuit since z_{21} has a private pole at $s = \infty$ that z_{11} does not have. However, the converse is not true as shown in the next case. (The function z_{11} may have a private pole that z_{21} does not have.)

Consider a fourth case with the following y -parameter functions,

$$y_{11} = \frac{a_1 \cdot s + a_3 \cdot s^3}{d_0 + d_2 \cdot s^2} \quad y_{21} = y_{12} = \frac{b_1 \cdot s}{d_0 + d_2 \cdot s^2} \quad y_{22} = \frac{c_1 \cdot s + c_3 \cdot s^3}{d_0 + d_2 \cdot s^2}. \quad (4.23)$$

There are three zeros of y_{21} , one located at $s = 0$, two at $s = \infty$. It implies that $1/(x \cdot s)$ need be subtracted once and $x \cdot s$ twice from y_{11} , where x is a real constant. The subtraction may be done in any order. If a pole at $s = 0$ is removed first, the following subtraction is performed with its remainder z_2 ,

$$z_2 = \frac{1}{y_{11}} - \frac{d_0}{a_1 \cdot s} = \frac{e_1 \cdot s}{a_1 + a_3 \cdot s^2}, \quad (4.24)$$

where

$$e_1 = \frac{(a_1 \cdot d_2 - d_0 \cdot a_3)}{a_1} \quad (4.25)$$

A capacitor with a_1/d_0 F is extracted. The remaining elements are easily seen from y_2 (or $1/z_2$) without further subtraction. The resulting circuit is shown in Figure 4.13. C1 realizes a pole at $s=0$, C2 and L1 realize two poles at $s = \infty$. To finish the synthesis, y_{21} needs to be scaled by splitting L1 and the difference of y_{22} and y_{p22} must be added as illustrated in Figure 4.11.

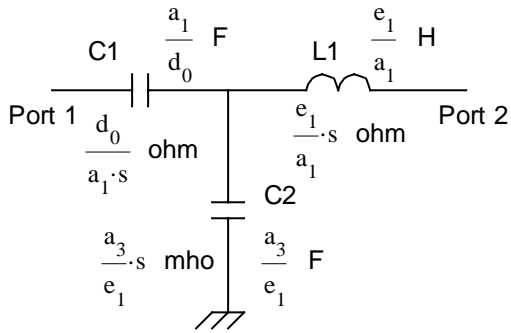


Figure 4.13: The equivalent circuit of (4.23) before y_{21} scaling and y_{22} matching.

To illustrate the synthesis of lossy circuits, the following lossy y -parameter functions are considered:

$$y_{11} = \frac{a_0 + a_1 \cdot s}{d_1 \cdot s + d_2 \cdot s^2} \quad y_{21} = y_{12} = \frac{b_0 + b_1 \cdot s}{d_1 \cdot s + d_2 \cdot s^2} \quad y_{22} = \frac{c_0 + c_1 \cdot s}{d_1 \cdot s + d_2 \cdot s^2} \quad (4.26)$$

There are two zeros of y_{21} , one located at $s = -b_0/b_1$ and the other at $s = \infty$, which requires that $x/(b_1 \cdot s + b_0)$ and $x \cdot s$ are subtracted from y_{11} , where x is a real constant. To shift the pole of y_{11} to $s = -b_0/b_1$, a pole is partially removed,

$$z_2 = \frac{1}{y_{11}} - x_1 \cdot s = \frac{sc_1 \cdot (b_0 + b_1 \cdot s) \cdot s}{a_0 + a_1 \cdot s}, \quad (4.27)$$

where x_1 is a real constant that creates a pole at $s = -b_0/b_1$ in y_2 . The following subtraction is performed next,

$$y_3 = \frac{1}{z_2} - \frac{x_2}{b_0 + b_1 \cdot s} = \frac{sc_2 \cdot (b_0 + b_1 \cdot s)}{sc_1 \cdot (b_0 + b_1 \cdot s) \cdot s} = \frac{sc_2}{sc_1 \cdot s}, \quad (4.28)$$

where x_2 is a real constant that creates a zero at $s = -b_0/b_1$ in y_3 (to cancel the same pole in the denominator). Figure 4.14 shows the resulting equivalent circuit. To complete the synthesis, y_{21} is scaled and the difference of y_{22} and y_{p22} is added as discussed previously.

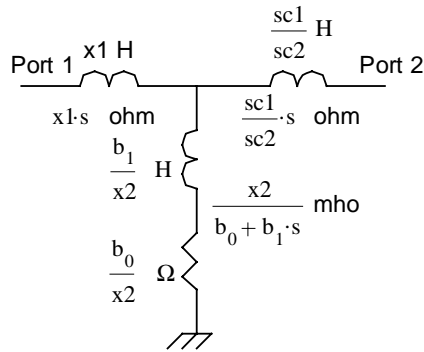


Figure 4.14: Equivalent circuit of (4.26) before y_{21} scaling and y_{22} matching.

4.5 Examples of Equivalent Circuits for Two-port Structures

The synthesis technique was applied to a 2-port inductor, capacitor and resistor with dimension similar to the 1-port case. Lossless functions were generated for every case using the data obtained from SONNET [25]. The equivalent circuits were synthesized from the resulting functions. The response of all the equivalent circuits is accurate over the frequency band DC – 4 GHz unless stated otherwise.

4.5.1 Inductor

Figure 4.15 shows the 2-port inductor structure and Figure 4.16 shows the equivalent circuit. The low frequency inductance of 10 nH is shown by L1 while C1 and C2 represent the parasitic capacitance between the metal and the ground. The inductance of the stripline leading to port 2 is captured by L2.

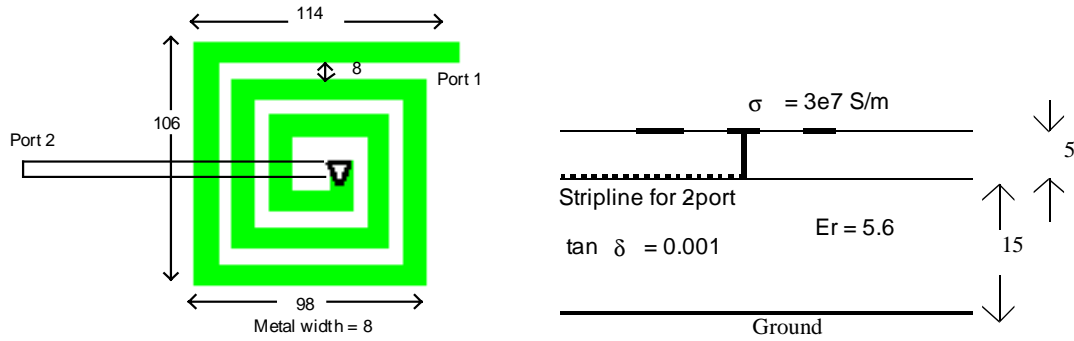


Figure 4.15: An embedded inductor structure. All dimensional units are in mils.

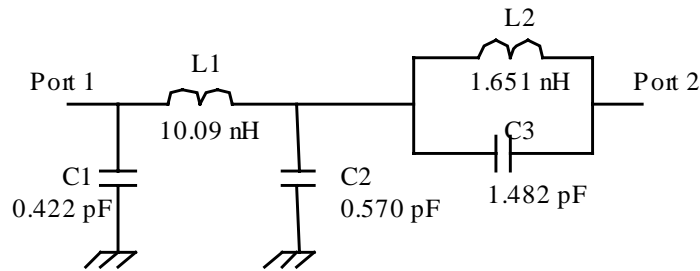


Figure 4.16: Equivalent circuit of the 2-port inductor in Figure 4.15.

4.5.2 Capacitor

Figure 4.17 shows the equivalent circuit of the 2-port capacitor in Figure 4.5. The s-parameters of the equivalent circuit have been compared to the simulated data from SONNET, as shown in Figure 4.18. The results show good agreement. For the capacitor structure in Figure 4.5, the capacitance between the plates can be computed using the simple parallel plate capacitor formula as

$$C = \frac{\epsilon_r \cdot \epsilon_o \cdot \text{width} \cdot \text{length}}{\text{distance}} = \frac{5.6 \left(0.225 \frac{\text{fF}}{\text{mil}} \right) \cdot (66 \cdot \text{mil}) \cdot (66 \cdot \text{mil})}{1 \cdot \text{mil}} = 19.6 \text{ pF} \quad (4.29)$$

This value agrees well with capacitor C2 in Figure 4.17. Based on the physical dimensions and the electrical properties of the substrate, the interconnect leading to the capacitor has $Z_0 = 54.2 \Omega$ and $\theta = 7.045^\circ$ which translates to an inductance at 2 GHz with value:

$$L = \frac{Z_0 \cdot \sin(\theta)}{\omega} = \frac{54.2 \text{ ohm} \cdot \sin(7.045)}{2 \cdot \pi \cdot 2 \cdot \text{GHz}} = 0.53 \text{ nH} \quad (4.30)$$

(assuming that the capacitive effect between the interconnect and the ground is small).

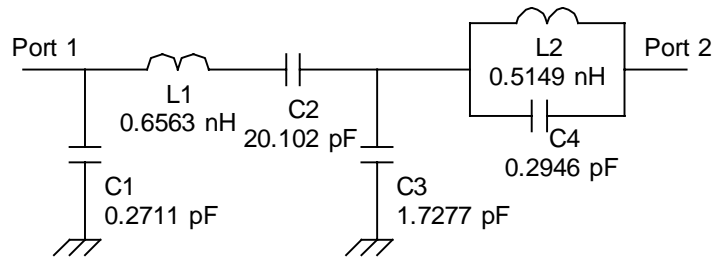


Figure 4.17: Equivalent circuit of the 2-port capacitor structure in Figure 4.5.

S11

S21

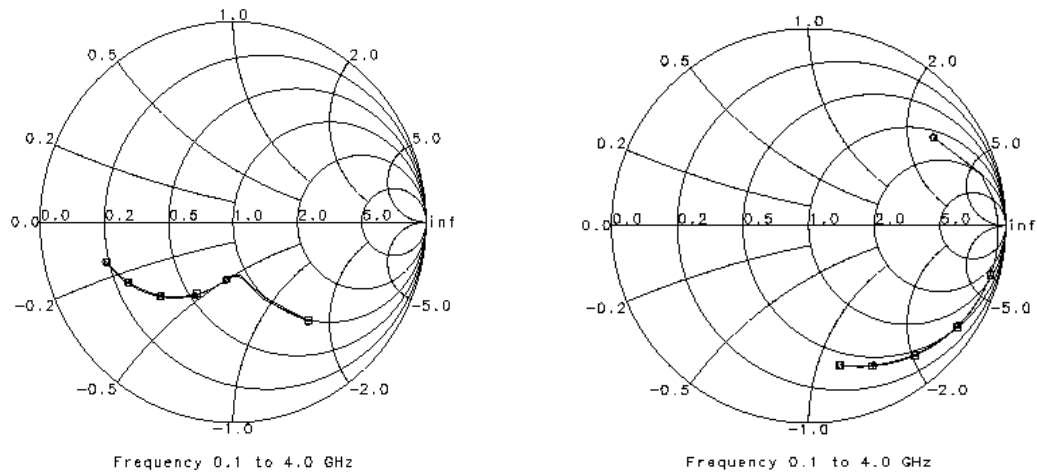


Figure 4.18: Response of SONNET (square) and the lossless equivalent circuit (circle) of the 2-port capacitor structure in Figure 4.5.

The inductors L1 and L2 capture the inductive effect of the interconnect. The inductor L1 is believed to be slightly higher than (4.30) due to the presence of C1. Using (4.29), the capacitance between the bottom plate and the ground plane is 1.28 pF, which is close to capacitor C3 in Figure 4.17. The inductors L1 and L2 capture the inductive effect of the interconnect. The inductor L1 is believed to be slightly higher than (4.30) due to the presence of C1. Using (4.29), the capacitance between the bottom plate and the ground plane is 1.28 pF, which is close to capacitor C3 in Figure 4.17.

The lossy equivalent circuit is shown in Figure 4.19. The circuit models the loss and is accurate up to 2.5 GHz. However, the presence of many negative components creates much difficulty correlating the lumped elements to the physical structure.

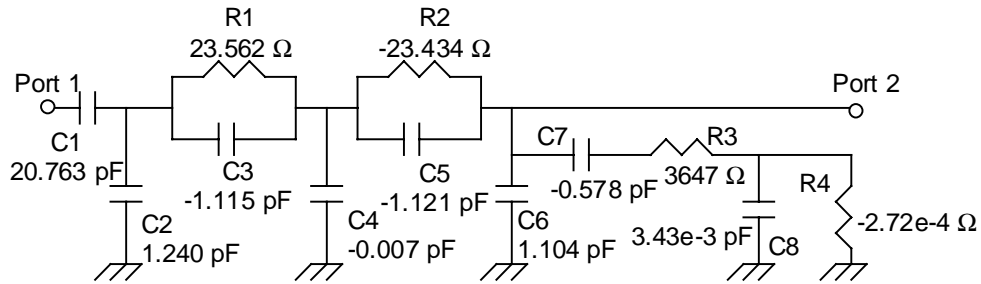


Figure 4.19: Lossy equivalent circuit of the capacitor structure in Figure 4.8.

4.5.3 Resistor

For the 2-port embedded resistor in Figure 4.8, only reactive elements (inductors and a capacitor) were first synthesized from the lossless functions. The resistors were then incorporated into the equivalent circuit and their values were optimized using a gradient optimizer in Microwave Design System (MDS). The value of the reactive elements were kept fixed. The optimization generated a negative resistor which was replaced with a current controlled voltage source. The final equivalent circuit is shown in Figure 4.20. Figure 4.21 compares the s-parameters of the equivalent circuit with only reactive elements before optimization and the data from SONNET. As can be seen, the results have large error. Figure 4.22 compares the s-parameters of the final circuit after the optimization with data from SONNET. In Figure 4.22, the agreement is almost exact. The benefit of using the optimizer after synthesizing the lossless equivalent circuit is that the degree of freedom for the optimizer can be minimized. For the resistor structure in Figure 4.8, the DC resistance can be computed as

$$R_{dc} = \frac{1}{\sigma \cdot (\text{metal_thickness})} = \frac{1}{\left(611.9 \frac{\text{S}}{\text{m}}\right) \cdot (20.32 \mu\text{m})} = 80.4 \frac{\text{ohm}}{\text{square}} \quad (4.31)$$

The dimension of 120 mil * 30 mil of the lossy metal can be regarded as four 80.4 Ω connected in parallel which gives a resistance of 20.1 Ω . Sum of R1 and R2 in Figure 4.19 gives the equivalent DC resistance. Using equation (4.30), the inductive effect of the interconnect at 2 GHz is computed as 0.57 nH, which compares well with inductors L1 and L2. Using equation (4.29), the parasitic capacitance between the lossy metal and ground plane is computed as 0.91 pF, which is represented by capacitor C1. The value of C1 is believed to be much higher than the theoretical prediction due to the presence of the controlled voltage source.

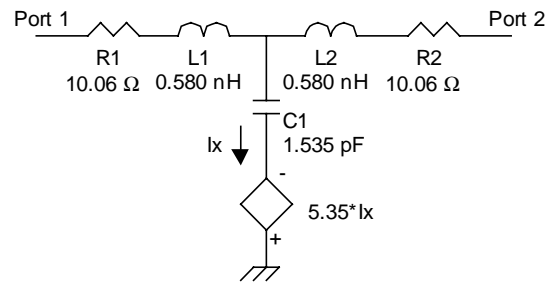


Figure 4.20: Equivalent circuit of the resistor structure in Figure 4.8. Losses (resistors) were optimized by an optimizer in MDS.

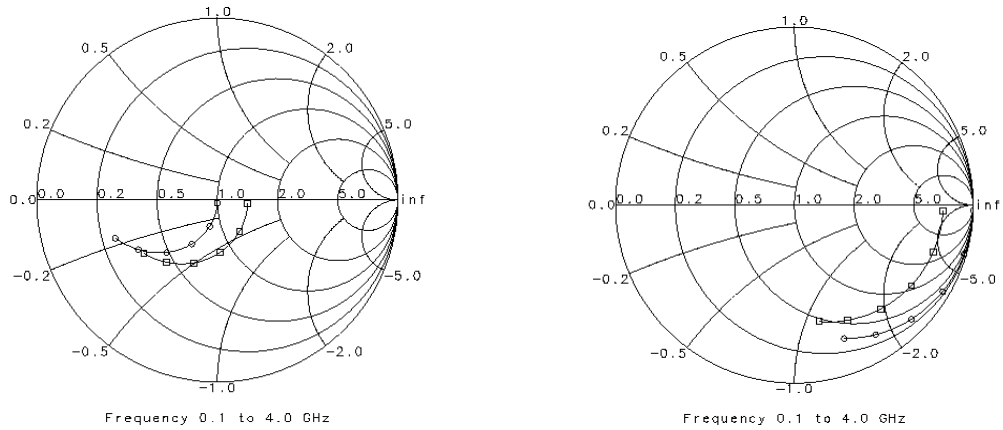


Figure 4.21: Response of SONNET (square) and the equivalent lossless circuit (circle) of the 2-port resistor in Figure 4.8 before optimization.

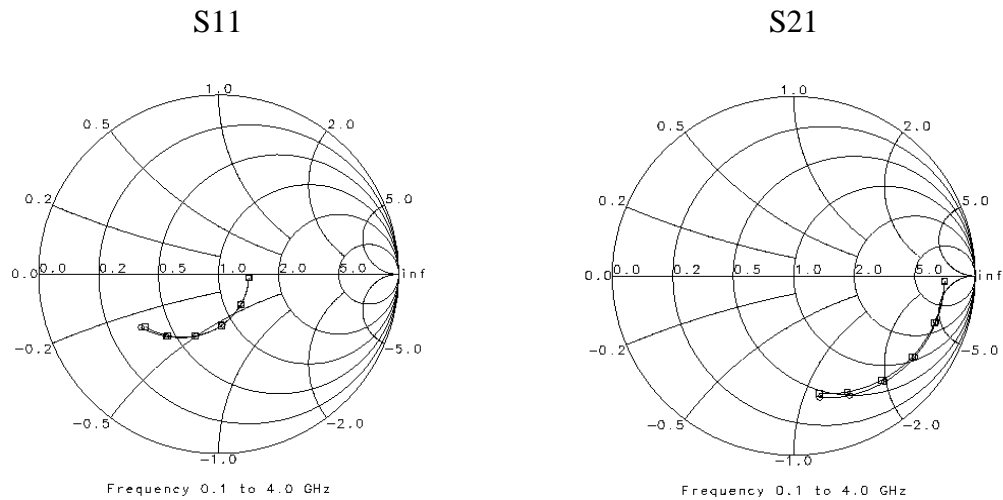


Figure 4.22: Response of SONNET (square) and the lossy equivalent circuit (circle) of the 2-port resistor in Figure 4.8 after optimization.

Figure 4.23 shows the lossy equivalent circuit. The interpretation to the physical structure is very difficult due to the presence of the negative elements. It also requires

almost twice as many lumped elements to realize the losses. For these reasons, synthesis of lossless circuits are preferred.

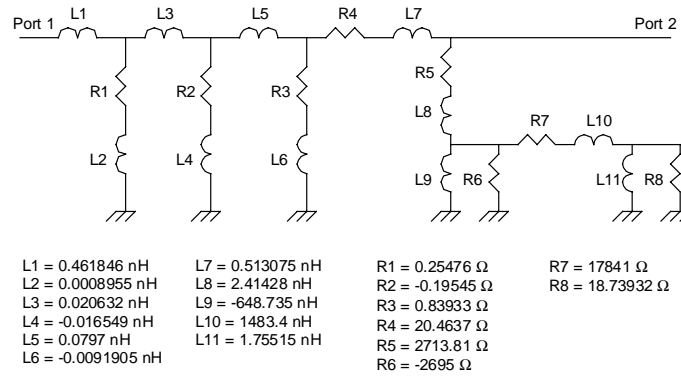


Figure 4.23: Lossy equivalent circuit of the resistor structure in Figure 4.8.

4.6 More Examples of Equivalent Circuits for Thin-film Structures

Circuit synthesis was applied to thin-film embedded structures realized by SLIM technology. An equivalent circuit was synthesized for a one-port inductor structure and a two-port capacitor structure. Figure 4.24 shows the one-port inductor structure. Figure 4.25 shows the resulting equivalent circuit.

The two-port capacitor structure is shown in Figure 4.26. Figure 4.27 shows its equivalent circuit.

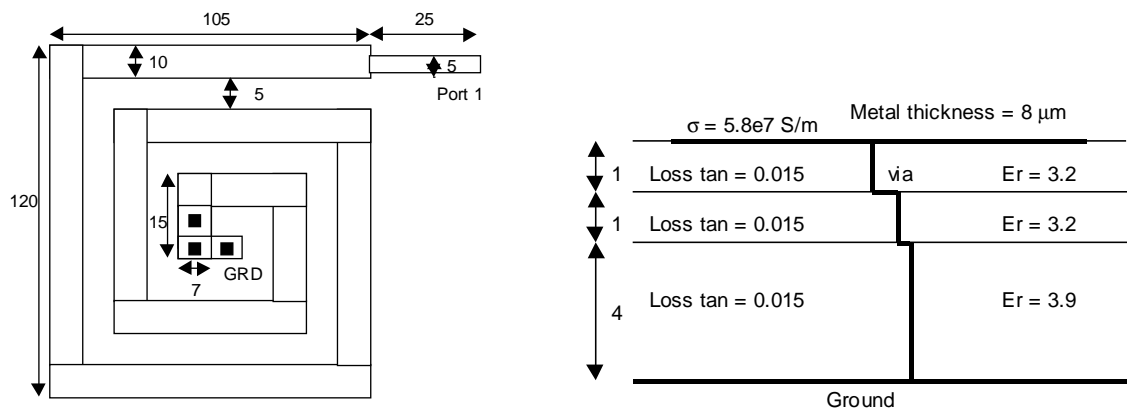


Figure 4.24: SLIM one-port inductor structure.

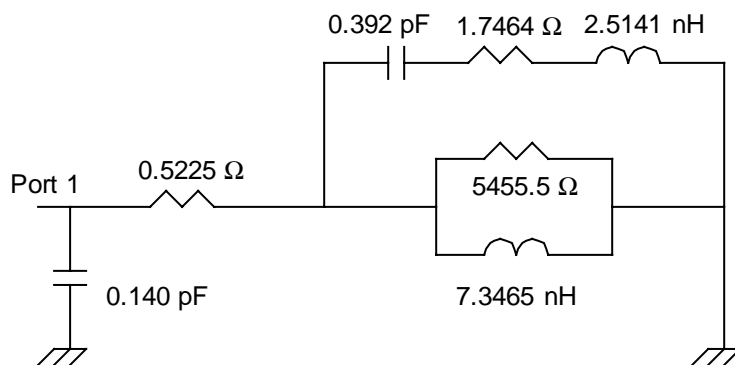


Figure 4.25: Equivalent circuit for the SLIM inductor structure shown in Figure 4.24.

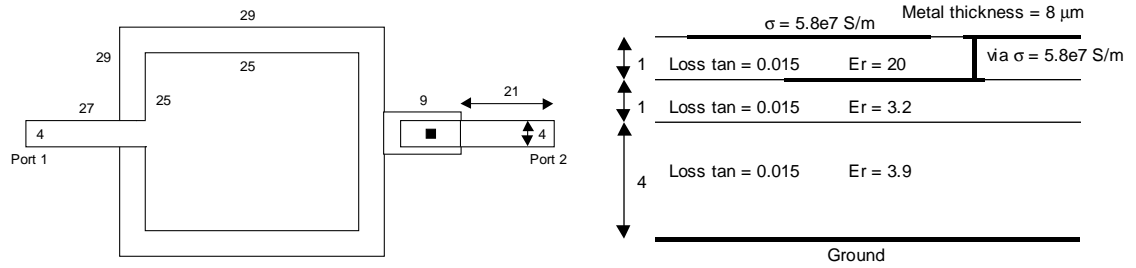


Figure 4.26: SLIM two-port capacitor structure.

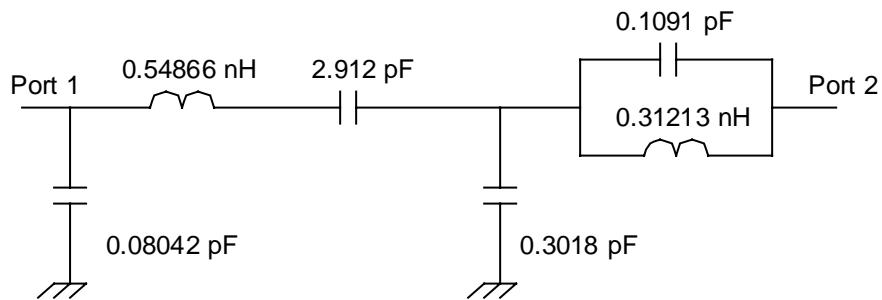


Figure 4.27: The equivalent circuit for the capacitor structure.

CHAPTER 5

STABILITY ENFORCEMENT ALGORITHM

For all the embedded passive structures presented in the previous chapters, the interpolation generated a stable solution using a minimum order. However, the interpolation technique may not always generate stable solutions, especially when a high order approximation is performed. The interpolation may produce rational functions that have poles on the right half plane. In such case, the solution results in unbounded time domain response and is no longer suitable for macromodeling.

In this chapter, a stability enforcement algorithm is presented. The method provides a stable solution even when unstable solution is generated by discarding unstable poles and collecting only stable poles for reinterpolation. The response is reinterpolated using sampled data and updating the residue of each collected stable pole. Only real coefficient rational function is considered since complex coefficient rational function is not suitable for macromodeling and circuit synthesis.

5.1 Stability Algorithm

Stability enforcement algorithm is applied to rational functions that contain one or more unstable poles. Rational functions are generated by the interpolation technique, which does not guarantee a stable solution. To illustrate the mathematical details of the algorithm, consider the following stable poles after discarding unstable poles of a real coefficient rational function,

$$p_0, p_1, p_2. \quad (6.1)$$

For real coefficient rational functions, poles are either a pair of complex conjugates or real. In addition, a pair of complex poles has a pair of corresponding complex residues and a real pole has a corresponding real residue. Suppose that p_0 and p_1 are complex conjugates of each other and p_2 is real. The response to be reinterpolated can be represented as

$$H(s) = \frac{r_0}{s - p_0} + \frac{r_1}{s - p_1} + \frac{r_2}{s - p_2}. \quad (6.2)$$

Since p_0 and p_1 are complex conjugates, r_0 and r_1 are also complex conjugates. The residue r_2 is real since the corresponding pole p_2 is real. The equation $H(s)$ is written as

$$H(s) = \frac{r_{\text{real}_0} + j \cdot r_{\text{imag}_0}}{s - p_0} + \frac{r_{\text{real}_0} - j \cdot r_{\text{imag}_0}}{s - p_0^*} + \frac{r_2}{s - p_2} \quad (6.3)$$

The equation can be represented as a matrix format,

$$[A] \cdot \begin{bmatrix} r_{\text{real}_0} \\ r_{\text{imag}_0} \\ r_2 \end{bmatrix} = \begin{bmatrix} H(s_1) \\ H(s_2) \\ \vdots \end{bmatrix}, \quad (6.4)$$

where

$$[A] = \begin{bmatrix} \text{Real} \\ \text{Imag} \end{bmatrix} = \begin{bmatrix} \frac{1+j}{s_1-p_0} & \frac{1-j}{s_1-p_0^*} & \frac{1}{s_1-p_2} \\ \frac{1+j}{s_2-p_0} & \frac{1-j}{s_2-p_0^*} & \frac{1}{s_2-p_2} \\ \vdots & \vdots & \vdots \\ \frac{1+j}{s_1-p_0} & \frac{1-j}{s_1-p_0^*} & \frac{1}{s_1-p_2} \\ \frac{1+j}{s_2-p_0} & \frac{1-j}{s_2-p_0^*} & \frac{1}{s_2-p_2} \\ \vdots & \vdots & \vdots \end{bmatrix}. \quad (6.5)$$

The residues are found by solving

$$\begin{bmatrix} r_{\text{real}_0} \\ r_{\text{imag}_0} \\ r_2 \end{bmatrix} = [A^T \cdot A]^{-1} \cdot A^T \cdot \begin{bmatrix} H(s_1) \\ H(s_2) \\ \vdots \end{bmatrix}, \quad (6.6)$$

where T denotes transposed matrix.

5.2 Results of Stability Enforcement Algorithm

The stability enforcement algorithm was applied to three embedded structures, an inductor, a capacitor, and a resistor. The result of each structure is discussed in the following subsections.

5.2.1 Inductor

The algorithm was applied to a one-port inductor structure shown in Figure 5.1. The full set of SONNET-generated data were used for interpolation. When numerator order P and the denominator order Q were set to 5 and 6 respectively, the following poles were generated,

$$\begin{aligned} p_1 &= -0.09381710220291 + 3.93552177549540i \\ p_2 &= -0.09381710220291 - 3.93552177549540i \\ p_3 &= 3.40351561030503 \\ p_4 &= -1.69842759178416 \\ p_5 &= -0.00967791873625 + 1.17094594502752i \\ p_6 &= -0.00967791873625 - 1.17094594502752i. \end{aligned}$$

The unstable pole p_3 was discarded and the remaining poles were collected to find their corresponding residues using a minimum number of data. Since there are five stable poles, the required minimum number of data for reinterpolation is five. The following residues were found,

$$\begin{aligned}
 r_1 &= 88.12530887269060 + 2.87116953815470i \\
 r_2 &= 88.12530887269060 - 2.87116953815470i \\
 r_4 &= -0.43878404204200 \\
 r_5 &= 56.29736595043329 - 0.07116581469280i \\
 r_6 &= 56.29736595043329 + 0.07116581469280i.
 \end{aligned}$$

Figure 5.2 shows the reinterpolated response using the stable poles and the updated residues. It shows a good agreement to the full set of SONNET-generated data.

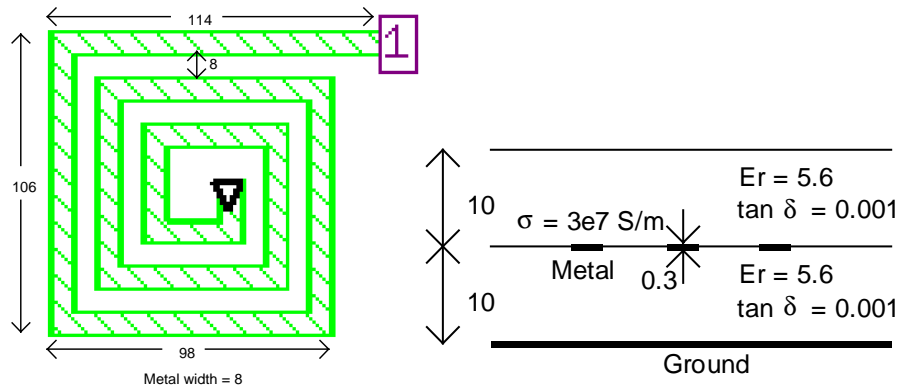


Figure 5.1: The inductor structure. All dimensional units are in mils.

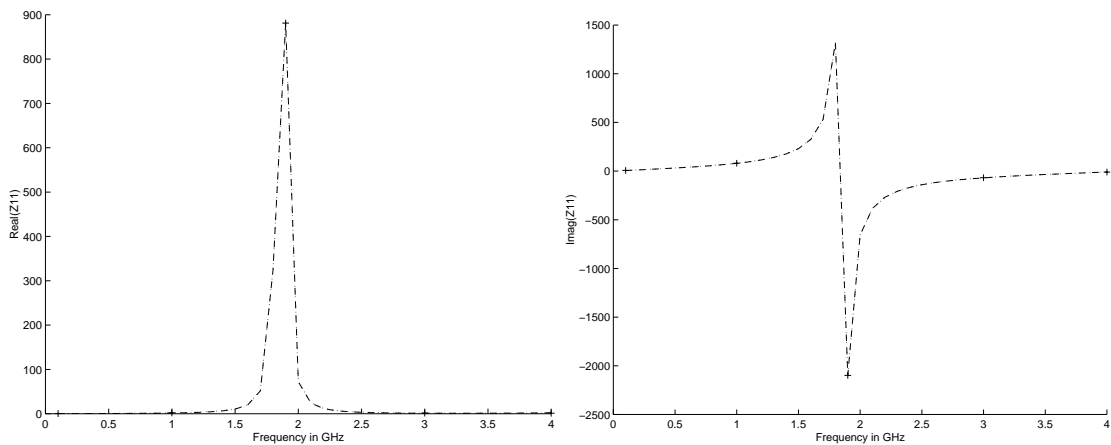


Figure 5.2: Response of SONNET and the stable function.

Dotted - SONNET, dashed - the stable function, x - data points used to update residues.

5.2.2 Capacitor

The stability enforcement algorithm was applied to a two-port capacitor structure shown in Figure 5.3. The order of the numerator for z_{11} , z_{21} , and z_{22} were chosen $P_1=7$, $P_2=5$, and $P_3=7$ respectively, and order of the common denominator was chosen as $Q=8$. When the interpolation technique was initially applied, the following poles were generated:

$$\begin{aligned}p_1 &= -0.37091208503460 + 23.81636689459581i \\p_2 &= -0.37091208503460 - 23.81636689459581i \\p_3 &= -0.02064844803906 + 9.62709057291218i \\p_4 &= -0.02064844803906 - 9.62709057291218i \\p_5 &= -1.62530071748234 \\p_6 &= -0.20662268448497 \\p_7 &= -0.00005857433403 \\p_8 &= 0.46829284242248.\end{aligned}$$

The last pole p_8 , which was located on the right half plane, was discarded. Using the remaining seven poles, the response was reinterpolated. The required minimum number of data for updating residues is equal to the number of poles, which is seven. However, in this case, the full set of 40 data points was used for reinterpolation to illustrate that a large number of data may also be used for this algorithm. The following residues were found for z_{11} :

$$\begin{aligned}r_1 &= 1613.86734272516 + 24.77155348352i \\r_2 &= 1613.86734272516 - 24.77155348352i \\r_3 &= -0.01791131599163 - 0.00012800627490i \\r_4 &= -0.01791131599163 + 0.00012800627490i \\r_5 &= 0.00020514568968 \\r_6 &= 0.00002707541385 \\r_7 &= 0.05416097676304.\end{aligned}$$

The following residues were found for z_{21} :

$$\begin{aligned} r_1 &= 383.585280450992 + 16.5386711679748i \\ r_2 &= 383.585280450992 - 16.5386711679748i \\ r_3 &= -95.5253769119736 - 3.96743824592704i \\ r_4 &= -95.5253769119736 + 3.96743824592704i \\ r_5 &= 0.346840226388849 \\ r_6 &= 0.0127462727721763 \\ r_7 &= 49.5645011133654. \end{aligned}$$

The reinterpolated response of z_{11} and z_{21} are shown in Figure 5.4.

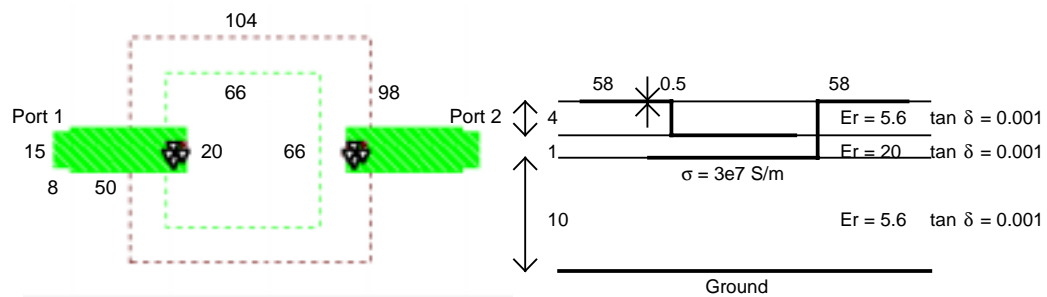


Figure 5.3: Capacitor structure. All dimensional units are in mils.

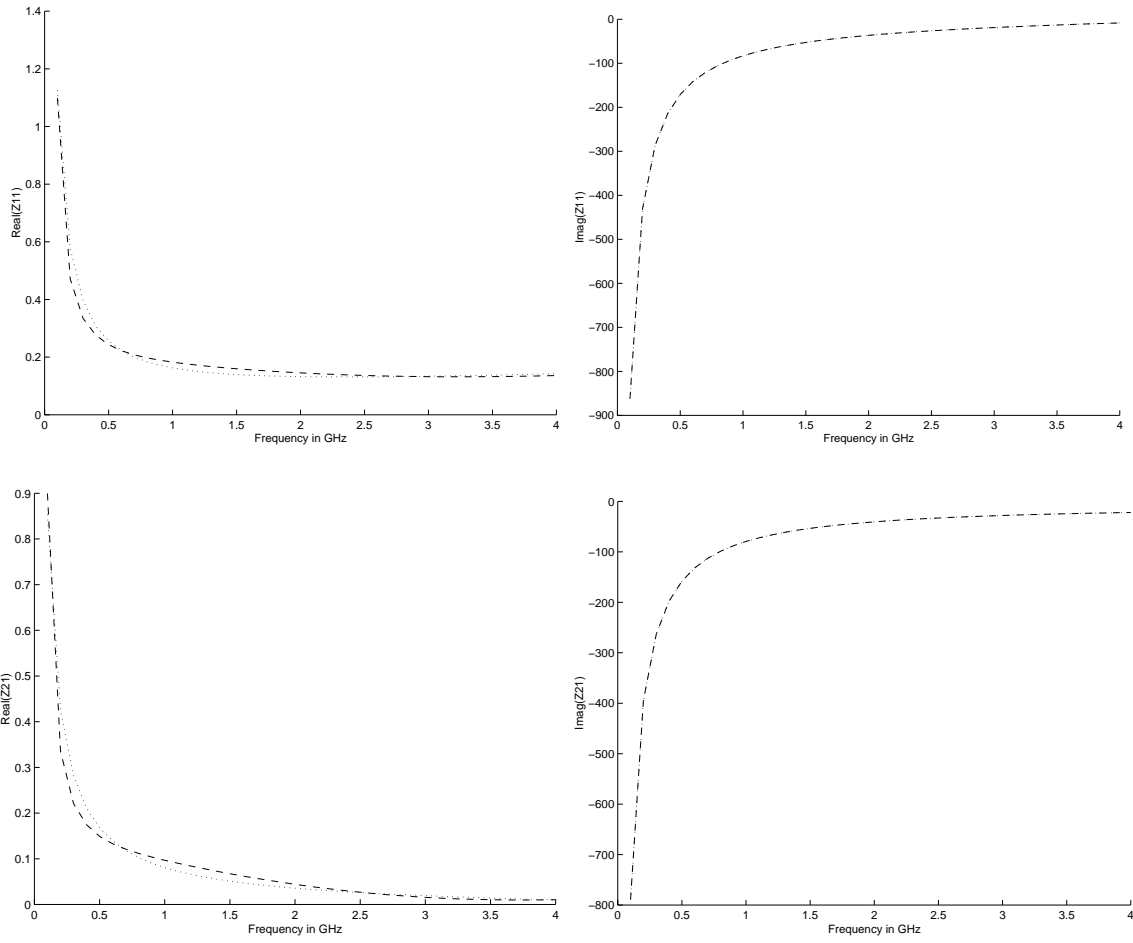


Figure 5.4: Response of SONNET and the stable function.
Dotted - SONNET, dashed - the stable function.

5.2.3. Resistor

The stability enforcement algorithm was applied to a resistor structure shown in Figure 5.5. The full set of SONNET data was used for interpolating input impedance. When the numerator order P and the denominator order Q were chosen as 7 and 8 respectively, the interpolation generated a rational function that has the following poles,

$$\begin{aligned}p_1 &= -2.32170458414923 + 19.51105596973696i \\p_2 &= -2.32170458414923 - 19.51105596973696i \\p_3 &= -0.47601779769009 + 3.07147365384140i \\p_4 &= -0.47601779769009 - 3.07147365384140i \\p_5 &= -1.49677896518829 \\p_6 &= -0.49260401989093 \\p_7 &= 0.33983141585170 \\p_8 &= -0.10460796701448.\end{aligned}$$

The unstable pole p_7 was discarded and the remaining stable poles were used for reinterpolation. The algorithm generated the following residues for each stable pole,

$$\begin{aligned}r_1 &= 1021.95606779936 + 85.6897526872064i \\r_2 &= 1021.95606779936 - 85.6897526872064i \\r_3 &= 34.327940282873 - 22.0940582818584i \\r_4 &= 34.327940282873 + 22.0940582818584i \\r_5 &= -0.619140941015019 \\r_6 &= -0.136069656620521 \\r_8 &= -0.0172113287677469.\end{aligned}$$

The stable function is shown in Figure 5.6. It shows a good agreement to the full set of SONNET data.

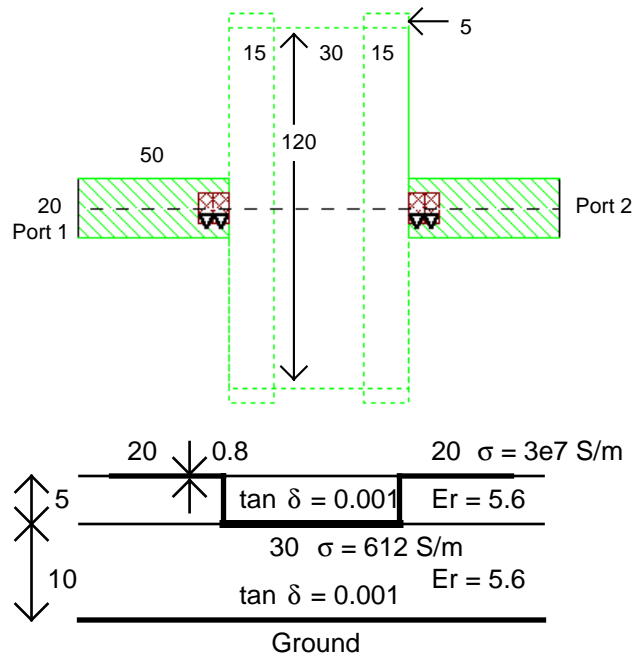


Figure 5.5: Top and side view of the 26Ω resistor structure. The dimensional units are in mils.

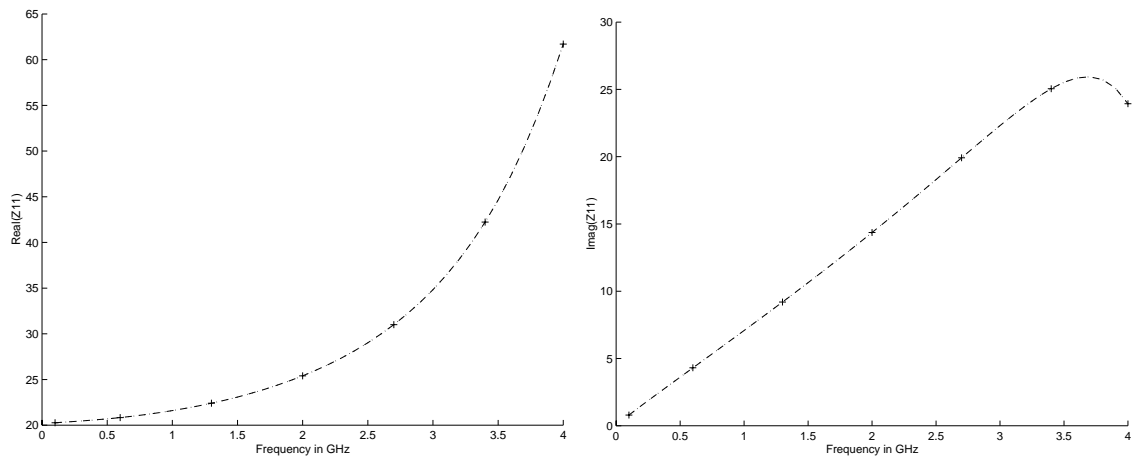


Figure 5.6: Input impedance generated by SONNET and the stable function. Dotted - SONNET, dashed - the stable function, x - data points used to update residues.

5.3 Application of the Stability Enforcement Algorithm

To illustrate usefulness of the method, the SPICE macromodeling technique and the equivalent circuit synthesis were applied to a stable function generated by the stability enforcement algorithm. The interpolation technique was applied to a resistor structure shown in Figure 5.7. The structure was realized based on SLIM ground rules. When the numerator order $P=4$ and the denominator order $Q=5$ were used, an unstable function with the following poles was generated:

$$\begin{aligned}p_1 &= -5.05659506715923 \\p_2 &= 4.39490145430350 \\p_3 &= -1.42631797166535 \\p_4 &= -0.43872785649784 \\p_5 &= -0.04859896130694\end{aligned}$$

The unstable pole p_2 was discarded and the residue of each stable pole was updated. The residues were found as

$$\begin{aligned}r_1 &= 1.91744977456039*100 \\r_3 &= 1.30724934118518*100 \\r_4 &= 1.95963418381059*100 \\r_5 &= 2.57234728406099*100.\end{aligned}$$

The stable function obtained using this algorithm is written as

$$Z_{in}(s) = \frac{r_1}{s + p_1} + \frac{r_3}{s + p_3} + \frac{r_4}{s + p_4} + \frac{r_5}{s + p_5}. \quad (6.7)$$

To incorporate this stable function in SPICE as a macromodel, the function (6.7) need be rewritten as a rational function,

$$Z_{in}(s) = \frac{a_0 + a_1 \cdot s + a_2 \cdot s^2 + a_3 \cdot s^3}{b_0 + b_1 \cdot s + b_2 \cdot s^2 + b_3 \cdot s^3 + b_4 \cdot s^4}$$

$$a = \begin{bmatrix} 1.128207185067 \\ 5.655339828542 \\ 5.190105543452 \\ 0.969585072952 \end{bmatrix}$$

$$b = \begin{bmatrix} 0.000192223616 \\ 0.004566225131 \\ 0.012991164399 \\ 0.008712799821 \\ 0.00125 \end{bmatrix} . \quad (6.8)$$

Not only can the stable function in (6.8) be used to build a macromodel, but also an equivalent circuit can be synthesized from (6.8). Figure 5.8 shows the equivalent circuit extracted from (6.8).

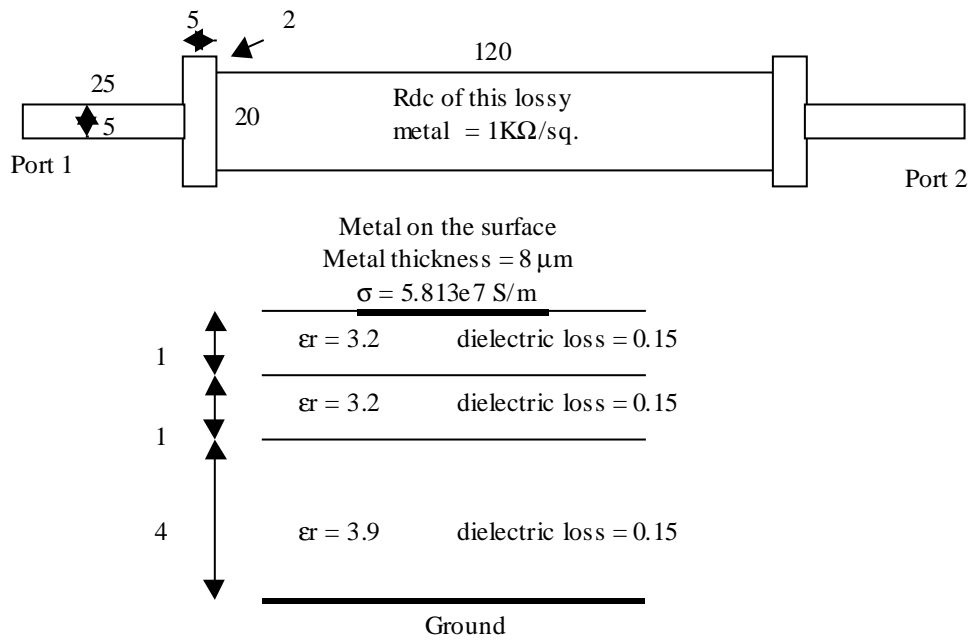


Figure 5.7: SLIM resistor structure. All dimensional units are in mils unless stated otherwise.

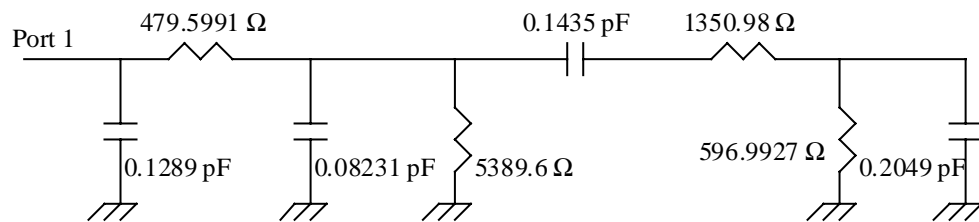


Figure 5.8: Equivalent circuit of the resistor structure in Figure 5.7.

CHAPTER 6

SIMULATION OF EMBEDDED CIRCUITS USING MACROMODELS AND EQUIVALENT CIRCUITS

In Chapter 2, a method was developed to capture the frequency response of an embedded component using rational functions. The method used an interpolation technique to reduce the analysis time using commercial electromagnetic (EM) solvers. In Chapter 3, the method was applied for transient simulation using SPICE macromodels. In Chapter 4, methods were presented for equivalent circuit synthesis from the rational functions to develop circuit models. The modeling techniques presented in the previous chapters were applied to only a single embedded passive component (or two at most for modeling of a voltage divider in Chapter 3). In this chapter, the macromodeling technique and the equivalent circuit synthesis are applied to circuits that consist of multiple embedded components. The accuracy of the two modeling techniques is compared.

Two cases are considered. The first case is embedded circuits used in digital applications. Multiple transmission lines were terminated with a matching embedded resistor and the time domain response was evaluated. The other case is an embedded circuit used in RF application and its frequency response was examined [45]. Low Temperature Cofired Ceramic technology (LTCC-M) process ground rules were used for the design of embedded components.

6.1 Digital Application

The circuit shown in Figure 6.1 was simulated in the time domain. The transmission lines have the characteristic impedance Z_0 of 150Ω and are terminated with an embedded resistor that has matching resistance of 150Ω . The structure of the embedded resistor, shown in Figure 6.2, is based on LTCC-M ground rules. A full set of data (0.1 - 4 GHz) was used to interpolate its frequency response and SONNET was used to obtain the data. The following rational function approximating the input admittance was generated:

$$Y_{in}(s) = \frac{a_0 + a_1 \cdot s + a_2 \cdot s^2}{b_0 + b_1 \cdot s + b_2 \cdot s^2 + b_3 \cdot s^3},$$

where

$$\begin{aligned}
 \mathbf{a} &= \begin{pmatrix} 0.00502568697585 \\ 0.02227981162008 \\ 0.00720672075652 \end{pmatrix} & \mathbf{b} &= \begin{bmatrix} 0.76829234150291 \\ 0.61994864936008 \\ 0.15310945503831 \\ 0.03707371795469 \end{bmatrix}
 \end{aligned} \tag{6.1}$$

The function in (6.1) was used to build a macromodel. An equivalent circuit was also extracted from (6.1) and is shown in Figure 6.3.

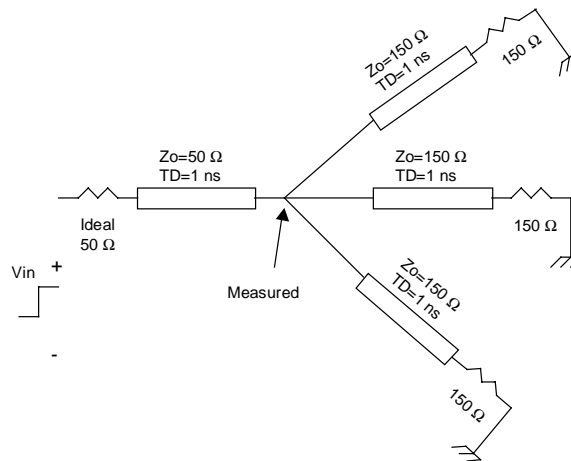


Figure 6.1: Schematic of the digital circuit for test.

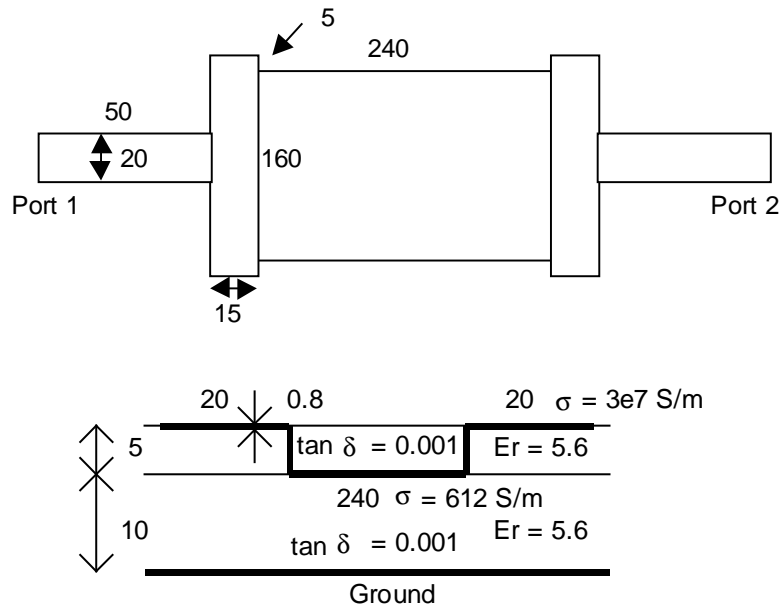


Figure 6.2: The 150 Ω resistor structure. All dimensional units are in mils.

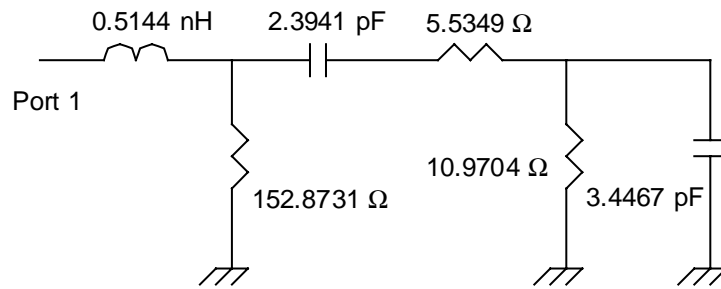


Figure 6.3: Equivalent circuit of the resistor structure shown in Figure 6.2.

To test the effect of terminating resistors using the two modeling methods, the circuit shown in Figure 6.1 was simulated twice in SPICE, first using macromodel for the resistor, and second using the equivalent circuit model for the resistor. The circuit was also simulated using ideal lumped resistor for comparison. For all the cases, the circuit

was excited by a 1-volt step input with 35 ps rise time. Figure 6.4 shows the response of each case. In the plot, the parasitic effect is shown after 2 ns from the ideal response, 1 ns to travel through the transmission line and 1 ns to bounce back through the same transmission line from the embedded resistor.

The circuit shown in Figure 6.5 was also simulated in the same manner. Figure 6.6 shows the response of each modeling case.

For both cases, the results show that the response of macromodel and the response of equivalent circuit are in good agreement. Both modeling techniques consistently generate the same results and, therefore, designers may choose either one of the modeling methods.

Figure 6.4: Response of each modeling method for the circuit shown in Figure 6.1.
Dashed - macromodel, dotted - equivalent circuit, solid - ideal lumped resistor.

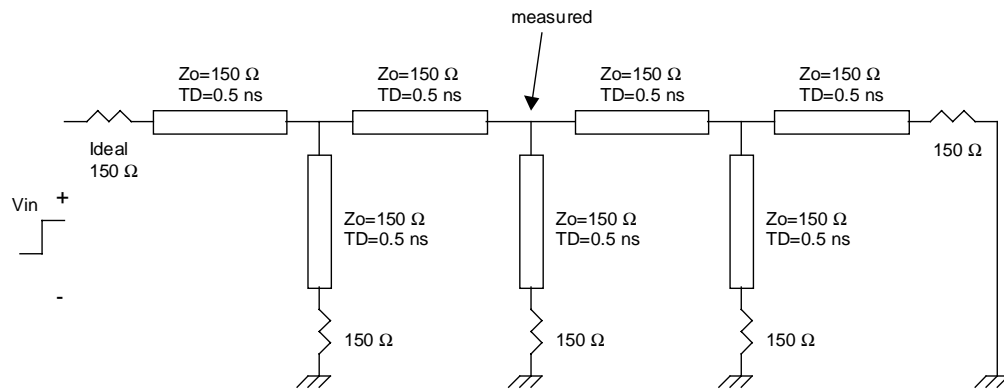


Figure 6.5: Schematic of the digital circuit.

Figure 6.6: Response of each modeling method for the circuit shown in Figure 6.5.
Dashed - macromodel, dotted - equivalent circuit, solid - ideal lumped resistor.

6.2 Analog and RF Application

A second order Butterworth bandpass filter with 3dB cutoff frequencies at 0.8 and 1.2 GHz is shown in Figure 6.7. The details on this filter design are found in [44]. Using empirical models available in the library of Advanced Design System (ADS), an embedded passive component was designed for each ideal lumped element in the circuit. The geometry and its dimensions were chosen to behave closely to the ideal lumped element. Table 6.1 lists the electrical and physical parameters of the embedded passives that were used for the design. The physical dimensions of each structure are shown in Table 6.2. The filter using empirical models is shown in Figure 6.8. Models for the interconnects connecting the passive components have not been introduced to better account for the parasitic behavior.

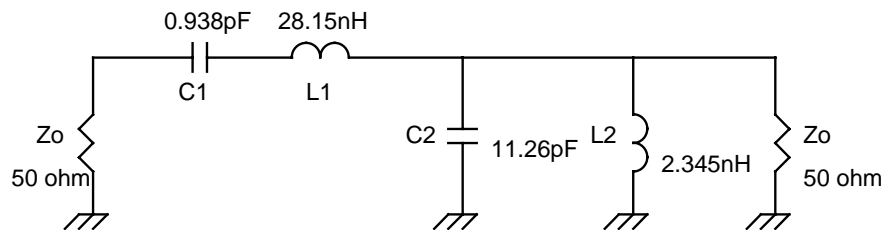


Figure 6.7: Bandpass filter using ideal lumped elements.

Table 6.1: Electrical and physical parameters for the embedded passives.

Dielectric layer thickness	5 mils
Dielectric constant	5.6
Loss tangent	0.001
Metal conductivity	$3 \cdot 10^7$ S/m
Metal thickness	0.5 mil

Table 6.2: Embedded passive structures. All dimensional units are in mils.

	Structure		Structure
C1	<p>57 5 15 Port 1 Port 2 Ground</p>	C2	<p>125 5 5 10 Port 1 Port 2 Ground</p>
L1	<p>8 8 Port 1 Port 2 115 115 Metal on the surface. Distance to the ground – 20 mils</p>	L2	<p>8 8 Port 1 Port 2 62 62 Metal on the surface. Distance to the ground – 20 mils</p>

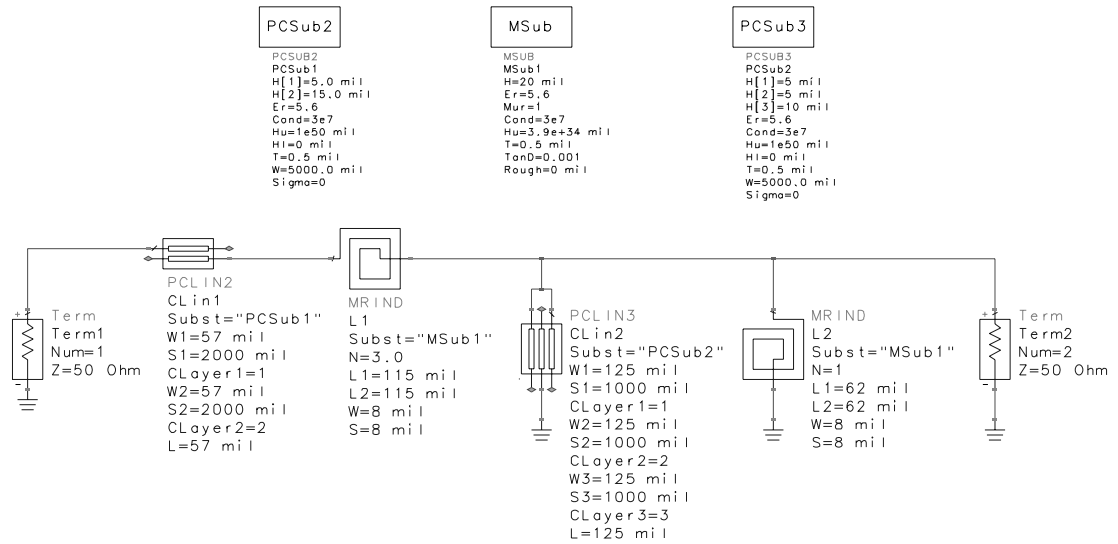


Figure 6.8: Filter using empirical models in ADS.

These structures were modeled using SONNET, an EM solver, to extract the frequency response except for the inductor L2, which was modeled using empirical data. The data points were interpolated to generate rational functions, which were used to develop SPICE macromodels. Losses in the two capacitors, C1 and C2, were small due to its geometry and were neglected. The response of the capacitors was represented by lossless rational functions, which are in the form of a ratio of an even powered polynomial and an odd powered polynomial or vice versa [30][31]. Most of the losses in the filter come from the two inductors, L1 and L2, and their losses were fully incorporated. The inductor L1 and the two capacitors were represented with a two-port macromodel using rational functions approximating the z-parameter responses. The inductor L2 was represented with a one-port macromodel approximating the input impedance.

For embedded structures C1, C2, and L2, the rational functions in the macromodels were used to synthesize lumped equivalent circuits. For inductor L1, the response was reinterpolated to generate lossless rational functions, which allowed the synthesis of a lossless equivalent circuit. To incorporate the losses, resistors were added and were optimized using a gradient optimizer in Microwave Design System (MDS). Figure 6.9 shows the macromodel and Figure 6.10 shows the equivalent circuit that represents the bandpass filter realized using embedded passives.

The $|S_{21}|$ response for each modeling technique is shown in Figure 6.11. The filter response using SPICE macromodels agrees well with the equivalent circuit model. However, a noticeable difference is observed between the responses of the macromodel

and the empirical model available in ADS, showing discrepancy between the full-wave solution and the empirical solution. Hence, the method discussed in this paper can be used to develop models for new processes where empirical models are inaccurate.

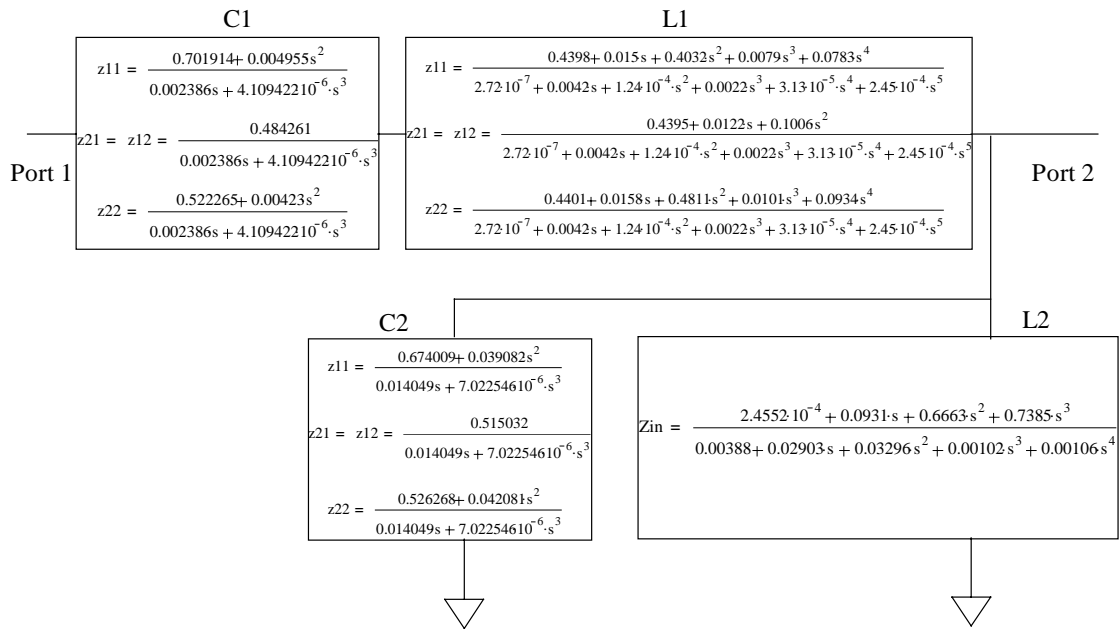


Figure 6.9: Macromodel for the filter.

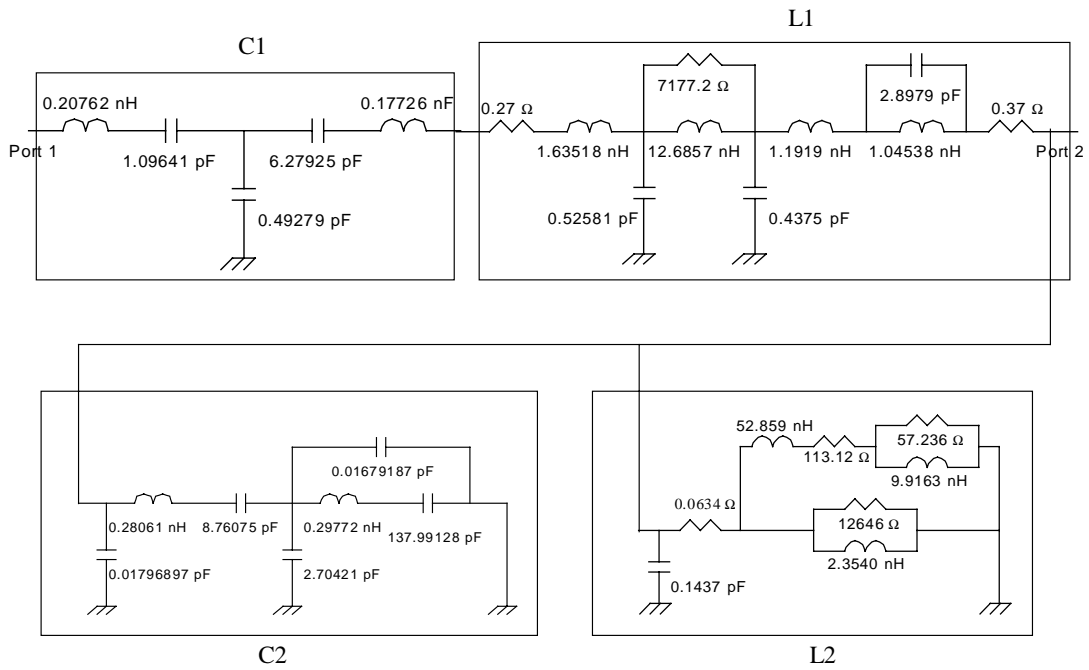


Figure 6.10: Equivalent circuit for the filter.

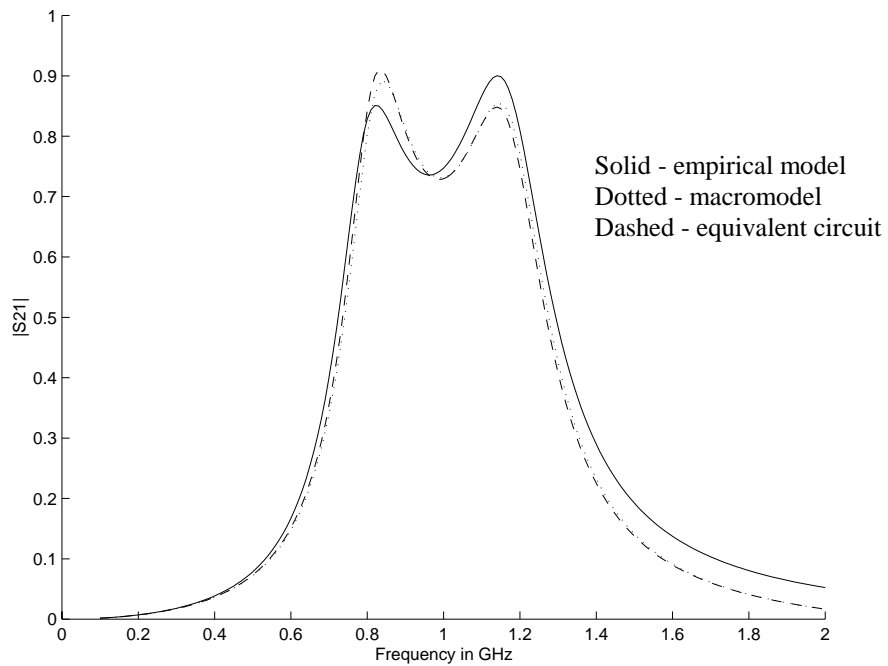


Figure 6.11: $|S_{21}|$ response of the filter.

CHAPTER 7

CONCLUSIONS AND FUTURE WORK

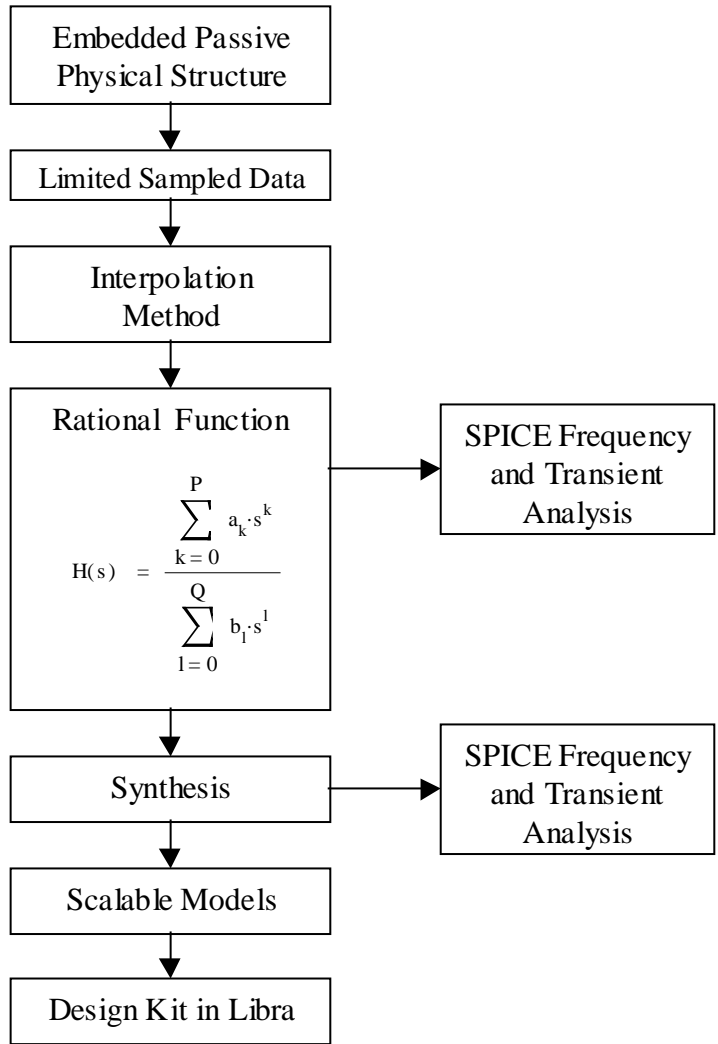
7.1 Conclusions

In this dissertation, modeling methods are presented to accurately model embedded passive components using rational functions. Based on the results of the modeling techniques presented in this dissertation, the following conclusions are drawn.

- A sampling and interpolation method was presented for embedded passives. The method reduced the EM simulation time for complex 3D structures. This is a useful method for realizing embedded passives.
- The interpolation technique was modified to generate rational functions with real coefficients and a common denominator for multiple-port structures. This modification allowed development of SPICE macromodels and synthesis of equivalent circuits. The method used to generate the macromodels is a major contribution.

- The interpolation technique did not guarantee a stable solution. In this dissertation, a stability-enforcing algorithm was developed. When used with the interpolation technique, a stable solution was always obtained.
- Macromodeling technique demonstrated that limited frequency data samples were sufficient to capture the parasitic effects in transient response.
- Equivalent circuits were extracted from a limited sampled data. Equivalent circuits physically correlated to the geometry of the structure. The physical correlation revealed parasitic effects and provided a ground work in developing scalable models [41]. This is a major contribution since it provides a path for developing design libraries for new processes.

When the modeling techniques are incorporated in a circuit design, the design of embedded passives would consist of the following procedure:



7.2 Future Work

When many embedded components are integrated in a substrate, there is electromagnetic interference (EMI) between the components. This undesirable effect becomes more significant as the components are placed more closely. Such unwanted EM effect is not well understood and an accurate modeling technique is needed for the circuit designers. For the work in the future, study of the EM and coupling effect between the embedded components is proposed. Modeling techniques will be utilized to model EMI. One of the ways to approach this problem is to analyze circuits with multiple structures using equivalent circuit synthesis, which may reveal coupling effects between the components.

Another proposed work for the future is sampling method for interpolation. To ensure the interpolation uses a minimum number of data for a new structure, methods for data selection will be studied further (from the work presented in the section 2.6). The method will allow the designers to use minimum number of data samples for interpolation of a new class of structures.

7.3 Publications Generated

The following publications were generated.

1. **Kwang Lim Choi** and Madhavan Swaminathan, "Utilization of Fast Algorithm to Analyze Embedded Passive Components Using Commercial EM Solvers," *IEEE 6th Topical Meeting on Electrical Performance of Electronic Packaging*, San Jose, CA, October 1997, pp.240-243.
2. **Kwang Lim Choi**, Nanju Na and Madhavan Swaminathan, "Characterization of Embedded Passives Using Macromodels in LTCC Technology," *IEEE Trans. on Components, Packaging and Manufacturing Technology- Part B*, Vol. 21, No. 3, August 1998, pp. 258-268.
3. **Kwang Lim Choi** and Madhavan Swaminathan, "Synthesis of RF Circuits for Embedded Passive Components in Mixed Signal Applications," *Proceedings of 48th Electronic Components & Technology Conference*, Seattle, Washington, 1998, pp.1052-1060.
4. **Kwang Lim Choi** and Madhavan Swaminathan, "Synthesis of Equivalent Circuits for Two-Port Integral Passive Components," Submitted to and accepted by 1999 *Proceedings on Multichip Modules and High Density Packaging (MCM)*, Denver, Colorado, April 1999.
5. **Kwang Lim Choi** and Madhavan Swaminathan, "Development of Model Libraries for Embedded Passives Using Network Synthesis," Submitted to *IEEE Transactions on Circuits and Systems II*, 1999.

6. **Kwang Lim Choi** and Madhavan Swaminathan, "Simulation of Embedded RF Circuits Using Macromodels and Synthesized Equivalent Circuits," Submitted to *Electrical Performance of Electrical Packaging*, 1999.
7. Nanju Na, **Kwang Lim Choi** and Madhavan Swaminathan, "Characterization of Embedded Resistors for High Frequency Wireless Applications," *IEEE Radio and Wireless Conference*, August 9-12, 1998.
8. Anisha Sood, **Kwang Lim Choi**, Anand Haridass, Nanju Na and Madhavan Swaminathan, "Modeling and Mixed Signal Simulation of Embedded Passive Components in High Performance Packages", *1998 Proceedings on Multichip Modules and High Density Packaging*, Denver, CO, April 1998, pp.506-511.
9. A. Fathy, V. Pendrick, G. Ayers, B. Geller, Y. Narayan, B. Thaler, H. D. Chen, M. J. Liberatore, J. Prokop, **Kwang Lim Choi** and M. Swaminathan, "Design of embedded passive components in Low-Temperature Cofired Ceramic on Metal (LTCC-M) technology", pp. 1281-1284, Vol. 3, *Microwave Symposium*, 1998.

7.4 Awards

1. Educational Foundation Award for the proposal entitled "Embedded Design of RF Components in Low Temperature Cofired Ceramic (LTCC) Technology" by the International Microelectronics and Packaging Society (IMAPS) for the school year 1997-1998 in amount of \$6,000.

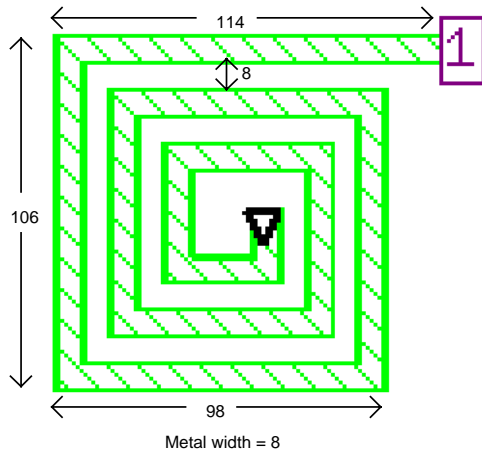
APPENDIX

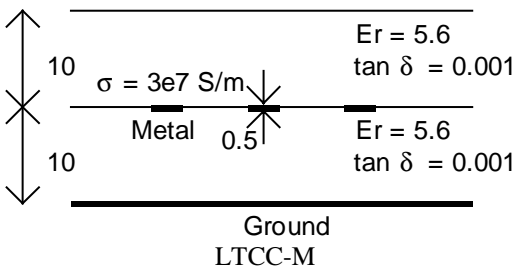
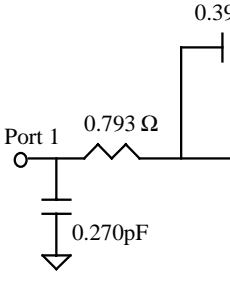
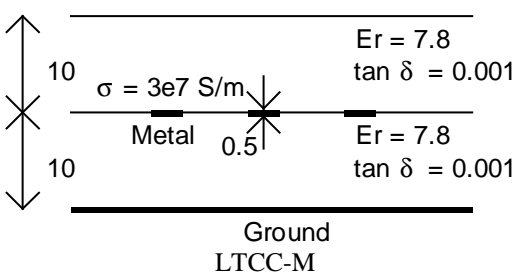
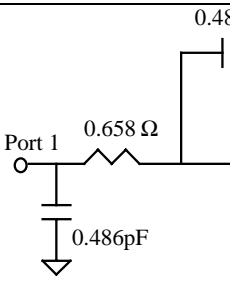
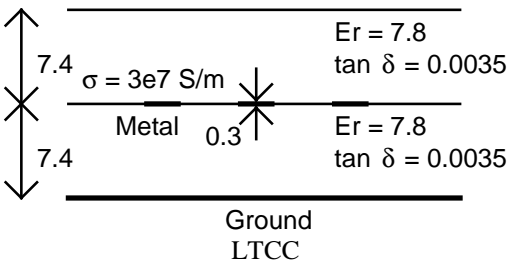
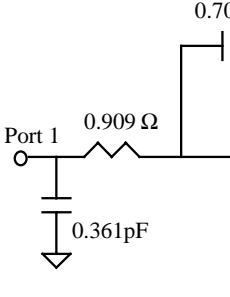
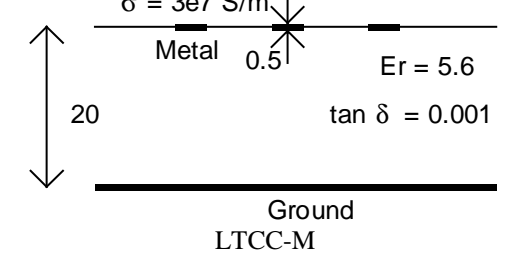
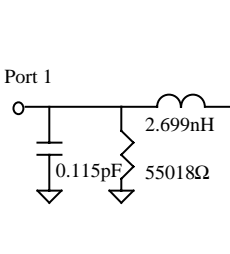
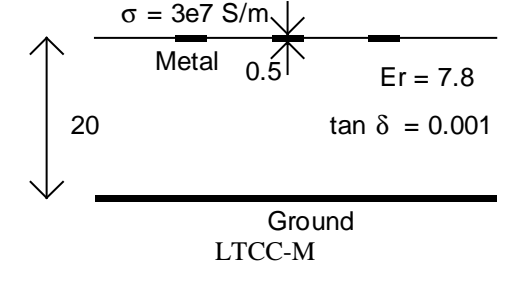
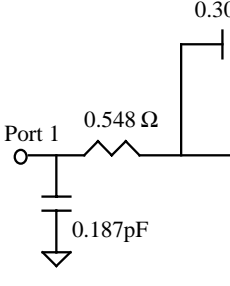
This appendix lists all the embedded structures discussed in this dissertation and the corresponding macromodel and equivalent circuit. The rational functions are denoted by a list of coefficients. In the case of one-port structures, either input impedance or admittance was interpolated (as indicated in macromodel column). The numerator coefficients are listed in 'a' matrix and denominator coefficients are listed in 'b' matrix.

In the case of two-port structures, z-parameter response was interpolated. The z_{11} numerator coefficients are listed in 'a' matrix. The z_{21} (or z_{12}) numerator coefficients are listed in 'b' matrix. The z_{22} numerator coefficients are listed in 'c' matrix. The common denominator coefficients are listed in 'd' matrix.

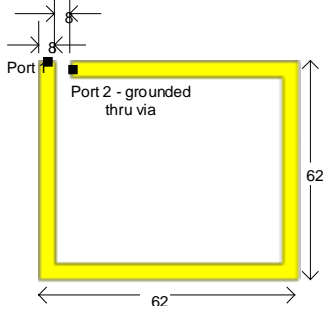
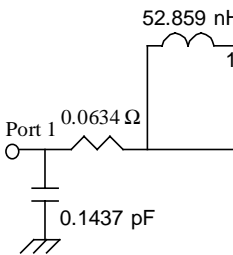
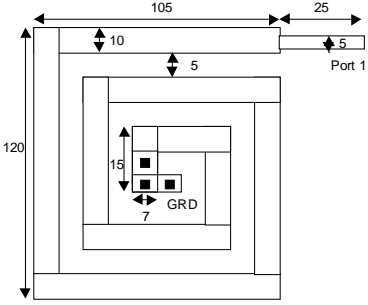
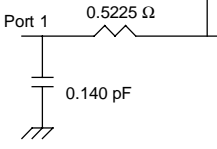
In all cases, the first number in the list corresponds to the first coefficient with a power of zero, the second number in the list corresponds to the second coefficient with a power of one, etc.

A.1 One-port Inductor

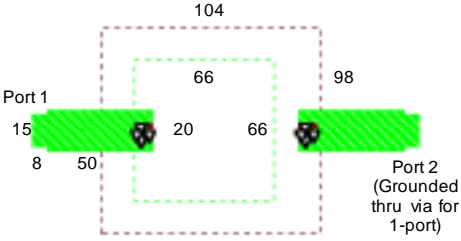


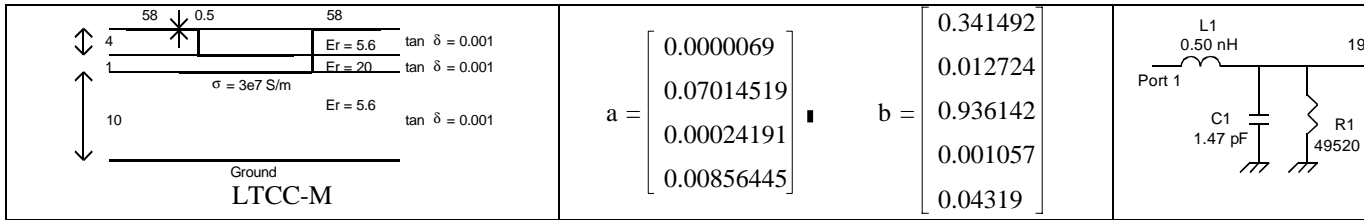
Structure	Macromodel	Equiva
 <p>Er = 5.6 tan δ = 0.001 $\sigma = 3e7$ S/m Metal 0.5 Er = 5.6 tan δ = 0.001 Ground LTCC-M</p>	<p>Zin, fscale = 1e9</p> $a = \begin{bmatrix} 0.082391 \\ 0.991161 \\ 6.088821 \cdot 10^{-4} \\ 0.001402 \end{bmatrix}$ $b = \begin{bmatrix} 0.103967 \\ 1.865426 \cdot 10^{-4} \\ 8.106577 \cdot 10^{-4} \\ 3.737655 \cdot 10^{-7} \\ 3.789698 \cdot 10^{-7} \end{bmatrix}$	 <p>0.30 Port 1 0.793 Ω 0.270 pF</p>
 <p>Er = 7.8 tan δ = 0.001 $\sigma = 3e7$ S/m Metal 0.5 Er = 7.8 tan δ = 0.001 Ground LTCC-M</p>	<p>Zin, fscale = 1e9</p> $a = \begin{bmatrix} 0.07028 \\ 0.991795 \\ 8.154097 \cdot 10^{-4} \\ 0.001993 \end{bmatrix}$ $b = \begin{bmatrix} 0.106761 \\ 2.570462 \cdot 10^{-4} \\ 0.001175 \\ 8.427054 \cdot 10^{-7} \\ 9.67819 \cdot 10^{-7} \end{bmatrix}$	 <p>0.48 Port 1 0.658 Ω 0.486 pF</p>
 <p>Er = 7.8 tan δ = 0.0035 $\sigma = 3e7$ S/m Metal 0.3 Er = 7.8 tan δ = 0.0035 Ground LTCC</p>	<p>Zin, fscale = 1e12</p> $a = \begin{bmatrix} 4.945992 \cdot 10^{-8} \\ 4.540054 \cdot 10^{-4} \\ 5.840788 \cdot 10^{-4} \\ 0.940499 \end{bmatrix}$ $b = \begin{bmatrix} 5.442401 \cdot 10^{-8} \\ 1.826995 \cdot 10^{-7} \\ 5.952754 \cdot 10^{-4} \\ 5.807797 \cdot 10^{-4} \\ 0.339795 \end{bmatrix}$	 <p>0.70 Port 1 0.909 Ω 0.361 pF</p>
 <p>$\sigma = 3e7$ S/m Metal 0.5 Er = 5.6 tan δ = 0.001 Ground LTCC-M</p>	<p>Zin, fscale = 1e9</p> $a = \begin{bmatrix} 0.070894 \\ 0.994326 \\ 1.857487 \cdot 10^{-4} \\ 8.402668 \cdot 10^{-4} \end{bmatrix}$ $b = \begin{bmatrix} 0.079302 \\ 7.706411 \cdot 10^{-5} \\ 4.260931 \cdot 10^{-4} \\ 3.670401 \cdot 10^{-8} \\ 9.694824 \cdot 10^{-8} \end{bmatrix}$	 <p>Port 1 2.699 nH 0.115 pF 55018 Ω</p>
 <p>$\sigma = 3e7$ S/m Metal 0.5 Er = 7.8 tan δ = 0.001 Ground LTCC-M</p>	<p>Zin, fscale = 1e9</p> $a = \begin{bmatrix} 0.063328 \\ 0.994822 \\ 5.890935 \cdot 10^{-4} \\ 0.001185 \end{bmatrix}$ $b = \begin{bmatrix} 0.079482 \\ 1.327119 \cdot 10^{-4} \\ 5.838579 \cdot 10^{-4} \\ 3.271525 \cdot 10^{-7} \\ 2.218134 \cdot 10^{-7} \end{bmatrix}$	 <p>0.30 Port 1 0.548 Ω 0.187 pF</p>

The other inductor structures are listed in the following table:

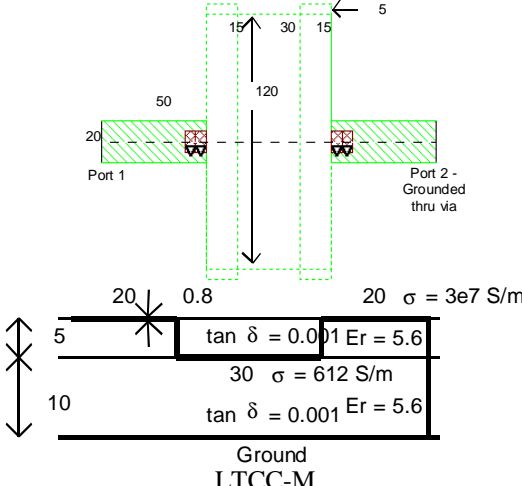
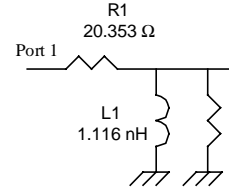
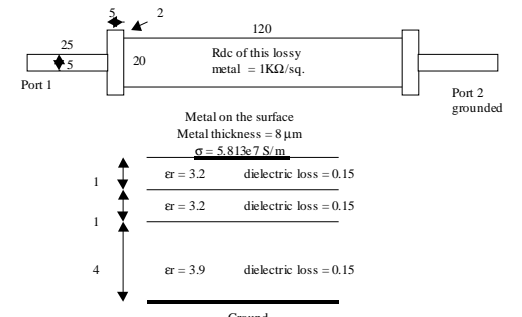
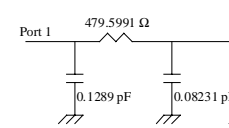
Structure	Macromodel	Equiva												
 <p>Distance from metal to ground = 20 mils. Metal thickness = 0.5 mils, ϵ_r of layer = 5.6, $\sigma = 3e7$ S/m, $\tan \delta = 0.001$ LTCC-M</p>	<p>Z_{in}, Fscale = 1e10</p> $a = \begin{bmatrix} 0.000246 \\ 0.093057 \\ 0.666338 \\ 0.738504 \end{bmatrix}$ $b = \begin{bmatrix} 0.003875 \\ 0.029033 \\ 0.032956 \\ 0.001016 \\ 0.001061 \end{bmatrix}$													
 <p>$\sigma = 5.8e7$ S/m Metal thickness = 8 μm</p> <table border="1" data-bbox="357 1165 722 1375"> <tr> <td>1</td> <td>Loss tan = 0.015</td> <td>via</td> <td>$\epsilon_r = 3.2$</td> </tr> <tr> <td>1</td> <td>Loss tan = 0.015</td> <td></td> <td>$\epsilon_r = 3.2$</td> </tr> <tr> <td>4</td> <td>Loss tan = 0.015</td> <td></td> <td>$\epsilon_r = 3.9$</td> </tr> </table> <p>Ground SLIM</p>	1	Loss tan = 0.015	via	$\epsilon_r = 3.2$	1	Loss tan = 0.015		$\epsilon_r = 3.2$	4	Loss tan = 0.015		$\epsilon_r = 3.9$	<p>Z_{in}, fscale = 1e10</p> $a = \begin{bmatrix} 0.007076 \\ 0.994996 \\ 0.008654 \\ 0.098131 \end{bmatrix}$ $b = \begin{bmatrix} 0.013542 \\ 0.0002728 \\ 0.006629 \\ 0.0000265 \\ 0.000137 \end{bmatrix}$	
1	Loss tan = 0.015	via	$\epsilon_r = 3.2$											
1	Loss tan = 0.015		$\epsilon_r = 3.2$											
4	Loss tan = 0.015		$\epsilon_r = 3.9$											

A.2 One-port Capacitor

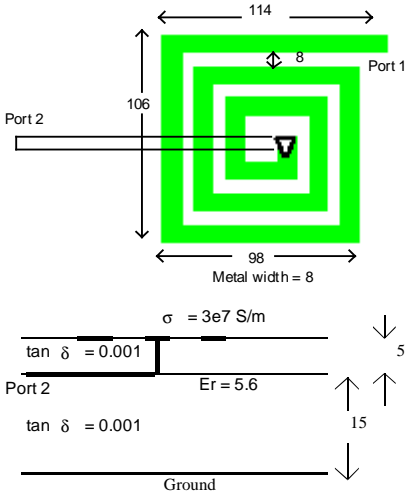
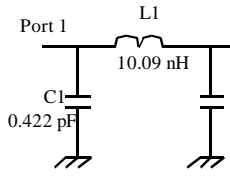
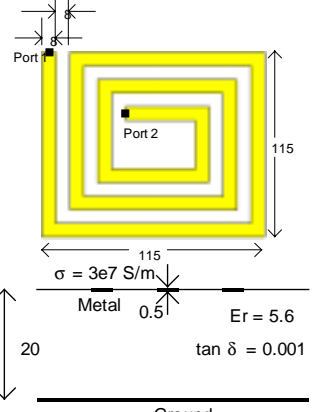
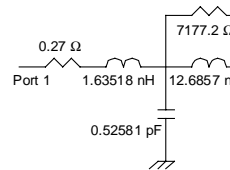
Structure	Macromodel	Equiva
	<p>Y_{in}, fscale = 1e10</p>	



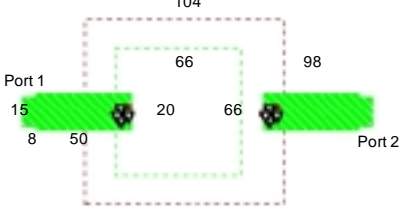
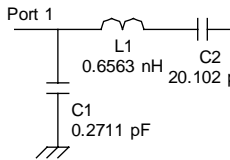
A.3 One-port Resistor

Structure	Macromodel	Equiva
 <p style="text-align: center;">Ground LTCC-M</p>	<p style="text-align: center;">Macromodel Zin, fscale = 1e10</p> $a = \begin{bmatrix} 0.771073 \\ 0.626385 \\ 0.101982 \\ 0.033584 \end{bmatrix} \quad b = \begin{bmatrix} 0.037886 \\ 0.010004 \\ 0.004816 \\ 0.000703 \end{bmatrix}$	
 <p style="text-align: center;">Ground SLIM</p>	<p style="text-align: center;">Macromodel Zin, fscale = 1e10</p> $a = \begin{bmatrix} 1.128207 \\ 5.65534 \\ 5.190106 \\ 0.969585 \end{bmatrix} \quad b = \begin{bmatrix} 0.0001922 \\ 0.0045662 \\ 0.0129912 \\ 0.0087128 \\ 0.00125 \end{bmatrix}$	

A.4 Two-port Inductor

Structure	Macromodel	Equiva
 <p style="text-align: center;">LTCC-M</p>	<p>z-parameter, fscale = 1e10, DC - 2 GHz</p> $a = \begin{pmatrix} 0.51582 \\ 0 \\ 0.296426 \end{pmatrix} \quad b = 0.533$ $c = \begin{pmatrix} 0.519436 \\ 0 \\ 0.304266 \end{pmatrix} \quad d = \begin{bmatrix} 0 \\ 0.005118 \\ 0 \\ 0.001252 \end{bmatrix}$	
 <p style="text-align: center;">LTCC-M</p>	<p>z-parameter, fscale = 1e10, DC - 2 GHz</p> $a = \begin{bmatrix} 0.483442 \\ 0 \\ 0.344459 \\ 0 \\ 0.023069 \end{bmatrix} \quad b = 0.480578$ $c = \begin{bmatrix} 0.483511 \\ 0 \\ 0.426679 \\ 0 \\ 0.016815 \end{bmatrix} \quad d = \begin{bmatrix} 0 \\ 0.004657 \\ 0 \\ 0.001411 \\ 0 \end{bmatrix}$	

A.5 Two-port Capacitor

Structure	Macromodel	Equiva
 <p style="text-align: center;">LTCC-M</p>	<p>z-parameter, fscale = 1e9</p>	

<p style="text-align: center;">Ground LTCC-M</p>	$a = \begin{pmatrix} 0.6093677 \\ 0 \\ 0.0006363 \end{pmatrix} \quad b = 0.561141$ $c = \begin{pmatrix} 0.560163 \\ 0 \\ 0.0006854 \end{pmatrix} \quad d = \begin{bmatrix} 0 \\ 0.001135 \\ 0 \\ 1.725176 \cdot 10^{-7} \end{bmatrix}$	
<p style="text-align: center;">Ground LTCC-M</p> <p>σ of metal = $3e7$ S/m, $\epsilon_r = 5.6$, $\tan \delta = 0.001$</p>	<p>z-parameter, fscale = $1e10$, DC - 2 GHz</p> $a = \begin{pmatrix} 0.701914 \\ 0 \\ 0.004955 \end{pmatrix} \quad b = 0.484261$ $c = \begin{pmatrix} 0.522265 \\ 0 \\ 0.00423 \end{pmatrix} \quad d = \begin{bmatrix} 0 \\ 0.002386 \\ 0 \\ 0 \end{bmatrix}$	
<p style="text-align: center;">Ground LTCC-M</p> <p>σ of metal = $3e7$ S/m, $\epsilon_r = 5.6$, $\tan \delta = 0.001$</p>	<p>z-parameter, fscale = $1e10$, DC - 2 GHz</p> $a = \begin{pmatrix} 0.674009 \\ 0 \\ 0.039082 \end{pmatrix} \quad b = 0.515032$ $c = \begin{pmatrix} 0.526268 \\ 0 \\ 0.042081 \end{pmatrix} \quad d = \begin{bmatrix} 0 \\ 0.014049 \\ 0 \\ 7.022546 \cdot 10^{-6} \end{bmatrix}$	
<p style="text-align: center;">Ground SLIM</p> <p>Metal thickness = $8 \mu\text{m}$</p> <p>$\sigma = 5.8e7$ S/m</p> <p>Loss tan = 0.015, $\epsilon_r = 20$ (top layer)</p> <p>Loss tan = 0.015, $\epsilon_r = 3.2$ (middle layer)</p> <p>Loss tan = 0.015, $\epsilon_r = 3.9$ (bottom layer)</p>	<p>z-parameter, fscale = $1e10$</p> $a = \begin{pmatrix} 0.610768 \\ 0 \\ 0.009164 \end{pmatrix} \quad b = 0.55341$ $c = \begin{pmatrix} 0.566151 \\ 0 \\ 0.009197 \end{pmatrix} \quad d = \begin{bmatrix} 0 \\ 0.002161 \\ 0 \\ 7.369792 \cdot 10^{-6} \end{bmatrix}$	

A.6 Two-port Resistor

Structures	Macromodel	Equiva
<p style="text-align: center;">LTCC-M</p>	<p style="text-align: center;">z-parameter, fscale = 1e10</p> $a = \begin{bmatrix} 0.026942 \\ 0.025207 \\ 0.004505 \\ 0.001942 \end{bmatrix} \quad b = \begin{bmatrix} -0.0269107 \\ -0.0207841 \\ 0.0017975 \\ 0.0000877 \end{bmatrix}$ $c = \begin{bmatrix} 0.026942 \\ 0.025207 \\ 0.004505 \\ 0.001942 \end{bmatrix} \quad d = \begin{bmatrix} 0.547213 \\ 0.787586 \\ 0.274502 \\ 0.030021 \\ 0.009126 \end{bmatrix}$	<p style="text-align: center;">Port 1 \rightarrow $R1$ \rightarrow $L1$ \rightarrow Port 2</p> <p style="text-align: center;">10.06Ω 0.580 nH</p>

REFERENCES

- [1] R.R. Tummala, E.J. Rymaszewski, A.G. Klopfenstein, Microelectronics Packaging Handbook Semiconductor Packaging Part II, International Thomson Publishing, New York.
- [2] Paul H.M. Keizer, "Ceramic Multicomponent Modules: A New Approach to Miniaturization", *IEEE trans. on Components, Packaging, and Manufacturing Technology - Part A*, vol 17, No.3, Sept. 1994.
- [3] S. Vasudevan, A. Shaikh, "Microwave Characterization of Low Temperature Cofired Ceramic System", *1997 International Symposium on Advanced Packaging Materials*, pp.152-157.
- [4] J. Muller, H. Thust, K.H. Drue, "RF-Design Considerations for Passive Elements in LTCC Material Systems", *The International Journal of Microcircuits and Electric Packaging*, Volume 18, Number 3, Third Quarter 1995.
- [5] O. Salmela, P. Ikalainen, "Ceramic Packaging Technologies for Microwave Application", *IEEE 1997 Wireless Communications Conference*, pp162-164.
- [6] T. Lenihan, L. Shaper, Y. Shi, G. Morgan, J. Parkerson, "Embedded Thin Film Resistors, Capacitors and Inductors in Flexible Polyimide Films", *IEEE 1996 Electronic Components and Technology Conference*, pp119-124.
- [7] Fairchild, Morcan, Lenihan, Brown, Schaper, Ang, Sommers, Parkerson, Glover, "Reliability of Flexible Thin-Film Embedded Resistors and Electrical Characterization of Thin-Film Embedded Capacitors and Inductors", *1997 47th IEEE Electronic Components and Technology Conference*, p730-738.

- [8] D. G. Swanson, "Simulating EM Fields", *IEEE Spectrum*, pp34-37, November 1991.
- [9] N. Jain, P. Onno, "Methods of Using Commercial Electromagnetic Simulators for Microwave and Millimeter-Wave Circuits Design and Optimization", *IEEE trans. on Microwave Theory and Techniques*, Vol. 45, No. 5, May 1997.
- [10] A.E. Ruehli, "Equivalent Circuit Models for Three-Dimensional Multiconductor Systems", *IEEE Trans. on Microwave Theory and Techniques*, Vol. MTT-22, No. 3, March 1974.
- [11] H. Heeb, A.E. Ruehli, "Three-Dimensional Interconnect Analysis Using Partial Element Equivalent Circuits", *IEEE Trans. on Circuits and Systems-I: Fundamental Theory and Applications*, Vol.39, No.11, November 1992.
- [12] Albert Ruehli, "Partial Element Equivalent Circuit (PEEC) Method and its Application in the Frequency and Time Domain", *IEEE International Symposium On Electromagnetic Compatibility*, 1996, p128-133.
- [13] A.E. Ruehli, J. Garrett, C.R. Paul, "Circuit Models for 3D Structures with Incident Fields", *Proc. IEEE International Symposium on Electromagnetic Compatibility*, p28-31, August 1993.
- [14] J. Zhao, R. Frye, W. Dai, K.L. Tai, "S Parameter-Based Experimental Modeling of High Q MCM Inductor with Exponential Gradient Learning Algorithm", *IEEE Trans. on Components, Packaging, and Manufacturing Technology-Part B*, Vol.20, No.3, August 1997.
- [15] Kendall Su, Analog Filters, Chapman & Hall, London, 1996.
- [16] James C. Rautio, "Synthesis of Lumped Models from N-Port Scattering Parameter Data", *IEEE Trans. on Microwave Theory and Techniques*, Vol.42, No.3, March 1994.

- [17] K. Kottapalli, T. Sarkar, Y. Hua, E. Miller, and G. Burke, "Accurate computation of wide-band response of electromagnetic systems utilizing narrow-band information," *IEEE Trans. Microwave Theory and Techniques*, vol. 39, pp. 682-688, April 1991.
- [18] R. Adve, T. Sarkar, S. Rao, E. Miller, and D. Pflug, "Application of the Cauchy Method for Extrapolating/Interpolating Narrow-Band System Responses," *IEEE Trans. Microwave Theory and Techniques*, vol. 45, pp. 837-845, May 1997.
- [19] Kwang Lim Choi and Madhavan Swaminathan, "Utilization of Fast Algorithm to Analyze Embedded Passive Components Using Commercial EM Solvers," *IEEE 6th Topical Meeting on Electrical Performance of Electronic Packaging*, San Jose, CA, October 1997, pp.240-243.
- [20] Andreas Cangellaris and John Prince, "Modeling and Simulation for Mixed-Signal Package Design," *Advances in Electronic Packaging*, EEP-vol. 19-1, vol. 1, pp.497-507, 1997.
- [21] Raghavan, Rohrer, Pillage, Lee, Bracken, Alaybeyi, "AWE-Inspired", *IEEE 1993 Custom Integrated Circuits Conference*, p18.1.1-18.1.7.
- [22] L.T. Pillage, R.A. Rohrer, "Asymptotic Waveform Evaluation for Timing Analysis", *IEEE Trans. on Computer-Aided Design*, Vol.9, No.4, April 1990.
- [23] E. Chiprout, Michel Nakhla, "Generalized Moment-matching Methods for Transient Analysis of Interconnect Networks", *29th ACM/IEEE Design Automation Conference*, 1992.
- [24] Gilbert Strang, Introduction to Linear Algebra, Wellesley-Cambridge Press, Wellesley, Chapter 4, pp.179-188.
- [25] SONNET User's Manual, SONNET Software, Inc., Volume 1, September 1996.

- [26] Chender Huang, Mustafa Celik and John L. Prince, "Simultaneous Switching Noise Simulation for Thin Film Packages Using Macromodeling Technique", *1996 Electronic Components and Technology Conference*, pp.747-751, 1996
- [27] Kwang Lim Choi, Nanju Na and Madhavan Swaminathan, "Characterization of Embedded Passives Using Macromodels in LTCC Technology," *IEEE Trans. on Components, Packaging and Manufacturing Technology- Part B*, Vol. 21, No. 3, August 1998, pp. 258-268
- [28] Nanju Na, Kwang Lim Choi and Madhavan Swaminathan, "Characterization of Embedded Resistors for High Frequency Wireless Applications," *IEEE Radio and Wireless Conference*, August 9-12, 1998.
- [29] Kwang Lim Choi and Madhavan Swaminathan, "Synthesis of RF Circuits for Embedded Passive Components in Mixed Signal Applications," *Proceedings of 48th Electronic Components & Technology Conference*, Seattle, Washington, 1998, pp.1052-1060.
- [30] Kwang Lim Choi and Madhavan Swaminathan, "Synthesis of Equivalent Circuits for Two-Port Integral Passive Components," *Proceedings on Multichip Modules and High Density Packaging (MCM)*, Denver, Colorado, April 1999, pp.316-321.
- [31] Kwang Lim Choi and Madhavan Swaminathan, "Synthesis of RF Circuits from Rational Functions for Integral Passive Structures in Packaging," Submitted to *IEEE Transactions on Circuits and Systems II*.
- [32] Louis Weinberg, Network Analysis and Synthesis, McGraw-Hill Book Company, Inc., New York, Chapter 9, pp.397-421, 1962.
- [33] Ernst Guillemin, Synthesis of Passive Networks, John Wiley & Sons, Inc., New York, 1957.
- [34] Norman Balabanian and Theodore Bickart, Linear Network Theory: Analysis, Properties, Design and Synthesis, Matrix Publishers, Inc., Beaverton, Oregon, 1981.

- [35] Anisha Sood, Kwang Lim Choi, Anand Haridass, Nanju Na and Madhavan Swaminathan, "Modeling and Mixed Signal Simulation of Embedded Passive Components in High Performance Packages", *1998 Proceedings on Multichip Modules and High Density Packaging*, Denver, Colorado, April 1998, pp.506-511.
- [36] Murray R. Spiegel, Advanced Mathematics for Engineers and Scientists, Schaum's Outline Series, McGraw-Hill, New York, Chapter 4, pp.98-120, 1998.
- [37] Alan V. Oppenheim and Ronald W. Schaffer, *Discrete-Time Signal Processing*, Prentice Hall, New Jersey, Chapter 3, pp.82, 1989.
- [38] A. Fathy, V. Pendrick, G. Ayers, B. Geller, Y. Narayan, B. Thaler, H.D.Chen, M.J.Liberatore, J. Prokop, K.L.Choi and M.Swaminathan, "Design of embedded passive components in Low-Temperature Cofired Ceramic on Metal (LTCC-M) technology", pp. 1281-1284, Vol. 3, *Microwave Symposium*, 1998.
- [39] HSPICE User's Manual, Meta-Software, Inc., Version H92, Volume 1, 1995.
- [40] Heebyung Yoon, "Fault Detection and Identification Techniques for Embedded Analog Circuits," Ph.D Thesis, Georgia Institute of Technology, Chapter 5, pp118-153, July 1998.
- [41] Alberto Baldisserotto and Madhavan Swaminathan, "Development of Scaleable Models for RF Structures in Mixed Signal Packaging", Submitted to the IEEE Workshop on Signal Propagation on Interconnects, Titisee-Neustadt, Germany, May 19-21, 1999.
- [42] E.B. Saff and A.D. Snider, Fundamentals of Complex Analysis for Mathematics, Science, and Engineering, Prentice-Hall, Inc., London, pp.48, 1993.

- [43] J.W. Brown and R.V. Churchill, Complex Variables and Applications, McGraw-Hill, Inc., New York, pp.27, 1996.

- [44] Kwang Lim Choi, "RF Filter Design," Ph.D. Qualifying Exam, Georgia Institute of Technology, May 22, 1988.

- [45] Kwang Lim Choi and Madhavan Swaminathan, "Simulation of Embedded RF Circuits Using Macromodels and Synthesized Equivalent Circuits," Submitted to *Electrical Performance of Electronic Packaging*, 1999.

- [46] D.F. Anastasakis, N. Gopal, S.Y. Kim, L.T. Pillage, "On the Stability of Moment-Matching Approximations in Asymptotic Waveform Evaluation", *29th ACM/IEEE Design Automation Conference*, 1992, p207-212.

- [47] E. Chiprout and M. Nakhla, "Transient Waveform Estimation of High-Speed MCM Networks Using Complex Frequency Hopping", *Proc. Multi-Chip Module Conference*, March 1993.

- [48] M. Celik, O. Ocali, M.A Tan, "Pole-Zero Computation in Microwave Circuits Using Multipoint Pade Approximation", *IEEE Trans. on Circuits and Systems -I: Fundamental Theory and Applications*, Vol.42, No. 1, January 1995.

- [49] Shlomo Karni, Network Theory: Analysis and Synthesis, Allyn and Bacon, Inc., Boston, 1966.

VITA

Kwang Lim Choi was born on October 2, 1972, in Seoul, Korea. He lived in Seoul until he immigrated to the United States in June 1986. He graduated from Stone Mountain High School, Stone Mountain, Georgia, in June 1990. He received BEE in March 1995, MSEE in December 1996, and Ph.D. in EE in December 1999, all from Georgia Institute of Technology, Atlanta, Georgia.

To pursue his Ph.D in Electrical Engineering, Choi began his research in January 1999 at Packaging Research Center, Georgia Tech. He has contributed to a number of publications in the area of modeling and simulation of embedded passive components. Choi won an IMAPS Educational Foundation Grant for the school year 1997-1998 after submitting IMAPS his research proposal on design of embedded passives.

As of the year 1999, Choi resides in Atlanta, Georgia.